




University of
Stavanger

Faculty of Science and Technology

MASTER'S THESIS

Study program/ Specialization: Petroleum Geosciences Engineering	Spring semester, 2012 <u>Open</u> / Restricted access
Writer: Angeliki Kreona	 (Writer's signature)
Faculty supervisor: Robert J. Brown	
External supervisor(s):	
Title of thesis: Processing and analysis of Vertical Seismic Profile data acquired while drilling (VSP-WD)	
Credits (ECTS): 30	
Key words: VSP-WD processing	Pages: 88 + enclosure: 18 Stavanger, 15th of June 2012 Date/year

UNIVERSITY OF STAVANGER



**PROCESSING AND ANALYSIS OF VERTICAL SEISMIC PROFILE DATA
ACQUIRED WHILE DRILLING (VSP-WD)**

Angeliki Kreona

June, 2012

A THESIS SUBMITTED TO THE
UNIVERSITY OF STAVANGER
IN FULFILLMENT OF THE REQUIREMENTS
FOR THE DEGREE OF:
MASTER OF SCIENCE IN PETROLEUM GEOSCIENCES ENGINEERING

Abstract

A Vertical Seismic Profiling While Drilling (VSP-WD) survey method was used to acquire data for processing analysis. This survey carried out in West Cameron in Offshore Louisiana by Schlumberger in 2005. A seismic source was activated in a stable position close to the wellhead, while the three-component receivers were located in the borehole above the drillbit and moving away from the source while drilling.

The principal objective of the current thesis is the identification of the Tex X Sand target. Far offset processing analysis of the recorded-memory data has been used to meet this objective. Both a median and an f - k filter have been used for the separation of the upgoing and downgoing waves. The downgoing P wavefield was used to design a deconvolution operator which was applied to the upgoing P wavefield for a waveshaping deconvolution. An exponential gain has been applied for the amplitude recovery. Finally, shifting to two-way time by doubling the first-break time of the upgoing P waves has been completed.

The main outputs of the processing were the VSPCDP transformation and the VSP corridor stack. The interpretation was based on the comparison among the corridor stack resulting by this process and those of the process on real-time and recorded-memory data provided by Schlumberger.

The very good matching between real-time and recorded-memory corridor stacks and the extension of them deeper to 4000 ms verify that the VSP-WD method can be successfully used for depth uncertainty reduction and look-ahead investigation.

Acknowledgements

There are a few people who have contributed to and made the difference in realization of this master thesis. I would like to acknowledge my supervisor Dr. Robert James Brown for his support and teaching through the last six months. His counsel and comments had a significant contribution towards my emergence as a graduate geoscientist.

I owe a great deal of gratitude to Mr. Neil Kelsall of Schlumberger of Norway for introducing me to the data used in this thesis and to his valuable advice.

I feel extremely grateful for Mr. Carlos Montaña from GEDCO Support. His help through processing of the data was fundamental to complete this project and is greatly appreciated.

I would like to thank from the deep of my heart, my parents Panagiota Kolkouki and Kreon Kreona for their patience, love and care. Special influence in my life has my sister Anastasia Kreona. Her unique personality and intelligence help me to go further in every aspect of my life.

Great moral contribution has been given from my beloved Rodrigo A. Ruyschaert. His support and love are of great importance to my success in every single effort in the past, present and future.

To my loving parents for their support, care and teaching.

Table of Contents

1. Abstract	ii
2. Acknowledgements	iii
3. Dedication	iv
CHAPTER 1: Introduction	1
1.1 Introduction	1
1.2 Thesis Objective	2
1.3 Field Presentation	2
CHAPTER 2: Seismic While Drilling Methods	4
2.1 Introduction to SWD technology	4
2.2 Historical Review of SWD Methods	5
2.3 Vertical Seismic Profile	6
2.4 Vertical Seismic Profile While Drilling (VSP-WD)	8
2.4.1 Data Acquisition	10
2.4.2 Look Ahead Capability	11
CHAPTER 3: VSP Processing	13
3.1 Introduction	13
3.2 Geometry	15
3.2.1 The importance of using three-component geophones	23
3.3 First-Break Picking	24
3.4 Velocity Profile	30
3.5 Hodogram Analysis	34
3.6 Wavefield Separation	43
3.6.1 Wavefield separation using velocity filters	43
3.6.2 Wavefield separation using median filter	44
3.6.3 Separate Downgoing P from H_{max}	44
3.6.4 Separate Upgoing P from Raw Z and H_{max}	50
3.7 Time Variant Orientation	55
3.8 Deconvolution	58
3.9 VSPCDP Transformation and Corridor Stack	63
CHAPTER 4: Interpretation and Conclusion	72
4.1 Interpretation	72

4.2 Conclusion	76
Bibliography	77
Appendix A	79
Appendix B.....	88

List of Figures

Figure 1.1: Location of the target Tex X Sand target provided by Shlumberger.	3
Figure 2.1: VSP-WD method.....	8
Figure 2.2: Receivers on the BHA.....	9
Figure 2.3: General operating procedures for VSP-WD surveys	10
Figure 2.4: Acquisition timing of the tool	11
Figure 3.1: Flow Diagram showing the Processing steps.....	14
Figure 3.2: The difference between a) Measured Depth and b) True Vertical depth. .	15
Figure 3.3: The top and side view of the well path.....	18
Figure 3.4: Raw X wavefield.....	20
Figure 3.5: Raw Y wavefield.....	21
Figure 3.6: Raw Z or Vertical wavefield.	22
Figure 3.7: Deviated VSP ray path geometry.	24
Figure 3.8: Raw Vertical Z with the first-break picking.....	26
Figure 3.9: Raw X with the first-break picking transferred by the Raw Vertical Z. ..	27
Figure 3.10: Raw Y with the first-break picking transferred by the Raw Vertical Z. .	28
Figure 3.11: Time- depth chart.	30
Figure 3.12: On the left side the time-depth curve is shown. In the right part the average velocity curve (blue line) and the interval velocity curve (red line) are illustrated.....	33
Figure 3.13: Hodogram of X, Y components at 3271.22 m depth.....	35
Figure 3.14: Hodogram of X, Y components at 3257.09 m depth.....	35
Figure 3.15: H_{max} Horizontal Rotation.....	37
Figure 3.16: H_{min} Horizontal Rotation.	38
Figure 3.17: Hodogram of H_{max} and Z components at 2964.23 m depth.....	39
Figure 3.18: Hodogram of H_{max} and Z components at 3009.05 m depth.....	40
Figure 3.19: Hodogram of H_{max} and Z components at 3271.22m depth.....	40
Figure 3.20: H_{max}' Hodogram Rotation.	41
Figure 3.21: Z' Hodogram Rotation.	42
Figure 3.22: Downgoing P Separation using a median filter.....	45
Figure 3.23: Downgoing P Separation using an $f-k$ filter.	45
Figure 3.24: FRT Output for Downgoing P Separation using a median filter.....	46

Figure 3.25: -TT Output for Downgoing P Separation using a median filter.....	47
Figure 3.26: FRT Output for Downgoing P Separation using an $f-k$ filter.	48
Figure 3.27: -TT Output for Downgoing P Separation using an $f-k$ filter.	49
Figure 3.28: Upgoing P Separation from Raw Z and H_{\max} using an $f-k$ filter.	50
Figure 3.29: FRT Output of Upgoing P Separation from Raw Z.	51
Figure 3.30: -TT Output of Upgoing P Separation from Raw Z.	52
Figure 3.31: FRT Output of Upgoing P Separation from H_{\max}	53
Figure 3.32: -TT Output of Upgoing P Separation from H_{\max}	54
Figure 3.33: Separation of Upgoing P and SV.	55
Figure 3.34: Upgoing SV Wavefield.	56
Figure 3.35: Upgoing P Wavefield.	57
Figure 3.36: VSP Polarity.	59
Figure 3.37: Deconvolution downgoing P operator.....	60
Figure 3.38: VSP waveshaping deconvolution on upgoing wavefield.....	60
Figure 3.39: Downgoing P deconvolution operator.....	61
Figure 3.40: Z'' Upgoing P wavefield FRT.....	62
Figure 3.41: Processing flow to receive VSPCDP and Corridor Stack.	63
Figure 3.42: Normal Moveout Correction.	65
Figure 3.43: Normal Moveout Correction after a median filter application.....	66
Figure 3.44: Shifting to two-way time after NMO Correction.	67
Figure 3.45: Output of the first band-pass filter.	68
Figure 3.46: Output after the five-trace median filter and the second band-pass filter.	69
Figure 3.47: VSPCDP Transformation on the left and the Corridor Stack on the right.	70
Figure 3.48: Corridor Stacks resulting from different filter application.....	71
Figure 4.1: Recognized events over the VSP2DCDP and Corridor Stack.	73
Figure 4.2: Interpretation between the resulting corridor stack(left) and the corridor stack from recorded-memory data provided by Schlumberger (right).	74
Figure 4.3: Interpretation between the resulting corridor stack (left) and the corridor stack from real-time data provided by Schlumberger (right).....	75

Figure A- 1: Hodogram at 2926.73m depth.....	79
Figure A- 2: Hodogram at 2964.23m depth.....	79
Figure A- 3: Hodogram at 2981.74m depth.....	79
Figure A- 4: Hodogram at 2990.88m depth.....	79
Figure A- 5: Hodogram at 3009.05m depth.....	80
Figure A- 6: Hodogram at 3018.19m depth.....	80
Figure A- 7: Hodogram at 3036.42m depth.....	80
Figure A- 8: Hodogram at 3045.32m depth.....	80
Figure A- 9: Hodogram at 3063.85m depth.....	81
Figure A- 10: Hodogram at 3072.32m depth.....	81
Figure A- 11: Hodogram at 3090.92m depth.....	81
Figure A- 12: Hodogram at 3099.39m depth.....	81
Figure A- 13: Hodogram at 3116.85m depth.....	82
Figure A- 14: Hodogram at 3124.63m depth.....	82
Figure A- 15: Hodogram at 3141.33m depth.....	82
Figure A- 16: Hodogram at 3148.64m depth.....	82
Figure A- 17: Hodogram at 3164.12m depth.....	83
Figure A- 18: Hodogram at 3171.03m depth.....	83
Figure A- 19: Hodogram at 3185.71m depth.....	83
Figure A- 20: Hodogram at 3192.26m depth.....	83
Figure A- 21: Hodogram at 3211.68m depth.....	84
Figure A- 22: Hodogram at 3223.49m depth.....	84
Figure A- 23: Hodogram at 3228.90m depth.....	84
Figure A- 24: Hodogram at 3229.03m depth.....	84
Figure A- 25: Hodogram at 3239.08m depth.....	85
Figure A- 26: Hodogram at 3243.53m depth.....	85
Figure A- 27: Hodogram at 3252.64m depth.....	85

Figure A- 28: Hodogram at 3257.00m depth.....	85
Figure A- 29: Hodogram at 3266.54m depth.....	86
Figure A- 30: Hodogram at 3271.22m depth.....	86
Figure A- 31: Hodogram at 3285.71m depth.....	86
Figure A- 32: Hodogram at 3296.05m depth.....	86
Figure B- 1: Hodogram at 2926.73m depth.....	88
Figure B- 2: Hodogram at 2964.23m depth.....	88
Figure B- 3: Hodogram at 2981.74m depth.....	88
Figure B- 4: Hodogram at 2990.88m depth.....	88
Figure B- 5: Hodogram at 3009.05m depth.....	89
Figure B- 6: Hodogram at 3018.19m depth.....	89
Figure B- 7: Hodogram at 3036.42m depth.....	89
Figure B- 8: Hodogram at 3045.32m depth.....	89
Figure B- 9: Hodogram at 3063.85m depth.....	90
Figure B- 10: Hodogram at 3072.32m depth.....	90
Figure B- 11: Hodogram at 3090.92m depth.....	90
Figure B- 12: Hodogram at 3099.39m depth.....	90
Figure B- 13: Hodogram at 3116.85m depth.....	91
Figure B- 14: Hodogram at 3124.63m depth.....	91
Figure B- 15: Hodogram at 3141.33m depth.....	91
Figure B- 16: Hodogram at 3148.64m depth.....	91
Figure B- 17: Hodogram at 3164.12m depth.....	92
Figure B- 18: Hodogram at 3171.03m depth.....	92
Figure B- 19: Hodogram at 3185.71m depth.....	92
Figure B- 20: Hodogram at 3192.26m depth.....	92
Figure B- 21: Hodogram at 3211.68m depth.....	93

Figure B- 22: Hodogram at 3223.49m depth.....	93
Figure B- 23: Hodogram at 3228.90m depth.....	93
Figure B- 24: Hodogram at 3229.03m depth.....	93
Figure B- 25: Hodogram at 3239.08m depth.....	94
Figure B- 26: Hodogram at 3243.53m depth.....	94
Figure B- 27: Hodogram at 3252.64m depth.....	94
Figure B- 28: Hodogram at 3257.00m depth.....	94
Figure B- 29: Hodogram at 3266.54m depth.....	95
Figure B- 30: Hodogram at 3271.22m depth.....	95
Figure B- 31: Hodogram at 3285.71m depth.....	95
Figure B- 32: Hodogram at 3296.05m depth.....	95

List of Tables

Table 2.1: The VSP in exploration and production	7
Table 3.1: Wellhead and source location.....	16
Table 3.2: Vertical Seismic Profile geometry.....	16
Table 3.3: Component representation by the Trace-ID Code.....	18
Table 3.4: First break times for each depth level.....	29
Table 3.5: Variation of P-wave velocities with the depth.....	31
Table A- 1 : Rotation Angles and Bearing from the First Rotation.....	79
Table B- 1: Rotation Angles and Bearing from the Second Rotation.....	88

CHAPTER 1: Introduction

1.1 Introduction

Surface seismic surveys may include high uncertainty in the prediction of the actual depth of a target. The detailed stratigraphic analysis of thin and often deep targets cannot be adequately imaged. Seismic images characterized by high frequency, high signal-to-noise ratio and less attenuation are vital for the subsurface mapping. Methods that developed to satisfy this great need based on the vertical seismic profile technique (VSP). Vertical seismic profiling is a technique in which seismic signals, generated at the surface of the earth, are recorded by geophones at various depths in a borehole. Different VSP methods have been developed and used extensively in the few decades by the oil industry for more accurate subsurface mapping and geosteering.

In this master thesis, the Vertical Seismic Profile While Drilling (VSP-WD) method is under consideration. VSP-WD is a technique that has been developed and used by Schlumberger since 2000. The main objective of this technique is to reduce the depth uncertainty while drilling. During the drilling procedure, real-time waveforms are transmitting in the surface using mud pulse telemetry. Those waveforms contain check-shot information that helps the geophysicist and the engineer to place with accuracy the drill-bit on the seismic map and to obtain look-ahead information. As a result, the geological model is updating in real time and the depth uncertainty is reduced. Moreover, raw full waveforms are recorded in the tool memory and are processed after the drilling is over. The method is analytically described in section 2.4.

The three-component raw full waveforms recorded in the tool-memory are available for processing in this thesis project and the target Tex X in the Gulf of Mexico is under consideration (figure 1.1).

1.2 Thesis Objective

The main objective of the thesis is the processing analysis of the recorded-memory raw VSP-WD data. The interpretation of them is limited since there is no availability of well-log data, sonic-log or gamma-ray information, nor any other information that may cast light upon the geological model. Information is extracted from the resulting corridor stack and compared with the corridor stack of the real-time and recorded-memory data provided by Schlumberger. Furthermore, to the extent of my knowledge, there is not any case study available in the literature using this particular method. An effort has been made to adjust the available theories of other VSP methods to the needs of the current project.

1.3 Field Presentation

In August 2005, Schlumberger carried out a survey using the Vertical Seismic Profile While Drilling (VSP-WD) method on behalf of Devon Energy Production Company L.P. The field location is in the West Cameron Area in Offshore Louisiana and the well was number 4 in the block 537. The purpose of this well was to test two targets called Bul 1 (Tex X) and Rob E Sands. Those sands appeared to be productive in four neighbouring wells. A seismic anomaly named Mamba is located across the syncline and high to both of these areas. The well was severely deviated in order to encounter both targets. The primary objectives were at the measured depths of 3492.4 m and 4111.8 m. The total depth of the well was 4727.5 m.

The pre-drilling prediction of the target Tex-X was at 2.891 s in two way time (TWT) and at 11044.3 ft (3366.3 m) in true vertical depth. The target was detected at approximately 2888 ms.

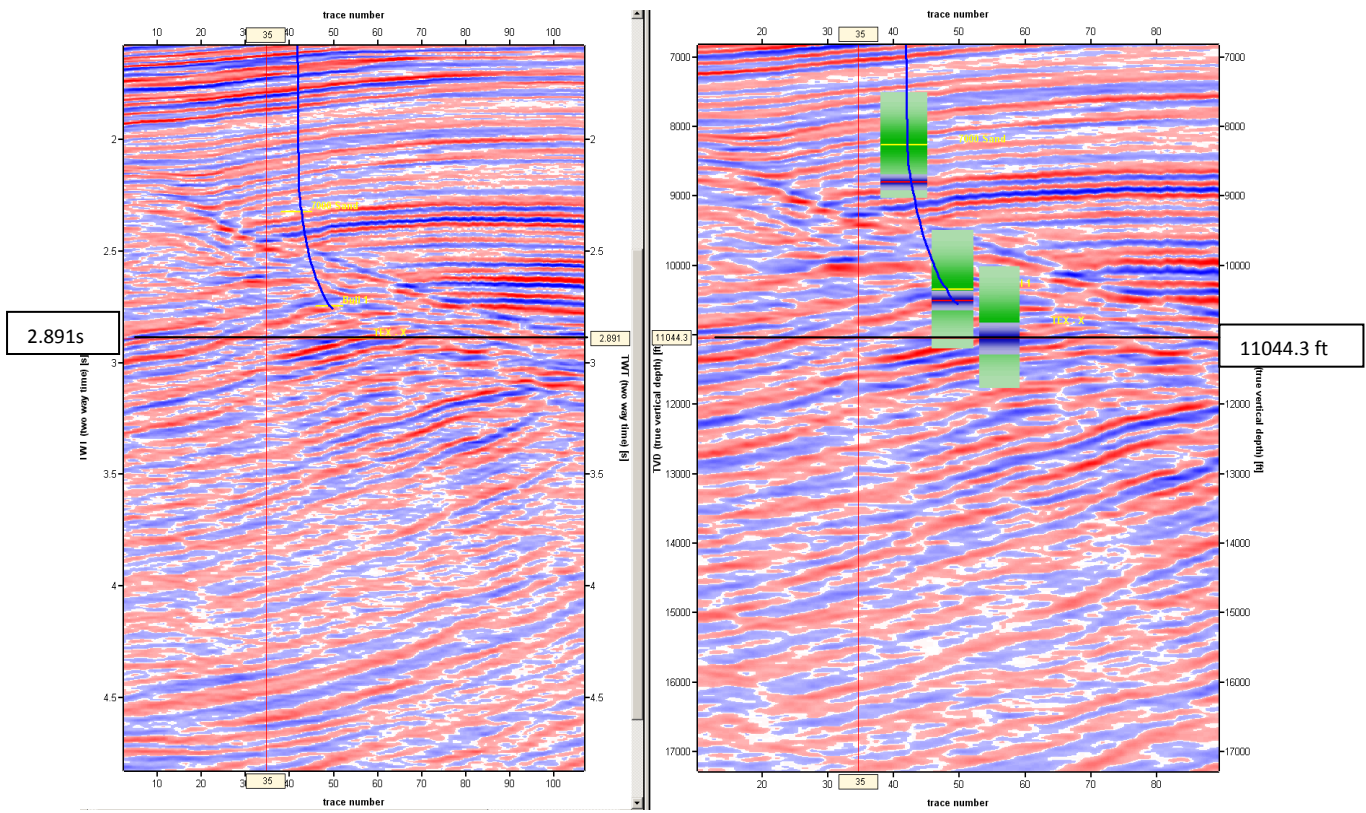


Figure 1.1: Location of the target Tex X Sand target provided by Schlumberger.

CHAPTER 2: Seismic While Drilling Methods

2.1 Introduction to SWD technology

Seismic While Drilling (SWD) has been a topic of interest to both drillers and geophysicists for a number of years. Borehole Seismic measurements are extremely useful for correlating drilled depth with seismic depth, setting coring and casing points, avoiding drilling hazards, and identifying, overpressure zones. In order to properly place the well that is being drilled in either the seismic time or depth section, an accurate travelttime-versus-depth profile is needed. Accurate knowledge of the location of a wellbore in seismic time or in depth is the primary objective of SWD (Althoff et al, 2004).

SWD can potentially be done either using a downhole source and surface receivers or using an active seismic source on the surface and the receivers downhole. VSP surveys have long been known to produce superior reflection images compared to images from surface seismic (Anchliya, 2006).

With the advance of PDC bits, the drill bit signal was found to be too weak to be used as a seismic source in many situations. In more recent SWD developments, downhole receivers are being used with a surface source. Because the drilling noise is in the frequency band of the seismic signal, the data should be acquired during a ‘quiet’ period of the drilling operation and not while the drilling activity is taking place.

Current implementation of SWD technology can best be described as a real-time checkshot survey, where the seismic travelttime from the source to the receiver is recorded downhole and sent to the surface in real time via mud pulse telemetry. This time-depth correlation provides extremely valuable information to update the seismic velocity profile and allows the proper positioning of the well in the seismic time section. Entire waveforms at the different receivers are recorded downhole for later retrieval. A complete VSP analysis, including reflections and corridor stacks for seismic ties and look-ahead applications, can be performed.

2.2 Historical Review of SWD Methods

In 1930, the idea to use the drill bit as a seismic source for investigating subsurface features came up. The original concept was cable tool drilling, which made processing a simple affair.

In 1968, an attempt to utilize the vibration signal from the drill bit was made by M. Chapuis, a geologist at Institut Français du Pétrole (IFP). He decided to record the noise disturbance from drilling with a geophone placed on the ground in the neighborhood of the rig.

In 1972, Jean Lutz at Elf Aquitaine, with his geoscientists and driller colleagues, improved this technique by fixing an accelerometer at the top of the drill-string. It measured bit vibration transmitted through the drill-string.

In the 1980's, Elf Aquitaine and CGG geophysicists realized that the accelerometer received a continuous signal similar to the surface geophone but with different speed so the two traces would be time shifted. By using cross correlation the value of this shift could be estimated.

In 1986, Western-Atlas published interesting results obtained onshore in North America in wells drilled by Amoco using the TomexTM-type SWD survey. This technique showed reasonably not satisfactory results when a PDC bit was used.

In the early 1990's, IFP tested its new TRAFOR MWD system, using a wire link to the surface through wired drill pipes, to analyze the downhole vibrations while drilling, in order to improve the safety of drilling operations. From 1990 to 2000 this technique was fully exploited and developed by IFP and its partners through various experiments.

In the year 1997, a Schlumberger project explored ways to look-ahead of the bit, trying to overcome the limitations of Drill-Bit Seismic. An experimental tool was built and then tested in Schlumberger test wells in 1998 with promising results. In 1999, BP and Schlumberger started collaborating on the trials of the seismic Measurements-While-Drilling (MWD) technique and successfully tested the

experimental tool at the Rocky Mountain Oilfield Test Center in Wyoming, USA. Schlumberger's engineers and scientists built and developed more tools and a new technique arose. This technique, named VSP-WD, employs an LWD tool containing seismic sensors, a surface seismic source and an MWD telemetry system to transmit information to the surface. Seismic energy is produced at the surface by a conventional seismic source, such as an air gun deployed off a boat or rig. The SeismicMWD* tool is placed downhole on the BHA to receive both the direct and reflected seismic energy originating from the source.

Recently SWD measurements took a new direction with the introduction of Swept Impulse tool by TEMPRESS®. The tool is capable of generating VSP in an inclined well with a PDC bit. Successful field tests were carried out by Tempress at Baker Experimental Test Area (BETA) with prototype tool (Althoff et al., 2004).

2.3 Vertical Seismic Profile

VSP surveys have long been known to produce superior reflection images compared to images from surface seismic. They can be used to gain insight into wavefield propagation (Lee and Blach 1983). Three-component geophones are lowered to the bottom of the borehole and a source is activated at the surface, at a certain distance away from the wellhead. Several shots are repeated for a certain depth level and then stacked together to produce one seismic trace. This procedure is repeated for different depth levels and, as a result, a group of traces are recorded in time yielding the VSP section.

Three components of the seismic wavefield can be recorded in situ over a range of depth levels. Both downgoing and upgoing waves are detected. The upgoing and downgoing seismic events can be identified at different points of their propagation path in depth and time. The arrival time of the downgoing waves is increasing as the depth of geophones increases, generating a positive slope. In contrast the arrival time of the upgoing events decreases as the depth of the geophones increases giving a negative slope.

Compared to surface seismic, the VSP is a tool that has special characteristics that enhance the quality and value of the seismic information:

1. Recording of the incident and reflected waveform fields
2. Improved vertical and horizontal resolution with information acquired in the Fresnel zone centered in the particular well and the highest frequency content
3. Detailed image of the objectives near the well
4. Reduce uncertainty in areas with marginal seismic data or without information.
5. Prediction of stratigraphy, lithology and the structure ahead of the bit to optimize drilling costs and reduce uncertainty (Gerardo et al, 2007).

Moreover, the VSP in a deviated borehole provides extensive lateral reflection coverage for structural and stratigraphic information. Also, the reflections are correlated directly to the measured depth and to the logs without performing a vertical depth correction on the logs or the synthetic seismogram. Finally, in comparison with a conventional velocity survey, it can provide this extensive high resolution reflection information away from the borehole for only an incremental cost (Gaiser, 1983).

On the other hand, the VSP data are limited in subsurface coverage and may have a substantial cost.

Table 2.1, the applications and the capabilities of the VSP in exploration and production procedures are summarized.

Table 2.1: The VSP in exploration and production

VSP	Exploration & Production
Application	Prospect evaluation & reservoir delination.
Capability	<ul style="list-style-type: none"> •Velocity and travelttime to depth. •Correlation of logs to seismic in depth. •High-resolution seismic data •Improve structural & stratigraphic interpretation. •Improve modelling parameters.

2.4 Vertical Seismic Profile While Drilling (VSP-WD)

The VSP-WD technique employs a downhole sensor incorporated in the borehole assembly (BHA), which receives seismic energy from a seismic source deployed on a source vessel (figure 2.1).

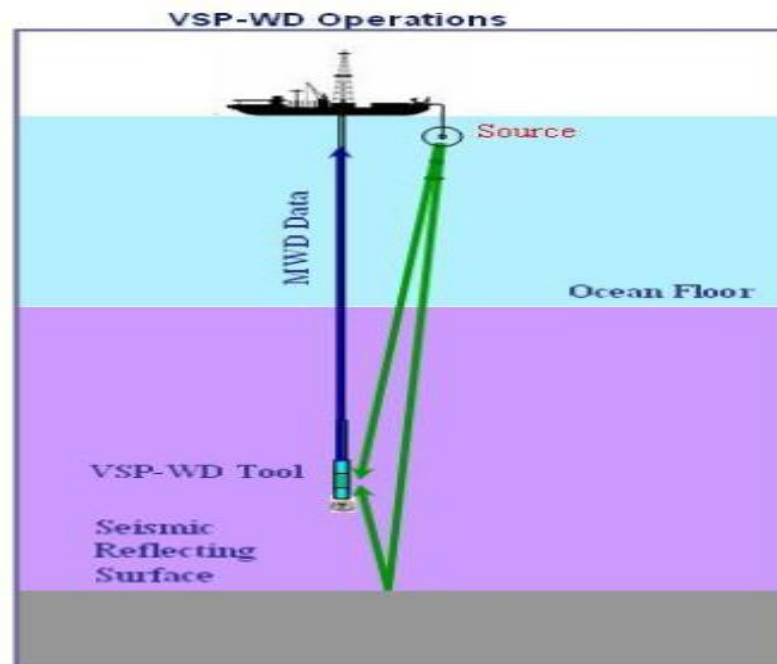


Figure 2.1: VSP-WD method (Anchliya, 2006).

The source is fired while drill-string connections are being made or during drilling pauses, while the mud circulation is stopped and drill-pipe is stationary so that drilling noise does not interfere with the data acquisition process. Seismic signals are received by the VSP-WD tool in a closely synchronized acquisition process by a conventional source such as an airgun offshore or dynamite or vibroseis on land. The tool can collect both the direct and reflected seismic waves. The downhole tool contains sensitive receivers, processors and memory (figure 2.2) (Anchliya, 2006).

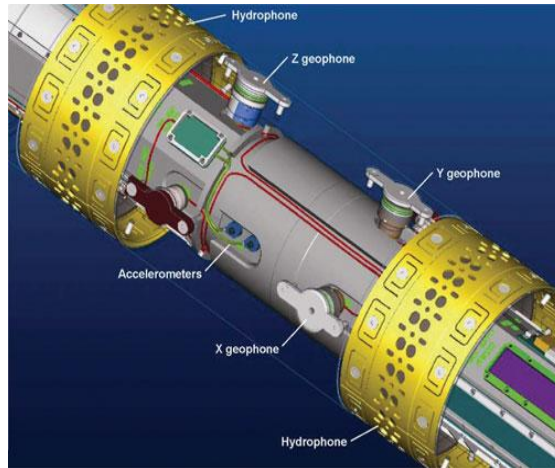


Figure 2.2: Receivers on the BHA (Hardage, 2009).

The signals are processed downhole to determine crucial first-break times, or check-shot times. The full waveform data were stored in memory during acquisition. In the downhole automated processing section, first-break times are picked together with an estimated signal/noise (S/N) ratio (Dethloff and Petersen, 2007). This information is then transferred uphole in real time by a mud pulse telemetry system. Current mud pulse telemetry systems do not have the required data transfer rates to send full-waveform data uphole (Anchliya, 2006).

Measurement While Drilling (MWD) systems measure formation properties (e.g. resistivity, natural gamma ray emission, porosity), wellbore geometry (inclination, azimuth), drilling system orientation (toolface), and mechanical properties of the drilling process. Traditionally MWD has fulfilled the role of providing wellbore inclination and azimuth in order to maintain directional control in real time. It transmits data to the surface by creating pressure waves within the mud stream inside the drillpipe. These pressure waves or pulses are detected at the surface by very sensitive devices that continuously monitor the pressure of the drilling mud. These data are passed on to sophisticated decoding computers which deconvolve the encoded data from downhole. This whole process is virtually instantaneous, thus enabling key decisions to be made as the wellbore is being drilled. These pulses or waves are propagated through the drilling fluid at roughly the speed of sound in mud (i.e. 4000-5000 ft/s or 1200-1500 m/s) (Baker Huges, 1997).

To prepare for the data-acquisition process, the tool is configured before it is run in on the BHA, with information relating to the recording schedule and acquisition. The

data recording schedule includes allowance for the trip-in, or sleep time, and the number of shots that will be processed. During tripping, the source can be activated while the tool is at desired depth. Seismic signals are recorded both directly from the source and reflected from the formations to be imaged. These signals are stored in tool memory for later processing. Immediately after acquiring the data, downhole processing determines the check-shot times. A complete procedural aspect of the tool is shown in figure 2.3 (Anchliya, 2006). Proper depths are assigned to the real-time data at the surface, and the time-depth pairs are used to locate the bit on the surface seismic section. All waveform information is stored in downhole memory and is retrieved at the surface after the bit run for VSP processing (Esmersoy et al, 2001). The technique depends largely on the geometry of the well and the source position. Vertical wells with zero offset sources work best for this application.

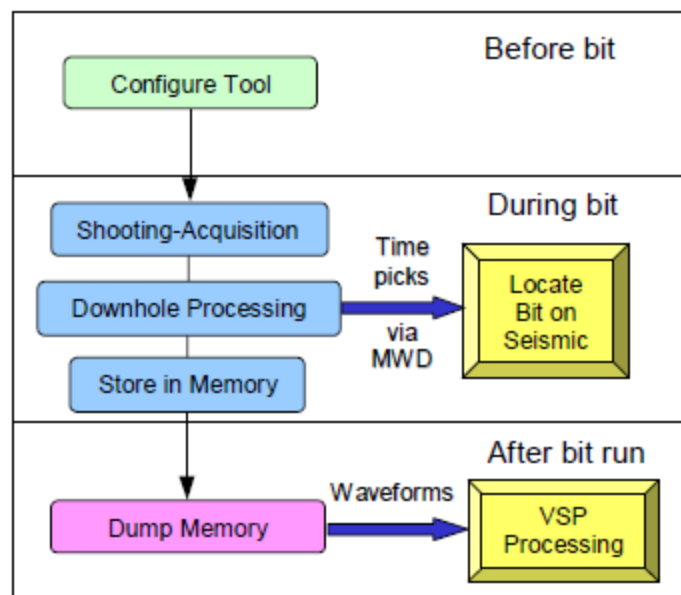


Figure 2.3: General operating procedures for VSP-WD surveys (Underhill et al, 2001).

2.4.1 Data Acquisition

The tool and surface clocks are synchronized and every 15 seconds an event window occurs (figure 2.4). The downhole tool checks at the start of this window to see if the pumps are on (drilling) and if so the tool goes back to sleep. If the pumps are off the tool then monitors the hydrophone and/or geophone signals to look for incident energy. At surface, the engineer decides whether to fire the airguns or not. If the

driller is making a connection and the downhole tool is stationary the engineer enables the automatic gun firing software. This fires the airguns exactly 15 seconds apart at the start of this window. The downhole tool analyses the incident energy and an algorithm decides whether there is a first break or not. If a shot is deemed to be good this is placed in a buffer. Whilst each shot is recorded in memory for later processing, the real-time measurement relies on at least 3 sequential shots to arrive at the tool at the same time offset in the window and also the same wave-shape. This is to avoid the tool triggering on noise generated by the rig. If at least 3 shots are seen the tool starts to stack the waveforms and continues to stack on each firing. Once the pumps resume, the tool calculates the first-break time from the stacked waveform, passes this to the MWD telemetry and is sent uphole immediately after the survey (Anchliya, 2006). The acquiring of data for the current project has been done by Schlumberger.

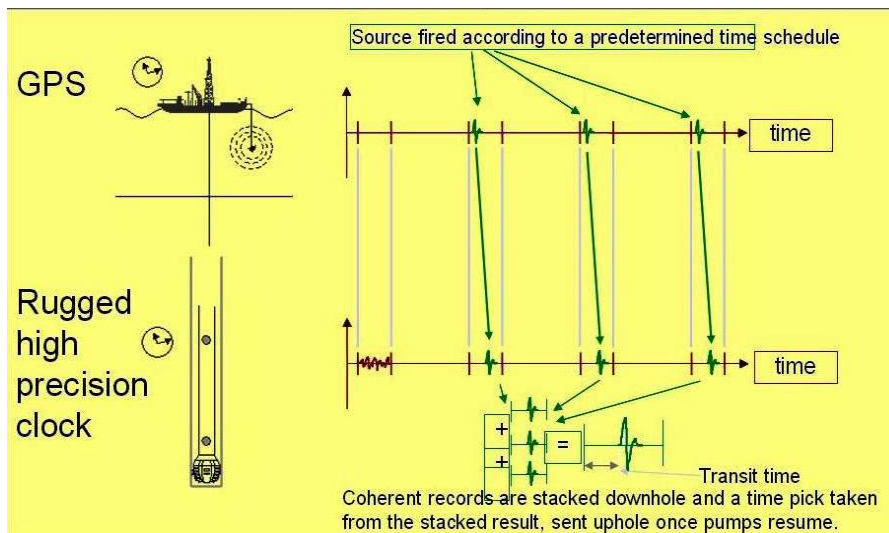


Figure 2.4: Acquisition timing of the tool (Anchliya, 2006).

2.4.2 Look Ahead Capability

The signals reflected in formations deeper than the total depth of the well are recorded ‘ahead of the bit’ by the geophones located close to the bottom of the well. In some cases, valid data has been observed up to 800m ahead of the bit. The technique of acquiring the information ahead of the bit and processing the information using the

last time-to-depth relation along with Inversion Techniques used to correlate the information, in depth, to the surface seismic ‘ahead of the bit’ is called VSP in Look Ahead Mode. The technique is used in an intermediate section of the well with the objective to predict the stratigraphy, lithology and structure ahead of the bit determining with less uncertainty the depth of the upcoming formations (Gerardo et al, 2007).

One of the main applications of the VSP-WD method is the “look ahead” prediction. The maximum “look ahead” depth is depending on the impedance contrast, design of the acquisition, and source strength (Hernández et al, 2007). Seismic source specifications are fundamental to the improvement of high resolution data, and to the detection of gas hazards (Price, 1990).

CHAPTER 3: VSP Processing

3.1 Introduction

For the processing, the VISTA® 2D/3D Seismic Data Processing Software (“VISTA”) by GEDCO has been used. The geometry of the survey demands the use of the Far-Offset-VSP processing flow of the particular software.

The Far-Offset-VSP processing flow is a conventional processing flow. At the beginning both a median and an $f-k$ filter has been used for the separation of the upgoing and downgoing waves. Afterwards, a waveshaping deconvolution that use the downgoing P waves took place in order to design the deconvolution operator to be applied to the upgoing P waves. Thereafter, an exponential gain has been applied for the amplitude recovery. Thereupon, shifting to the two way time by doubling the first-break time of the upgoing P waves has been completed and finally, the corridor stack has been resulted. The flow diagram in figure 3.1 show analytically the processing steps.

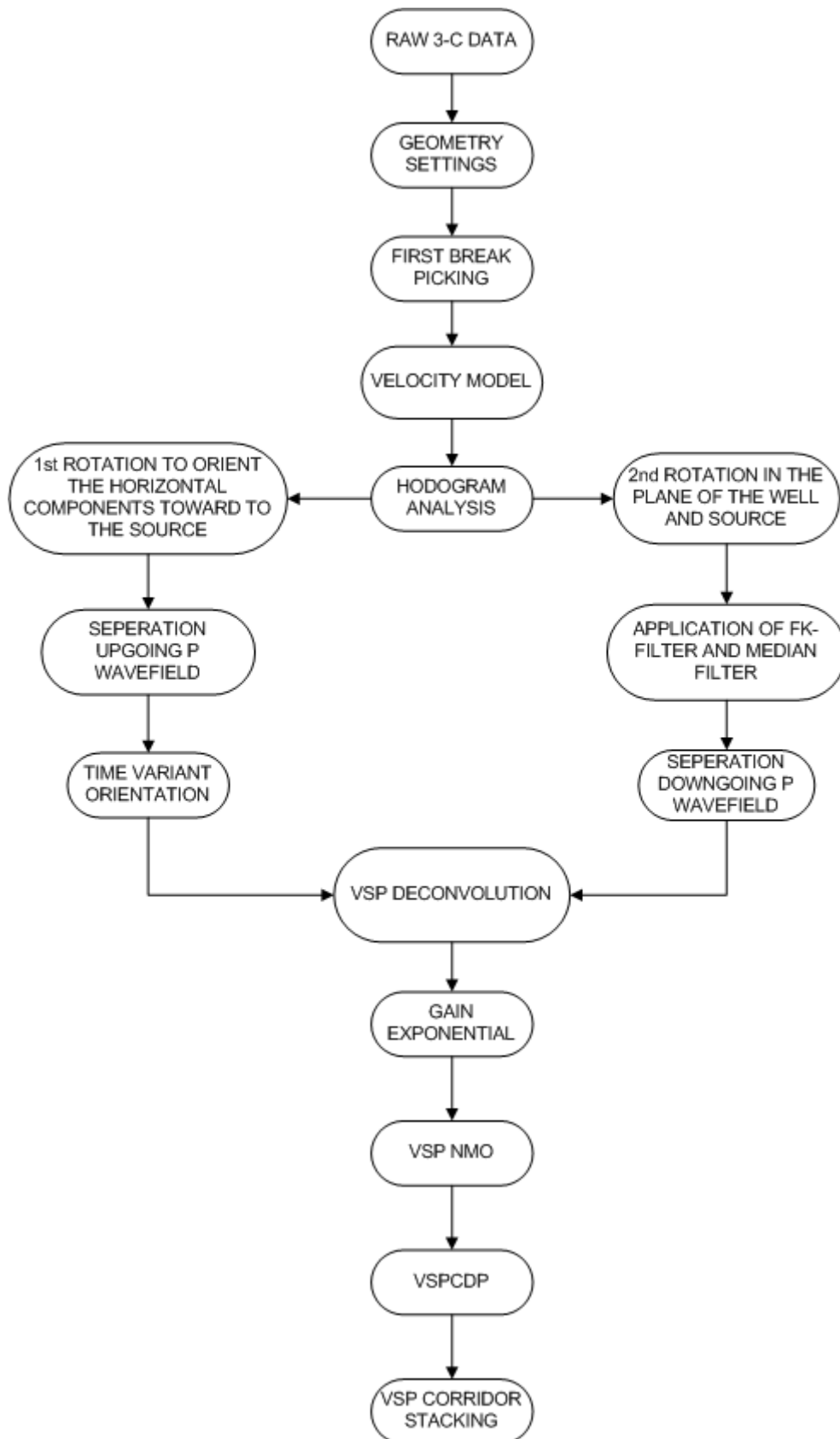


Figure 3.1: Flow Diagram showing the Processing steps.

3.2 Geometry

The drilling floor is the base ‘Kelly-bush’ (KB) level of the well, where the maneuvers are performed. This point define the geographic coordinates of the well. The two fundamental aspects of the geometry are the source and the receiver positions. The source position remain stable during the survey and is located 19.2 m away from the Kelly-bush and in depth of 4.57 m. The receivers are moving away from the source while drilling generating several angles of incidence. The three-component wavefield is recorded in situ over a range of depth levels. Totally, thirty-two number of traces (depth levels) has been recorded with a sample rate 2 ms. The range of the depth levels is from 2968.38 m to 3462.39 m in measured depth (MD) or from 2926.73 m to 3296.05 in true vertical depth (TVD). In deviated wells the drilling depth (or length of the well curve) differs from the vertical depth, which is calculated using the deviation data. In figure 3.2, the difference between true vertical depth and measured depth is presented. In figure 3.2a, the well is vertical and its measured depth (z drill) is equal to true vertical depth (z true). In the case of the deviated well in figure 3.2b, the depth differs from the measured depth (z drill) with the later to be larger than the true vertical depth (z true).

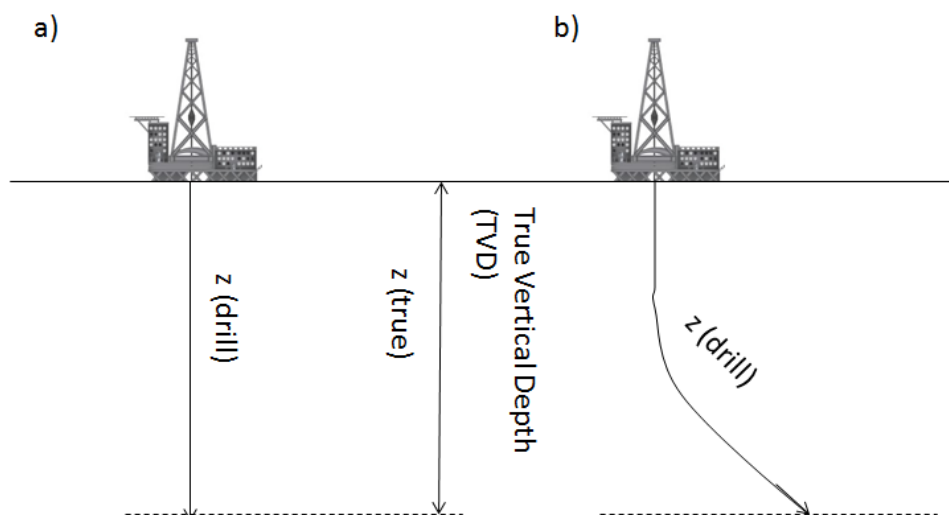


Figure 3.2: The difference between a) Measured Depth and b) True Vertical depth.

The resulting offset between source and receiver position is varying from 67.37 m to 361.6 m. The details of the VSP geometry is presented in the tables 3.1 and 3.2.

Table 3.1: Wellhead and source location.

X-Well (m)		Y-Well (m)	
0		0	
X-Shot (m)	Y-Shot (m)	Shot Depth (m)	Shot Elevation (m)
17.93	-6.88	4.57	0

Table 3.2: Vertical Seismic Profile geometry.

Level	MD (m)	TVD (m)	X-Receiver (m)	Y-Receiver (m)	Offset (m)	Tool Inclination	Tool azimuth
1	2968.38	2926.73	46.07	-68.10	67.37	16.80	124.00
2	3007.49	2964.23	52.85	-77.97	79.20	18.84	124.81
3	3026.03	2981.74	56.34	-83.06	85.31	18.87	122.34
4	3035.77	2990.88	58.17	-85.73	88.53	18.89	121.04
5	3055.07	3009.05	61.78	-91.21	95.05	19.46	119.91
6	3064.81	3018.19	63.59	-94.00	98.36	19.76	117.54
7	3084.21	3036.42	67.07	-99.60	104.94	21.11	115.45
8	3093.64	3045.32	68.73	-102.33	108.13	21.79	114.54
9	3113.37	3063.85	72.12	-108.19	114.89	23.55	113.80
10	3122.39	3072.32	73.66	-110.89	118.00	24.37	113.50
11	3142.44	3090.92	77.48	-117.66	125.77	25.93	113.69
12	3151.76	3099.39	79.31	-120.91	129.50	26.64	113.81
13	3171.51	3116.85	83.81	-129.11	138.86	28.23	114.14
14	3180.84	3124.87	86.01	-133.15	143.46	28.98	114.30
15	3200.58	3141.33	91.30	-142.81	154.46	29.46	114.17

Level	MD (m)	TVD (m)	X- Receiver (m)	Y- Receiver (m)	Offset (m)	Tool Inclination	Tool azimuth
16	3209.94	3148.89	93.87	-147.52	159.83	29.66	114.10
17	3229.65	3164.12	99.97	-158.34	172.25	30.04	114.10
18	3238.97	3171.32	102.92	-163.57	178.25	30.21	114.10
19	3258.79	3185.71	109.79	-175.40	191.93	31.55	114.99
20	3268.11	3192.26	113.09	-181.05	198.47	32.21	115.44
21	3297.21	3211.68	124.33	-199.56	220.10	34.18	116.87
22	3316.95	3223.49	132.74	-212.93	235.88	35.71	117.80
23	3326.00	3228.90	136.69	-219.15	243.23	36.42	118.22
24	3326.27	3229.05	136.80	-219.34	243.45	36.44	118.22
25	3346.01	3239.08	145.81	-233.70	260.39	37.97	118.61
26	3355.33	3243.53	150.12	-240.58	268.50	38.70	118.80
27	3375.10	3252.64	159.30	-255.41	285.92	40.29	119.53
28	3384.42	3257.00	163.63	-255.41	294.17	41.18	120.07
29	3404.22	3266.54	172.81	-277.14	311.49	43.06	121.23
30	3413.54	3271.22	177.12	-284.04	319.62	44.03	121.89
31	3442.45	3285.71	190.47	-305.12	344.55	47.42	122.86
32	3462.39	3296.05	199.70	-319.47	361.60	49.41	122.90

The extracted seismic is an arbitrary line along the borehole, not in the either inline or xline direction and so it is not regularly spaced. A view of the line over which the seismic wavefield is recorded is shown in figure 3.3. The red point represent the position of the source, thus the blue point shows the Kelly-bush. The receivers are the green points and shows clearly the path of the well.

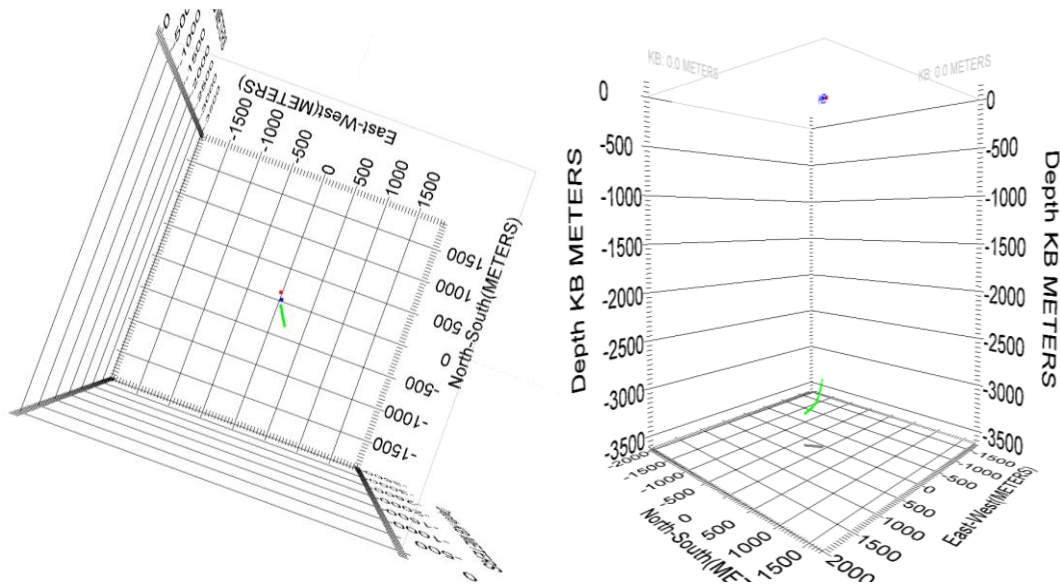


Figure 3.3: The top and side view of the well path.

The dataset consists of three component raw wavefield files X, Y and Z. The raw data X and Y consist the horizontal components ,thus, the raw Z file present the vertical one. The importance to employ three-component geophones in VSP surveys was searching and analyzing by Stéphane Labonté in 1990 and briefly presented in the next section.

Each of the raw data wavefield has a characteristic Trace-ID Code. Specifically, the Raw X file has a Trace-ID Code equal to 1, the Raw Y file equal to 2 and the Vertical file equal to 3. Consequently, the component is expressed by the number of the Trace-ID Code as it is presented in the table 3.3. This is the way that the software recognize the separation among the three components in the Raw data and so the division of the Trace-ID Code is a fundamental aspect .

Table 3.3: Component representation by the Trace-ID Code.

	Raw X	Raw Y	Raw Z
Component	1	2	3

The dataset has been provided for the current project, was already separated in the three Raw wavefield files. Compressional (P), shear vertical (SV) and the shear horizontal (SH) ray paths are depicted. Depending upon the developing angles that the various modes have with X, Y and Z axis of the geophone package, these wave modes

will be divided among the three downhole geophone axes. Consequently, the Z-axis geophone will record a combination of P and SV energy. Similarly the X- and Y- axis geophone will record some P-wave energy (Hinds et al).^(R.C. Hinds)

The raw stacks of shots at each level, for each of the three components are shown in figures 3.4, 3.5 and 3.6. The quality of the data recorded is good with high signal-to-noise ratio .

The Z component show mainly downgoing P wave. The signature is consistent with no character variation with increasing depth, apart from the traces 1, 4 and 32.

The X component recorded weaker first P arrivals. The signature has some character variation and the phase of the first P arrivals shows changes with the depth.

The Y signal-to-noise ratio is a little bit poorer compare to the other components. This may happen since the Y axis lies perpendicular to the vertical plane of the well, which should wholly contain the P and SV motion if the well were pointing exactly in the true dip direction for all interface (Knight, 1987).

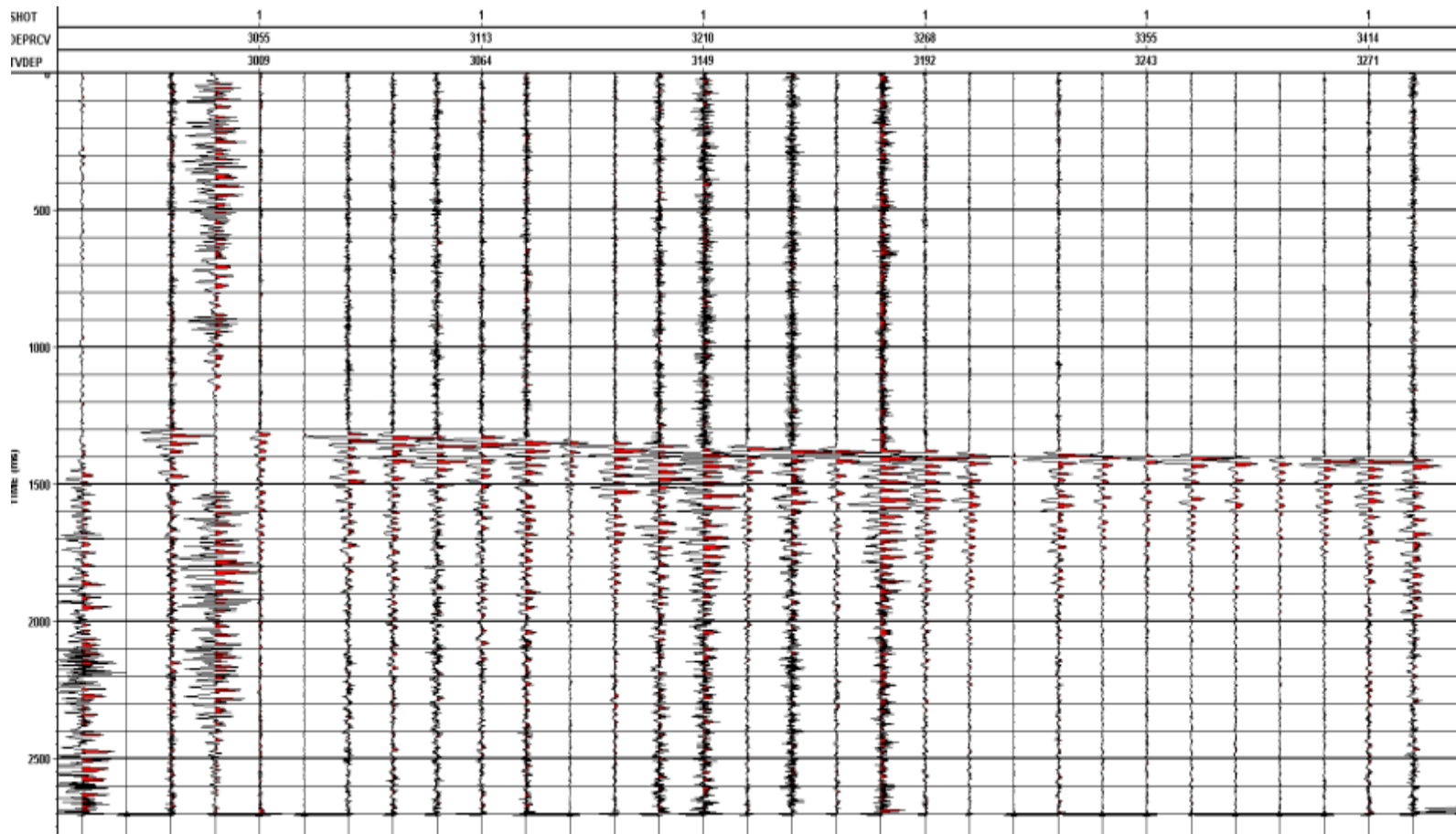


Figure 3.4: Raw X wavefield.

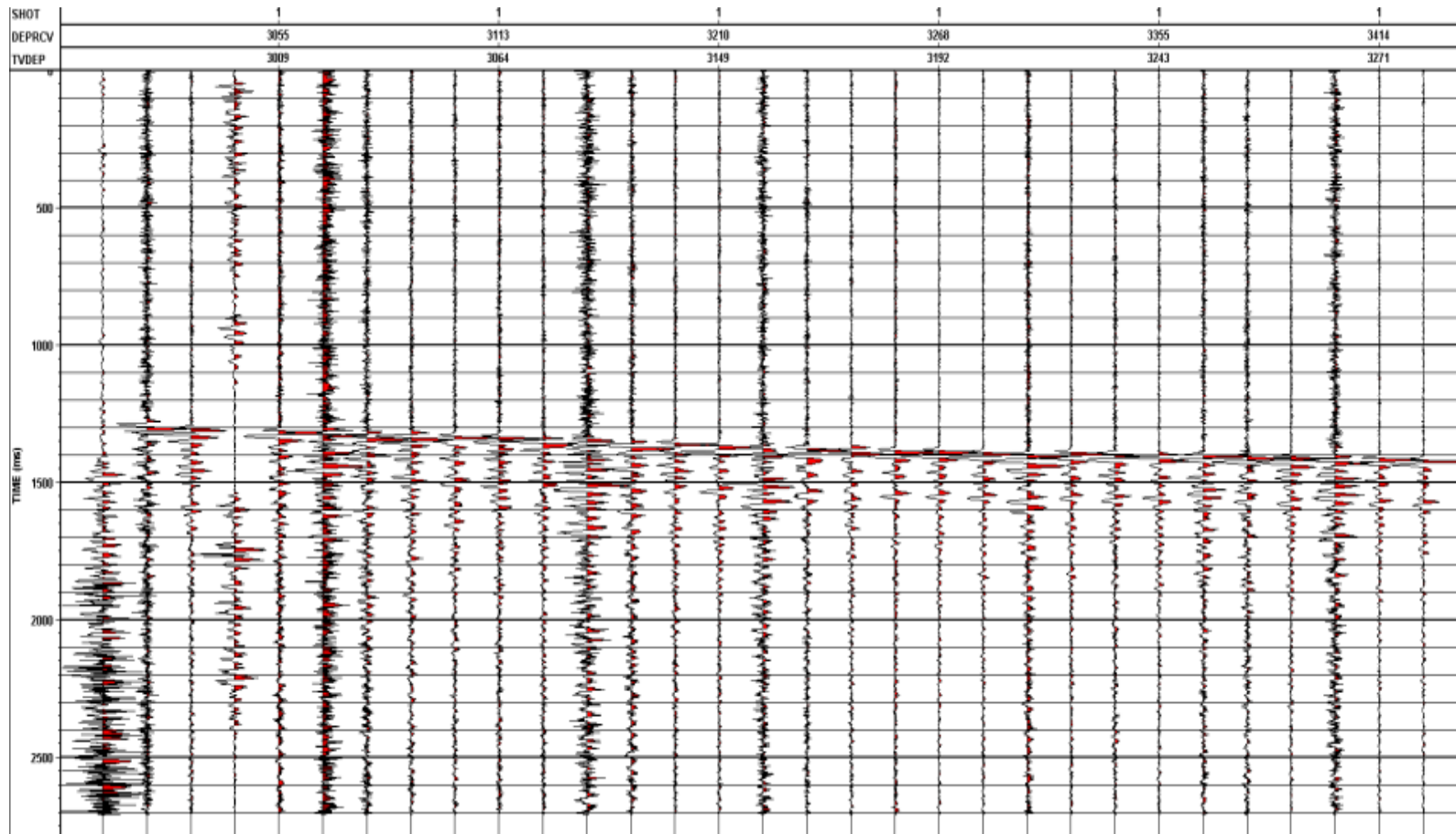


Figure 3.5: Raw Y wavefield.

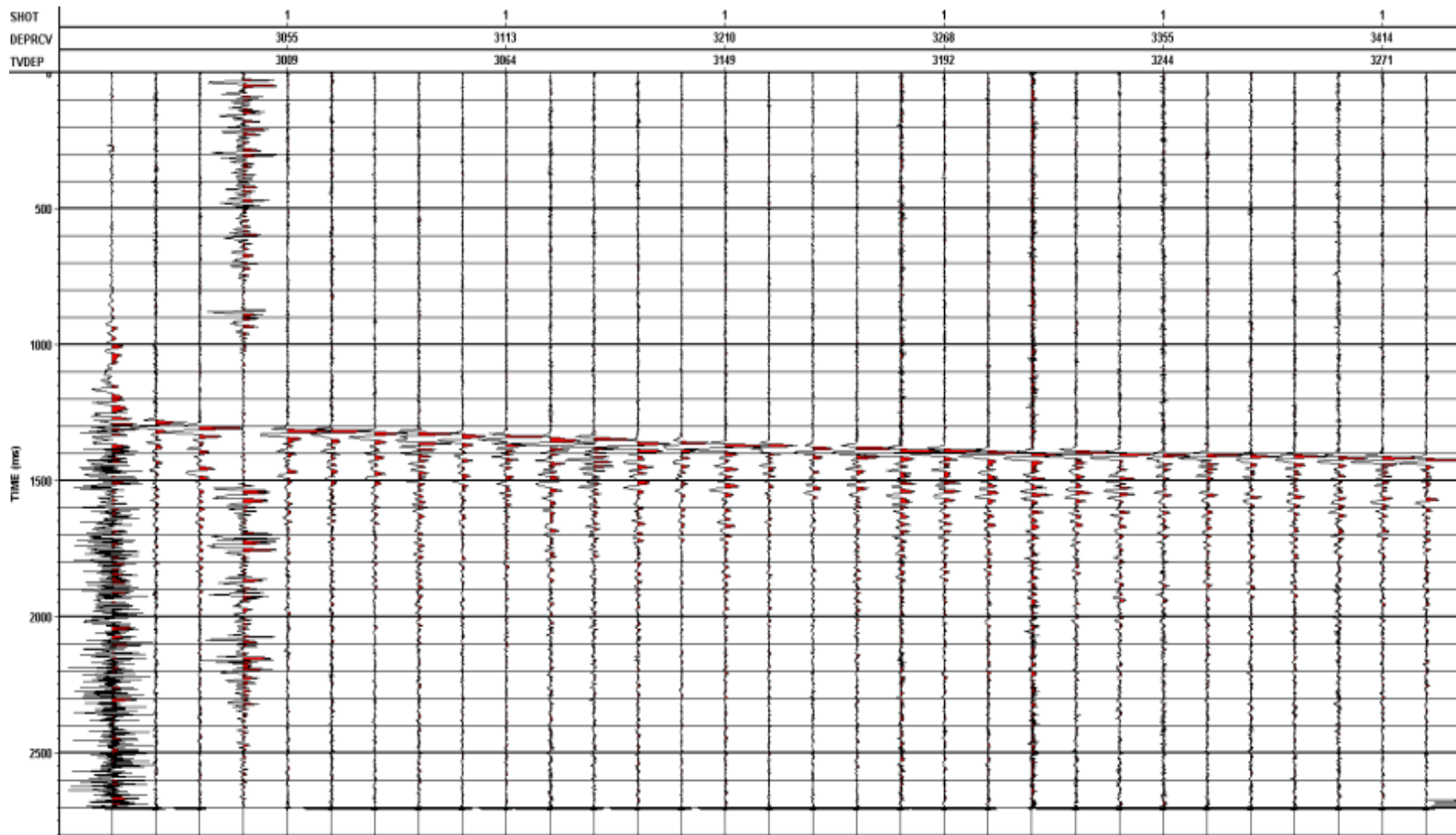


Figure 3.6: Raw Z or Vertical wavefield.

3.2.1 The importance of using three-component geophones

In vertical seismic profiling, the large variation in angles of incidence at the geophones location and the presence of considerable amounts of compressional (P) and shear (S) waves in the propagating wavefield, requires the use of three-components (3-C) geophones for full wavefield understanding.

In figure 3.7, a cross-sectional view of a VSP ray path geometry in a deviated borehole is presented. The propagating wavefield and the arrival times at the geophone locations can become really complex. The waves shown in this figure have been drawn in this way for the clarity of the picture. It should be noticed that every single geophone receives all the waves that are illustrated. The propagation wavefield includes:

1. Direct P waves
2. Downgoing P waves converted to downgoing S waves at geological interfaces
3. Downgoing P waves converted to upgoing SV waves at the reflection point
4. Downgoing P waves converted to upgoing P waves at the reflection point

At shallow receiver depths, the angle of incidence of a downgoing P or S wave is closer to horizontal than when the geophone is located deeper in the hole where its angle of incidence is closer to vertical. As concern the upgoing P or S waves, their angles of incidence are closer to vertical at shallow receiver depth than at greater depths where their angles of incidence is further from the vertical. Because of the variation in angles of incidence, P waves are partially on the horizontal channel and this part of this signal would not be recorded without a horizontal geophone. Also, shear waves are partly on the vertical geophone and cannot be fully separated without all components.

In order to record the full wavefield, a vertical and radial geophone are needed to record the vertical and radial components of the propagating wavefield. By doing so, the P-wave section can be improved over the conventional method of vertical

component recording, and an attempt can be made at reconstructing the S wavefield (Labonté, 1990).

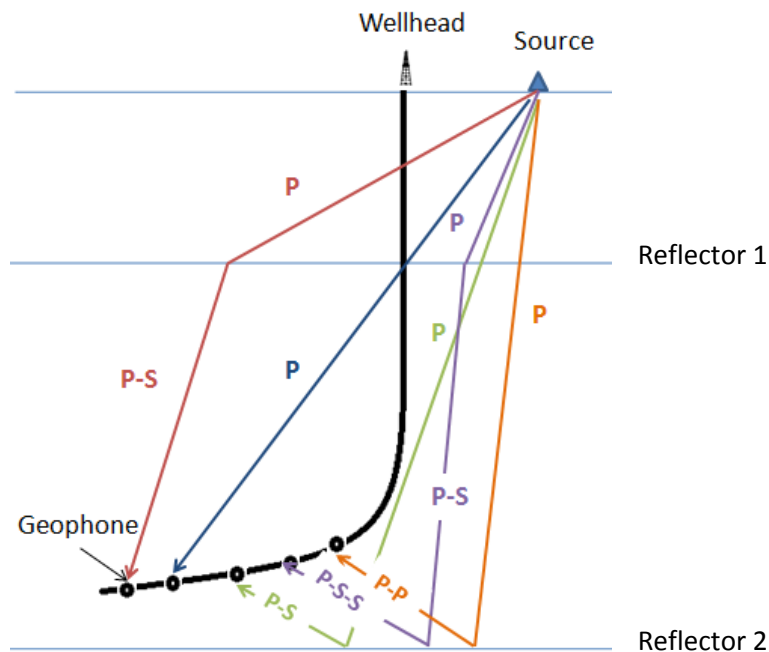


Figure 3.7: Deviated VSP ray path geometry.

3.3 First-Break Picking

The first breaks are the first energy that arrives at each depth, the downgoing energy that propagates in a direct line from the shot. Picking is a basic step of VSP-WD data processing. First-break picking is used while drilling to help in three areas:

1. VSP-wavefield separation and processing.
2. Time/depth checkshot analysis and geological model update.
3. Focused-data processing and S/N improvement (Poletto and Miranda , 2004).

The quality and repeatability of the direct arrivals is a basic aspect of picking. The first arrival times enable a determination of the true vertical depth-versus-time curve and a calculation of interval velocities. The amount of offset is taken into account when calculating velocities. In marine applications picking the first arrival is usually straightforward because the source energy level remains constant, as does the medium

surrounding the source. In addition the shot elevation remains relatively constant, and the geometry is such that offsets away from the wellbore usually increase in an even progressive manner (Kuzmiski et al, 2009).

Picking of first arrivals can be achieved automatically or manually. The first break times (FBP) were picked on the raw vertical Z component by searching the first arriving energy on each trace in the time-window, as is shown in figure 14. The first break time is picked as the first strong trough in the downgoing P-wave trace. It is important to mention that the FBP's from the Vertical component have been used for the X and Y component data. This suggestion is made as the signal-to-noise is usually poor on these latter data sets (figures 3.8 and 3.9).

The small discontinuities along the first breaks are due to the gaps in the depth levels. There is a very small (almost negligible) change in the slope due to a change in level spacing from 9 m to 20 m. As was described in a previous section, the shot is activated while a new well pipe is added (quiet period), the length of which is 20 m.

The first break picking has been avoided on four traces. Analytically, traces 1 and 4 show incoherent signal, which makes it difficult, if not impossible, to detect the first arriving energy. Furthermore, trace 24 was not included in the picking. The depth of this trace is significantly close to the depth of trace 23. Specifically, trace 23 has true vertical depth equal to 3228.9 m and trace 24 to 3229.05 m. That makes the velocity model to appear false velocity spikes with negative value. Finally, trace 32 was avoided since it does not show any signal.

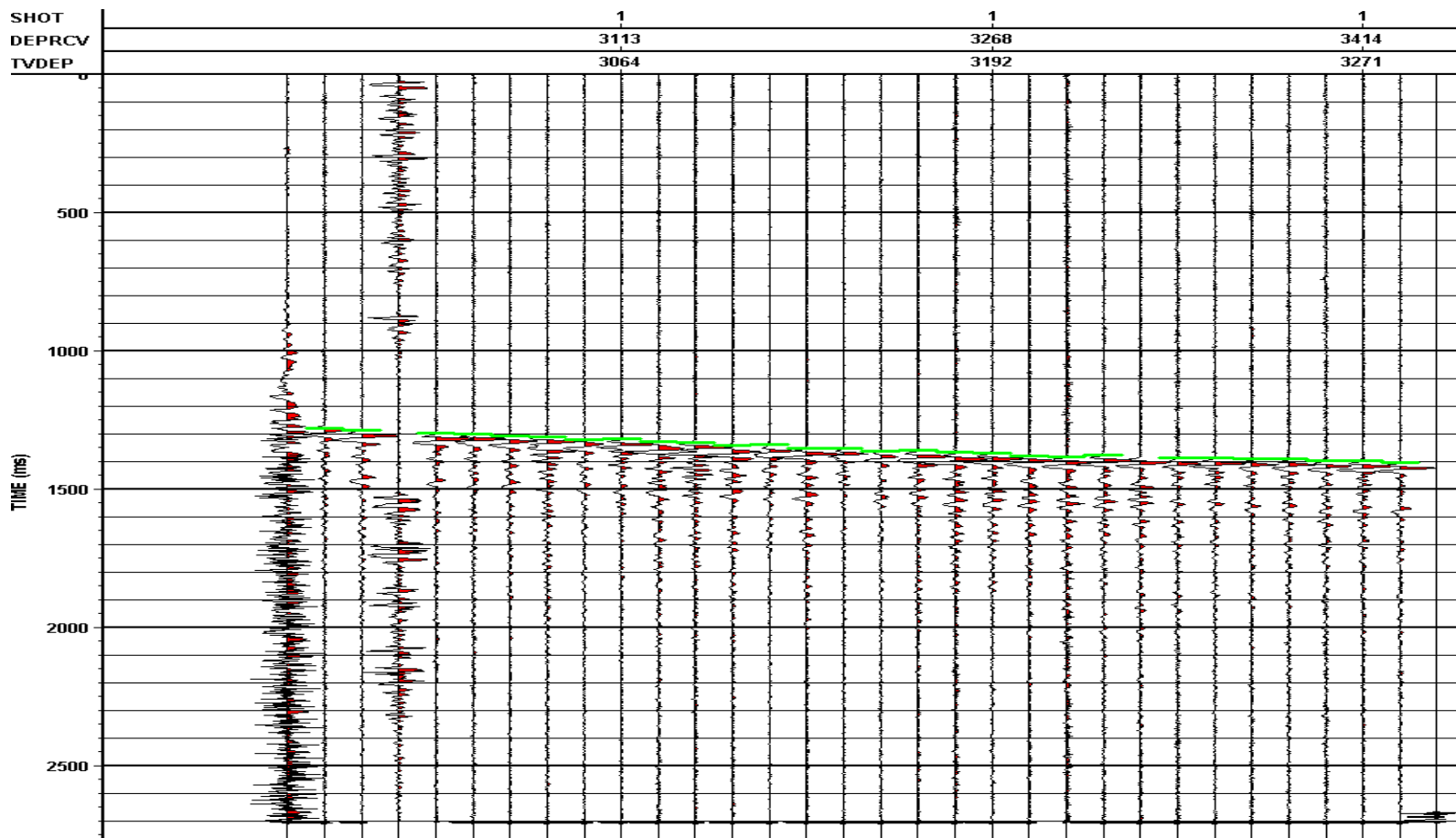


Figure 3.8: Raw Vertical Z with the first-break picking.

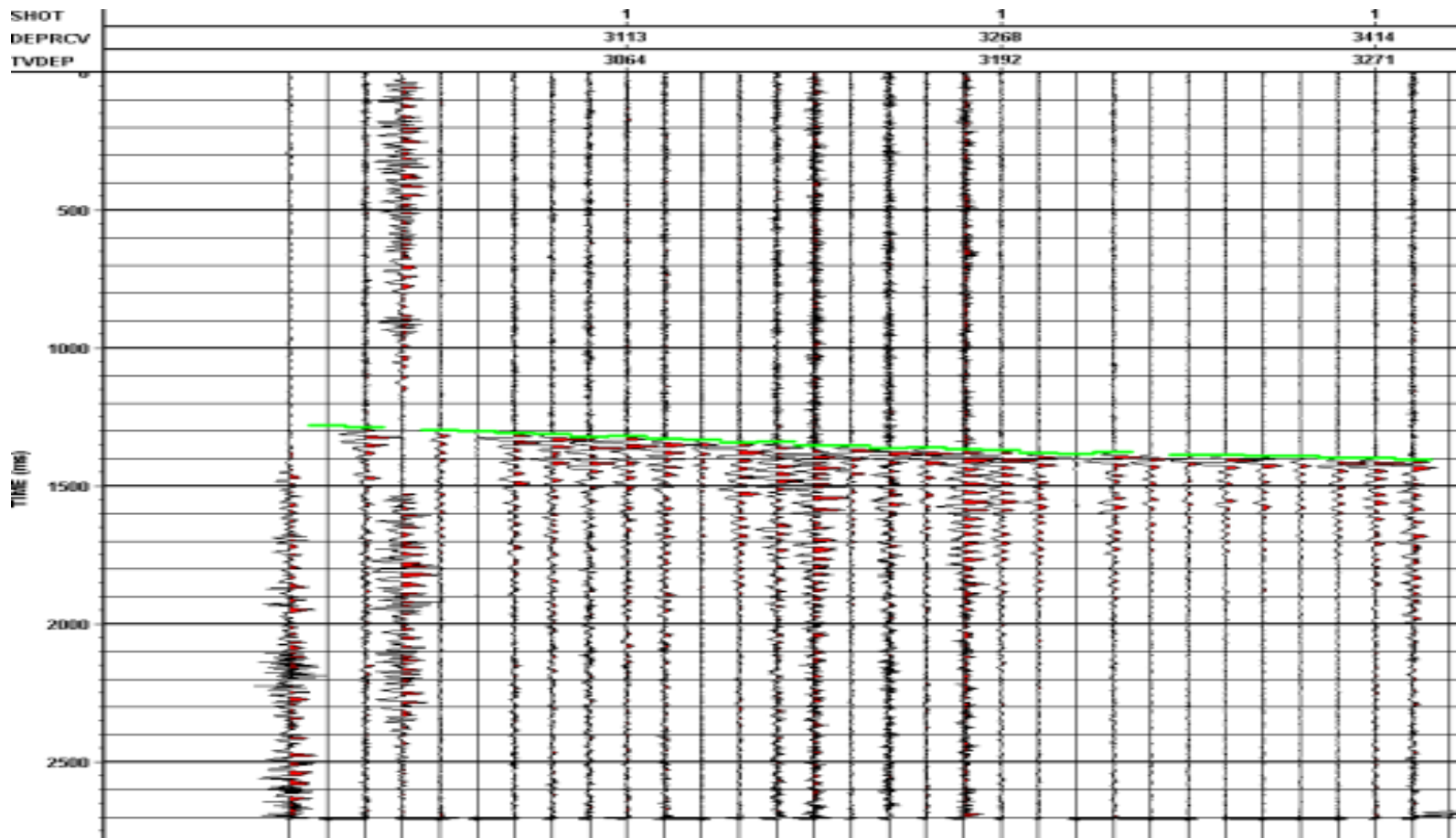


Figure 3.9: Raw X with the first-break picking transferred by the Raw Vertical Z.

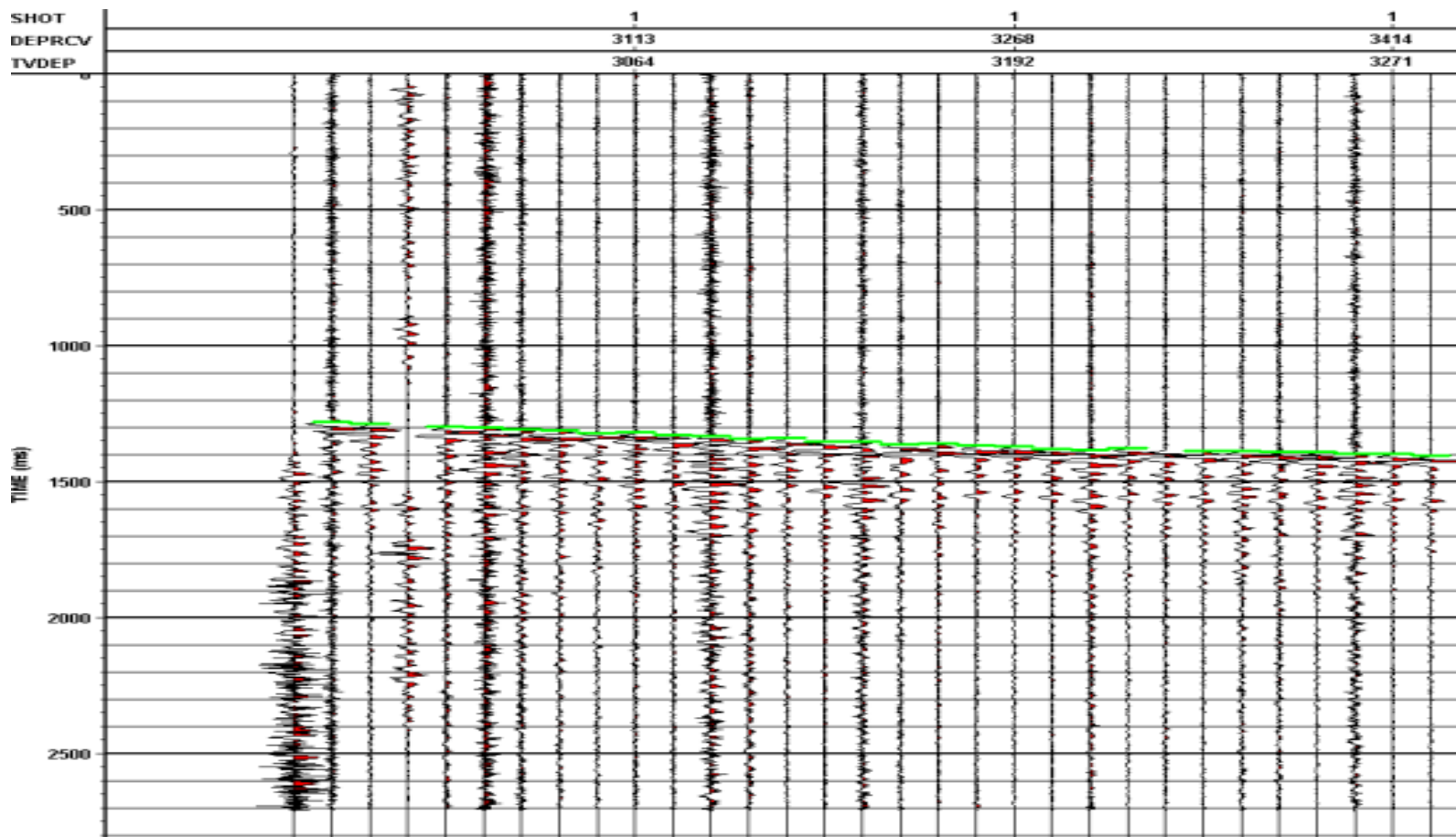


Figure 3.10: Raw Y with the first-break picking transferred by the Raw Vertical Z.

The first-break times that were picked for each depth level are presented in table 3.4. Furthermore, the times of the breaks were plotted as a time-depth chart, with the true vertical depth shown down the vertical axis and time shown horizontally (figure 3.11). Moving down the scale to a depth and across to the curve, the time for that depth can be read.

Table 3.4: First break times for each depth level.

Level	TVD	FBP
1	2964.23	1280.00
2	2981.74	1287.00
3	3009.05	1298.00
4	3018.19	1301.00
5	3036.42	1308.00
6	3045.32	1311.50
7	3063.85	1318.40
8	3072.32	1321.30
9	3090.92	1329.30
10	3099.39	1332.80
11	3116.85	1340.20
12	3124.87	1343.50
13	3141.33	1351.00
14	3148.89	1354.00
15	3164.12	1360.00
16	3171.32	1362.60
17	3185.71	1367.70
18	3192.26	1370.00
19	3211.68	1377.00
20	3223.49	1380.00
21	3229.05	1382.00
22	3239.08	1385.50
23	3243.53	1386.50
24	3252.64	1390.70
25	3257.00	1392.00
26	3266.54	1396.00
27	3271.22	1398.00
28	3285.71	1404.00

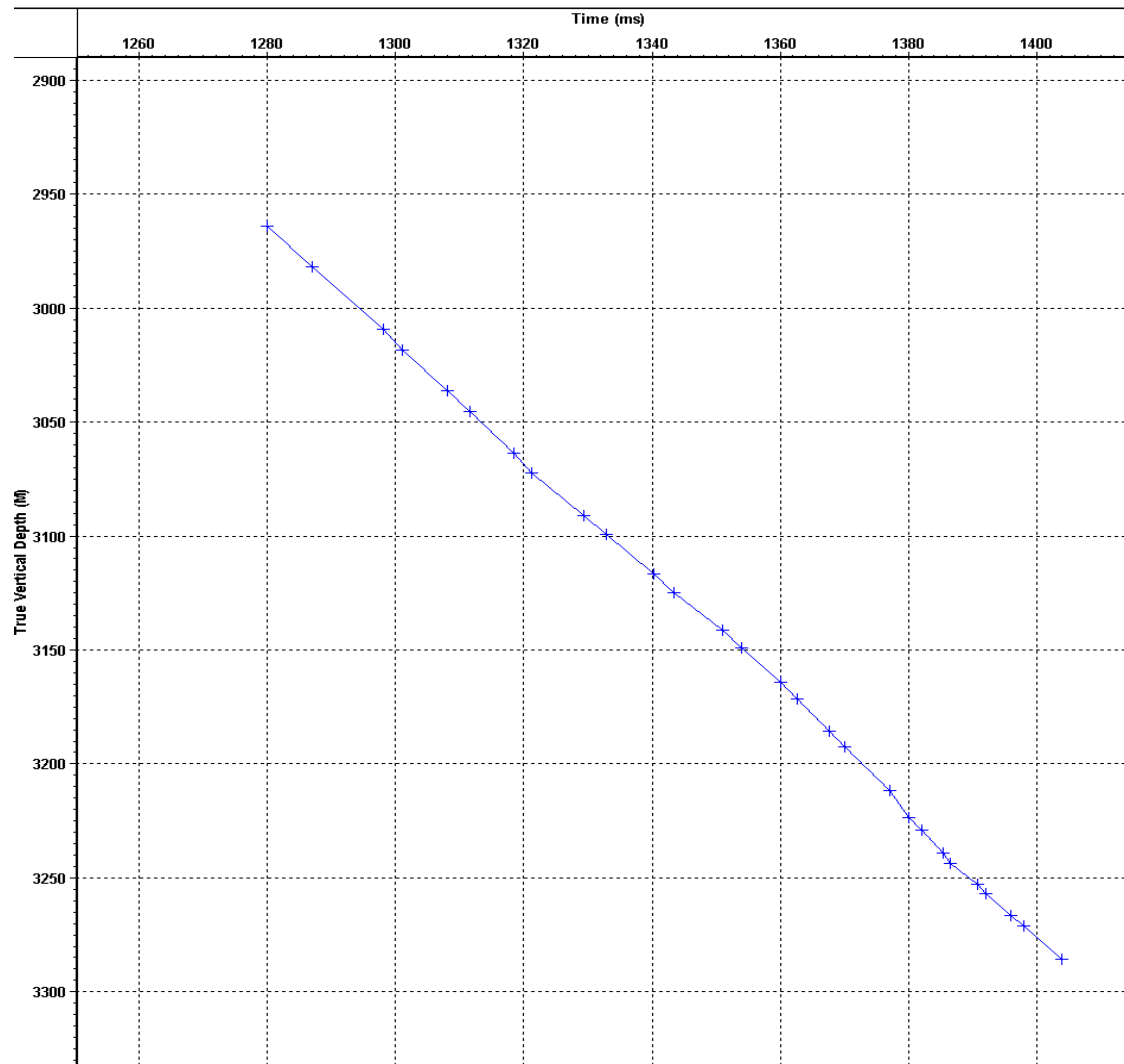


Figure 3.11: Time-depth chart.

3.4 Velocity Profile

A principal use of VSPs is to determine the variation of seismic velocity with the depth (Stewart,1984). Thus, the interval velocities, the average velocities and the root-mean-square (RMS) velocities for the P waves were calculated. The average velocities, \bar{V} , were calculated straightforwardly by dividing the true vertical depths by the picked first-break times at each depth level. Likewise, the RMS velocity, V_{RMS} , refers to a specific path. The RMS velocities are typically a few percent larger than the corresponding average velocities. The interval velocity V_i is the average velocity over the interval between two receivers. It calculated using the Dix velocity equation. The equations that represent those velocities are presented below.

- Average velocity: $\bar{V} = \frac{\sum_f V_f \Delta t_f}{\sum_f \Delta t_f}$ Eq. 3.1

where $V_f \Delta t_f$ represent the true vertical depth over a specific receiver.

- RMS velocity : $V_{rms} = \frac{\sum_f V_f^2 \Delta t_f}{\sum_f \Delta t_f}$ Eq. 3.2

- Dix equation for the interval velocities:

$$V_i^2 = \frac{V_{rms_n}^2 t_n - V_{rms_{n-1}}^2 t_{n-1}}{t_n - t_{n-1}} \quad \text{Eq. 3.3}$$

where t_n is the zero-offset travel time (or the picked first break time) corresponding to the depth of the n th receiver (true vertical depth) (Geldart et al, 1995).

In table 3.5 the P-wave velocities are presented. It is observed that the average and RMS velocities increase with the depth. The average velocity ranges from 2313.10 to 2349.8 m/s, thus the RMS velocity is slightly higher and is varying between 2313.10 and 2355.50 m/s. Moreover, the interval velocity demonstrates a range approximately from 2300 to 2700 m/s with three exceptions where the velocity appears to increase rapidly. Those picks of the velocity are on the levels 4, 17 and 22 with velocities equal to 3091 m/s, 3106.9 m/s and 4111 m/s respectively.

Table 3.5: Variation of P-wave velocities with the depth.

Level	MD (m)	TVD (m)	FBP (ms)	Velocity Interval (m/s)	Velocity Average (m/s)	Velocity RMS (m/s)
1	3007.49	2964.23	1280.00	2313.10	2313.10	2313.10
2	3026.03	2981.74	1287.00	2526.50	2314.20	2314.30
3	3055.07	3009.05	1298.00	2510.20	2315.80	2316.00
4	3064.81	3018.19	1301.00	3091.00	2317.60	2318.00
5	3084.21	3036.42	1308.00	2638.10	2319.30	2323.80
6	3093.64	3045.32	1311.50	2576.40	2320.00	2320.50

Level	MD (m)	TVD (m)	FBP (ms)	Velocity Interval (m/s)	Velocity Average (m/s)	Velocity RMS (m/s)
7	3113.37	3063.85	1318.40	2745.30	2322.20	2322.90
8	3122.39	3072.32	1321.30	2867.70	2323.40	2324.30
9	3142.44	3090.92	1329.30	2377.10	2323.70	2324.60
10	3151.76	3099.39	1332.80	2464.20	2324.10	2325.00
11	3171.51	3116.85	1340.20	2443.60	2324.70	2325.60
12	3180.84	3124.87	1343.50	2363.90	2324.80	2325.70
13	3200.58	3141.33	1351.00	2324.80	2324.80	2325.70
14	3209.94	3148.89	1354.00	2423.90	2325.00	2325.90
15	3229.65	3164.12	1360.00	2782.00	2326.90	2328.00
16	3238.97	3171.32	1362.60	2621.10	2327.50	2328.60
17	3258.79	3185.71	1367.70	3106.90	2330.10	2331.70
18	3268.11	3192.26	1370.00	3067.20	2331.30	2333.00
19	3297.21	3211.68	1377.00	3399.90	2335.70	2338.40
20	3316.95	3223.49	1380.00	3171.10	2338.00	2341.10
21	3326.27	3229.05	1382.00	3623.50	2339.40	2342.90
22	3346.01	3239.08	1385.50	4111.00	2342.50	2347.20
23	3355.33	3243.53	1386.50	3453.40	2343.60	2348.50
24	3375.10	3252.64	1390.70	3040.00	2345.10	2350.20
25	3384.42	3257.00	1392.00	2693.10	2345.50	2350.60
26	3404.22	3266.54	1396.00	3147.00	2347.20	2352.70
27	3413.54	3271.22	1398.00	2787.20	2347.80	2353.20
28	3442.45	3285.71	1404.00	2914.10	2349.80	2355.50

In figure 3.12, a combined graph of the time-depth chart and the generating velocity profile in m/s is illustrated. The time-depth curve is shown in the left part of the picture, thus, the velocity curves are demonstrated in the right part. The blue line represent the average velocity that shows clearly an increase with the depth. The interval velocities are represented in red color, which makes visible the changes with the depth.

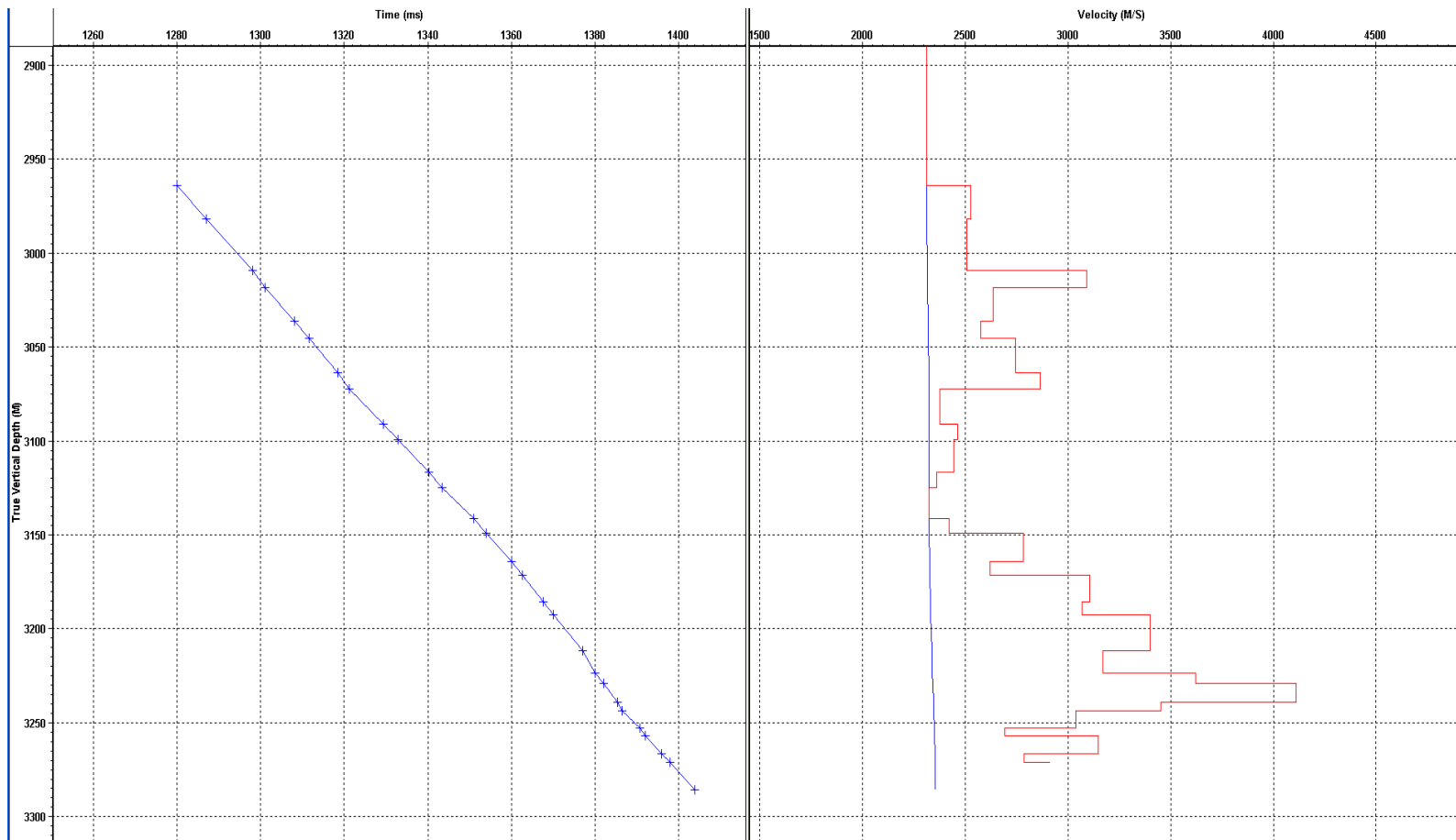


Figure 3.12: On the left side the time-depth curve is shown. In the right part the average velocity curve (blue line) and the interval velocity curve (red line) are illustrated.

3.5 Hodogram Analysis

After the first-break picking, two Hodogram Rotations are required for optimum Far Offset processing. As the sonde with the triaxial geophone package is lowered down the borehole, the VSP tool containing the geophone package will rotate and the X and Y channels will change orientation due to the deviation of the borehole. In the processing sequence, various numerical pseudo-rotations are needed to redistribute the P, SV and SH energy back onto separate channels. These numerical rotations or redistributions of the recordings from the three geophone axes onto newly orientated axes are called the polarization or hodogram analysis (Hinds et al).

The first Hodogram Rotation represents the rotation of the two horizontal components of the wavefield so that one of them is always oriented toward the source and the other always oriented perpendicular to the source-receiver line. The radial component is called H_{\max} , while the component orthogonal to the H_{\max} (transverse component) is called H_{\min} . The transverse component captures the SH (horizontally polarized shear) wavefield as well as out-of-plane reflections. The radial component captures the remaining wavefield consisting of downgoing P and SV and up-going P and SV waves.

An analysis window of one wavelength along the first arrival is used. In figure 3.13, the Hodogram at 3271.22 m depth is shown in reverse polarity, while in figure 3.14 the Hodogram at 3257.09 m depth in normal polarity is illustrated. The reversed polarity will be corrected after the hodogram analysis and data rotation. At each depth level, a Hodogram is produced. In Appendix A, the hodograms of the thirty-two depth levels are illustrated. It has to be noticed that since first-break picking has not been made on four traces (1, 4, 24 and 32), as mentioned in previous section, the produced Hodograms of them show a chaotic pattern.

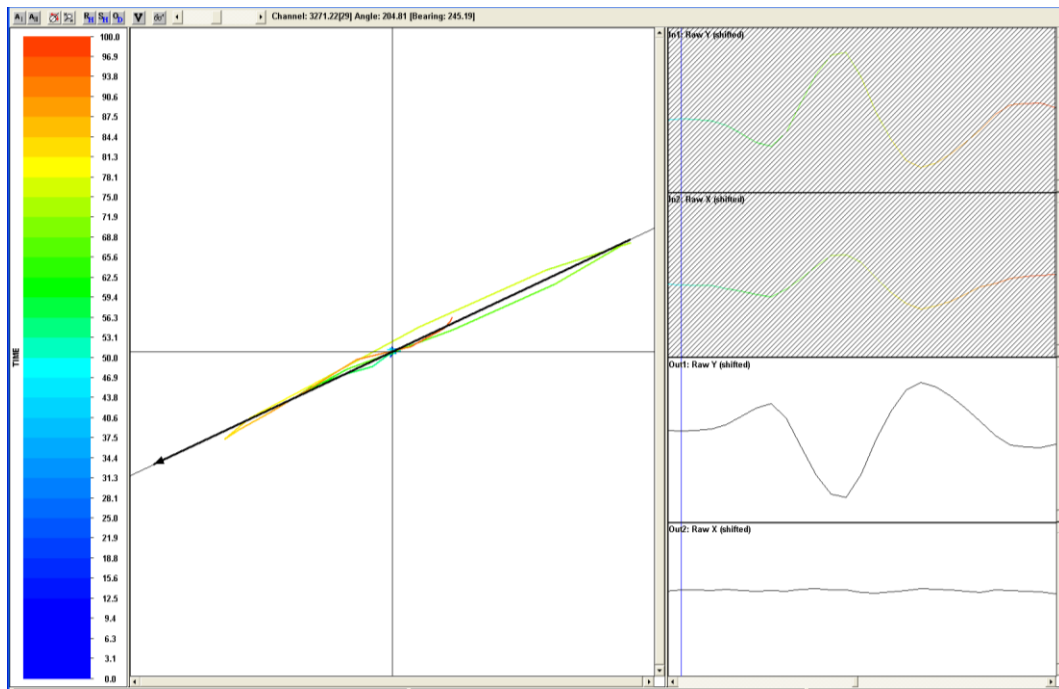


Figure 3.13: Hodogram of X, Y components at 3271.22 m depth.

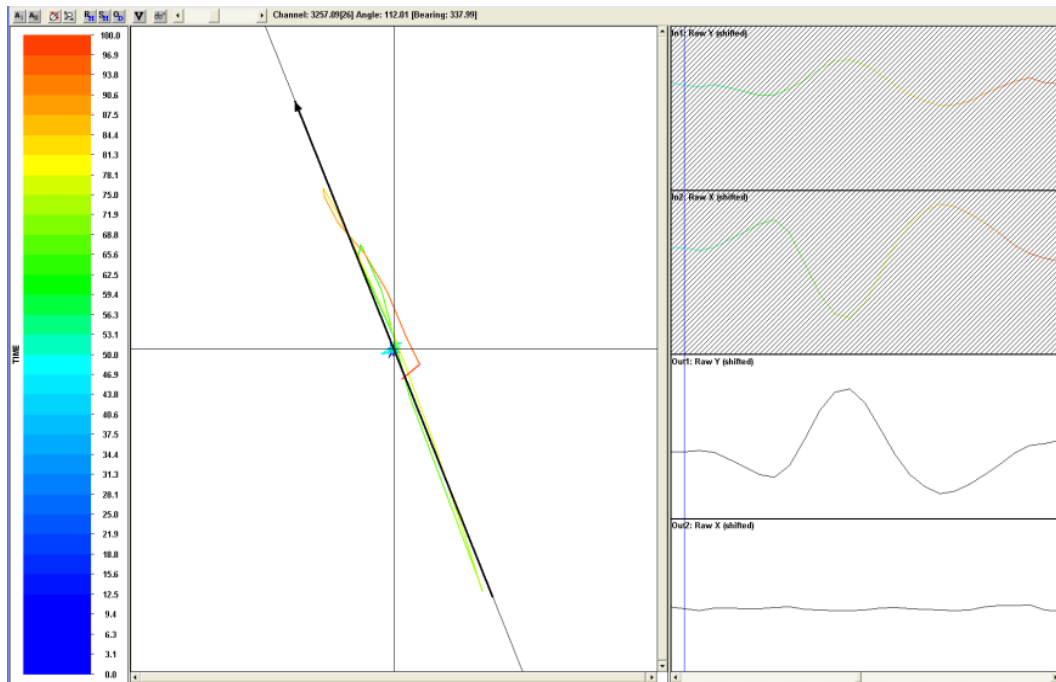


Figure 3.14: Hodogram of X, Y components at 3257.09 m depth.

The cross-hatched vertical boxes bound the amplitudes of the first arrival of the X and Y traces, as is demonstrated in the top two trace panels. Those amplitudes are plotted on the X and Y axes of the hodogram. The linear least-squares fit line determines the computed angle of orientation. The angle is applied to the data, shown on the bottom two trace panels, through a rotation matrix. Note the hodogram is almost a straight line. This is a good quality control of the noise and coupling of the geophones. On the far right panel are the computed slope angles for all levels of a single shot. The slope angles show a randomness. This is the result of the tools being cabled and un-oriented in X and Y with respect to one another in the borehole. The rotation angles and the bearing for each depth level for all the shots is demonstrated in Appendix A.

The data shown in figures 3.15 and 3.16 show H_{\max} and H_{\min} components after the first rotation. In the H_{\max} rotation window, the dominance of the P and SV wavefield is clear. The P waves arrive first with strong amplitude, thus the SV waves arrive approximately 180 ms later and their amplitudes are much smaller. No SH-wave energy is observed. In contrast, in the H_{\min} rotation window, the SH wavefield and the out-of-plane reflections appear to be very strong.

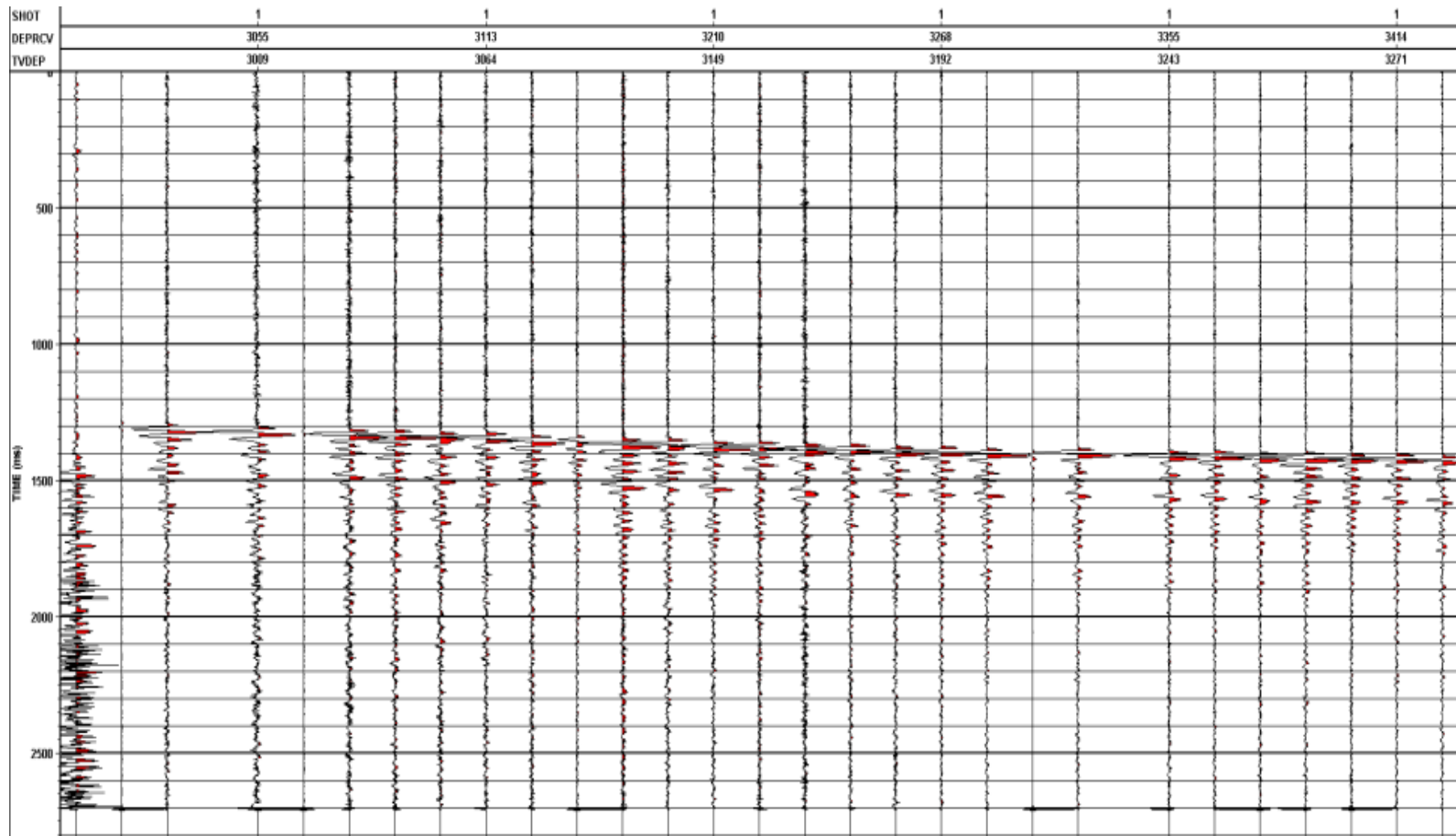


Figure 3.15: H_{\max} Horizontal Rotation.

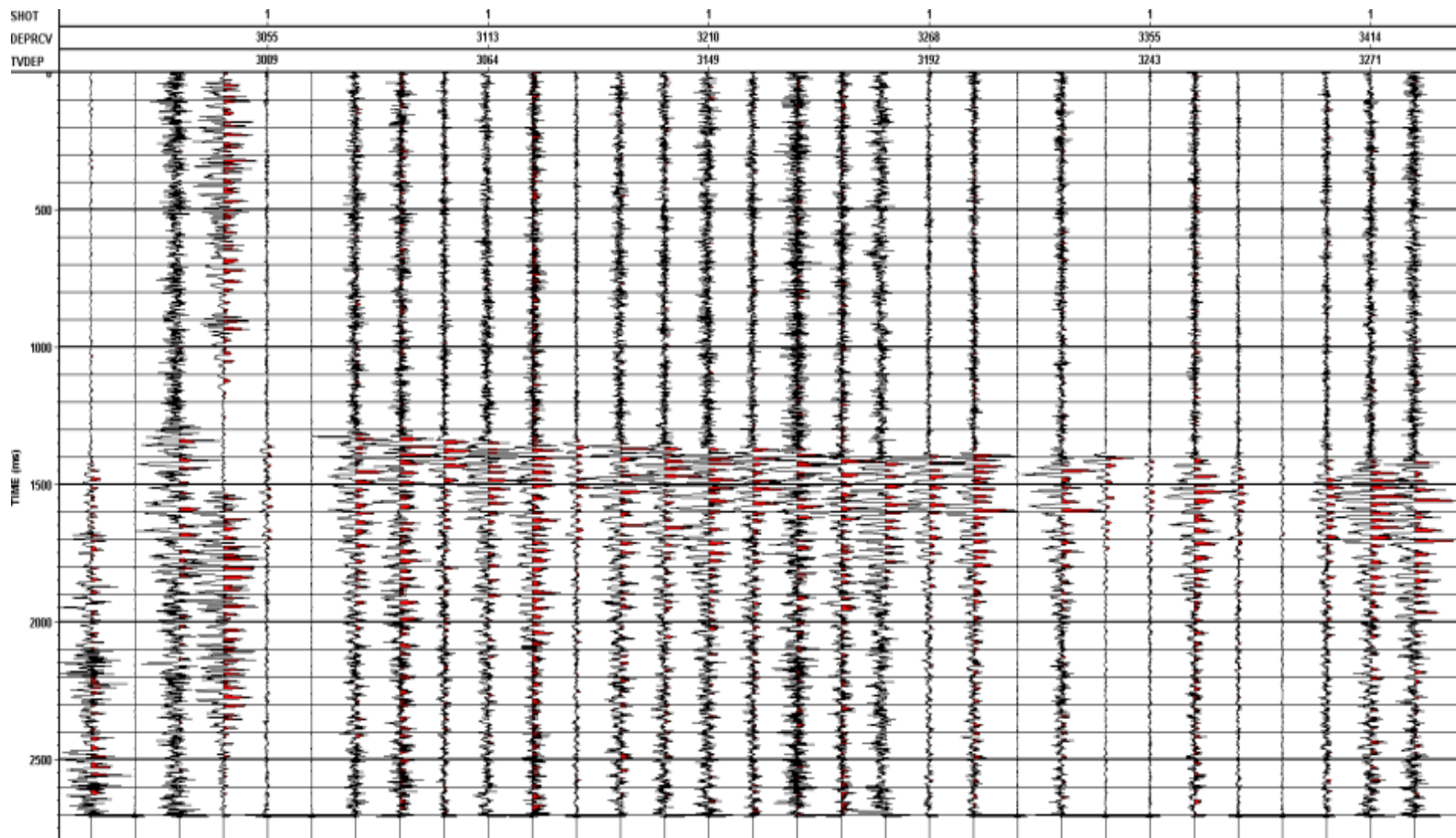


Figure 3.16: H_{\min} Horizontal Rotation.

The second Hodogram Rotation, using downgoing P waves, takes a time window around the P-wave first-break curve on the oriented horizontal (H_{max}) and the Raw Z (vertical component) and orients them in the plane of the well and source. This maximizes the downgoing P-wave energy onto one output channel H_{max}' and the downgoing SV on the other output channel Z'. The polarization method has been performed on the downgoing first-break energy. The upgoing P and SV wavefields are not yet polarized. In order to accomplish this, the time-variant orientation method is used. The method will be discussed in a later section. The predominantly upgoing P and SV wavefields still exist, mixed on both channels. Hodogram examples at three different depths are illustrated in figures 3.17, 3.18 and 3.19. In figure 3.17, a polarity reversal has been observed at the shallowest depth, while the Hodograms at greater depth show similar polarities. This reversal polarity might be caused not only by the relative position of source and receiver, but also from the strong influence of the geological stratification. The produced Hodograms for each depth and the table with the calculated rotation angles are presented in Appendix B.

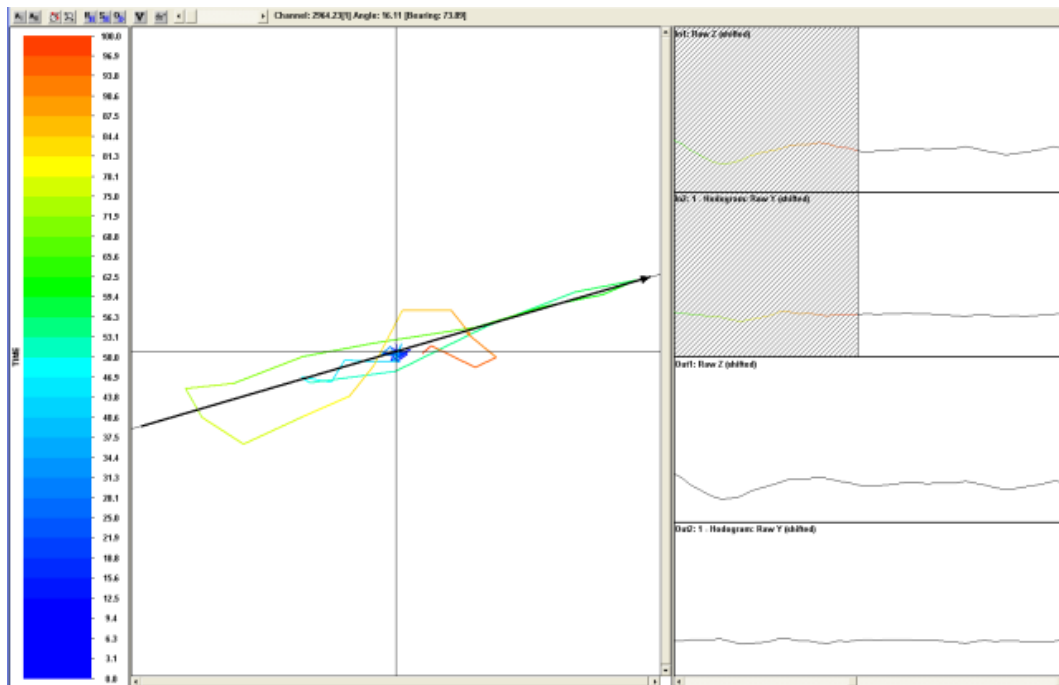


Figure 3.17: Hodogram of H_{max} and Z components at 2964.23 m depth.

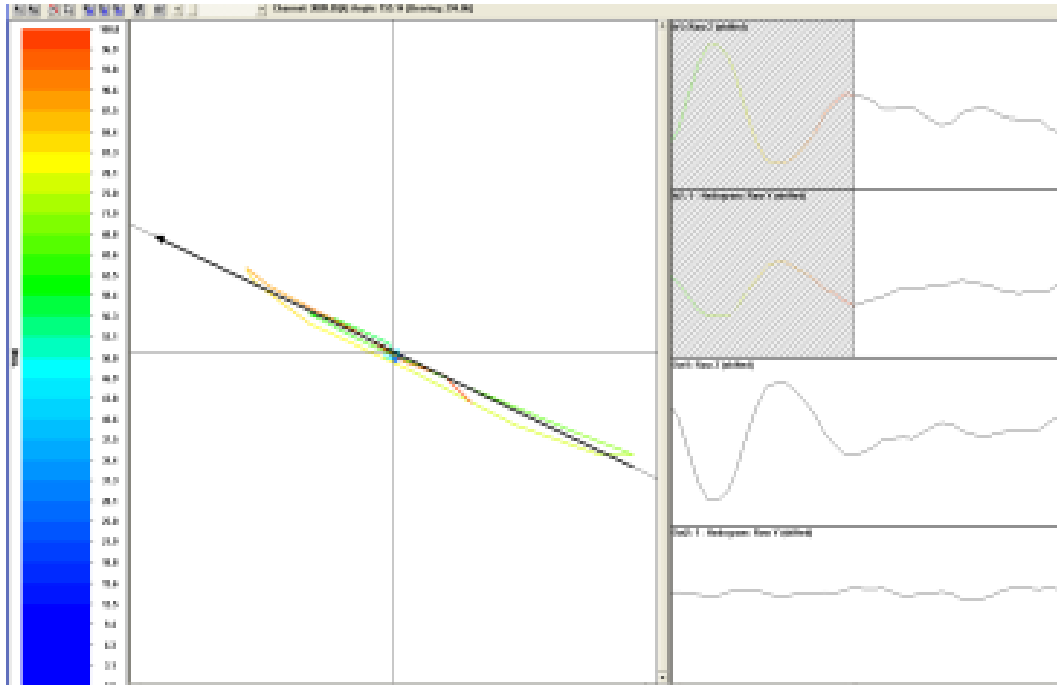


Figure 3.18: Hodogram of H_{\max} and Z components at 3009.05 m depth.

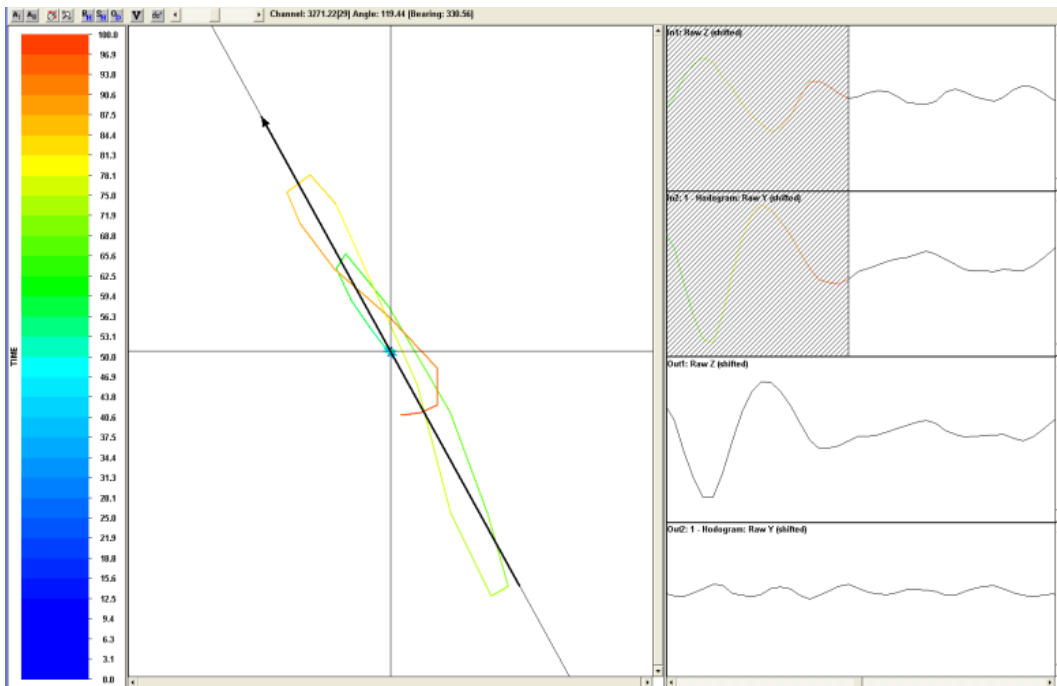


Figure 3.19: Hodogram of H_{\max} and Z components at 3271.22m depth.

The outputs H_{\max}' and Z' of the second Hodogram Rotation are presented in figures 3.20 and 3.21.

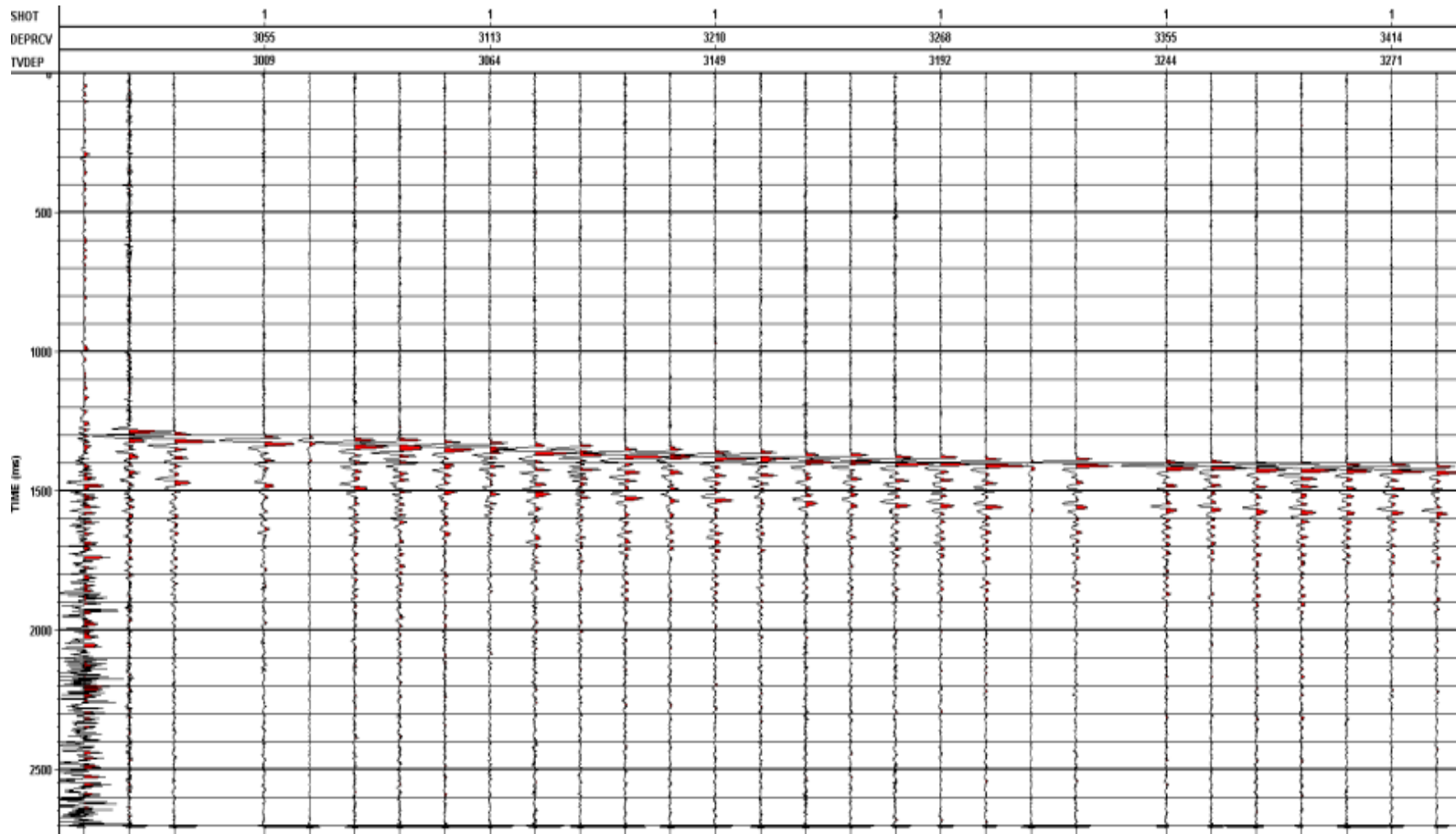


Figure 3.20: H_{\max}' Hodogram Rotation.

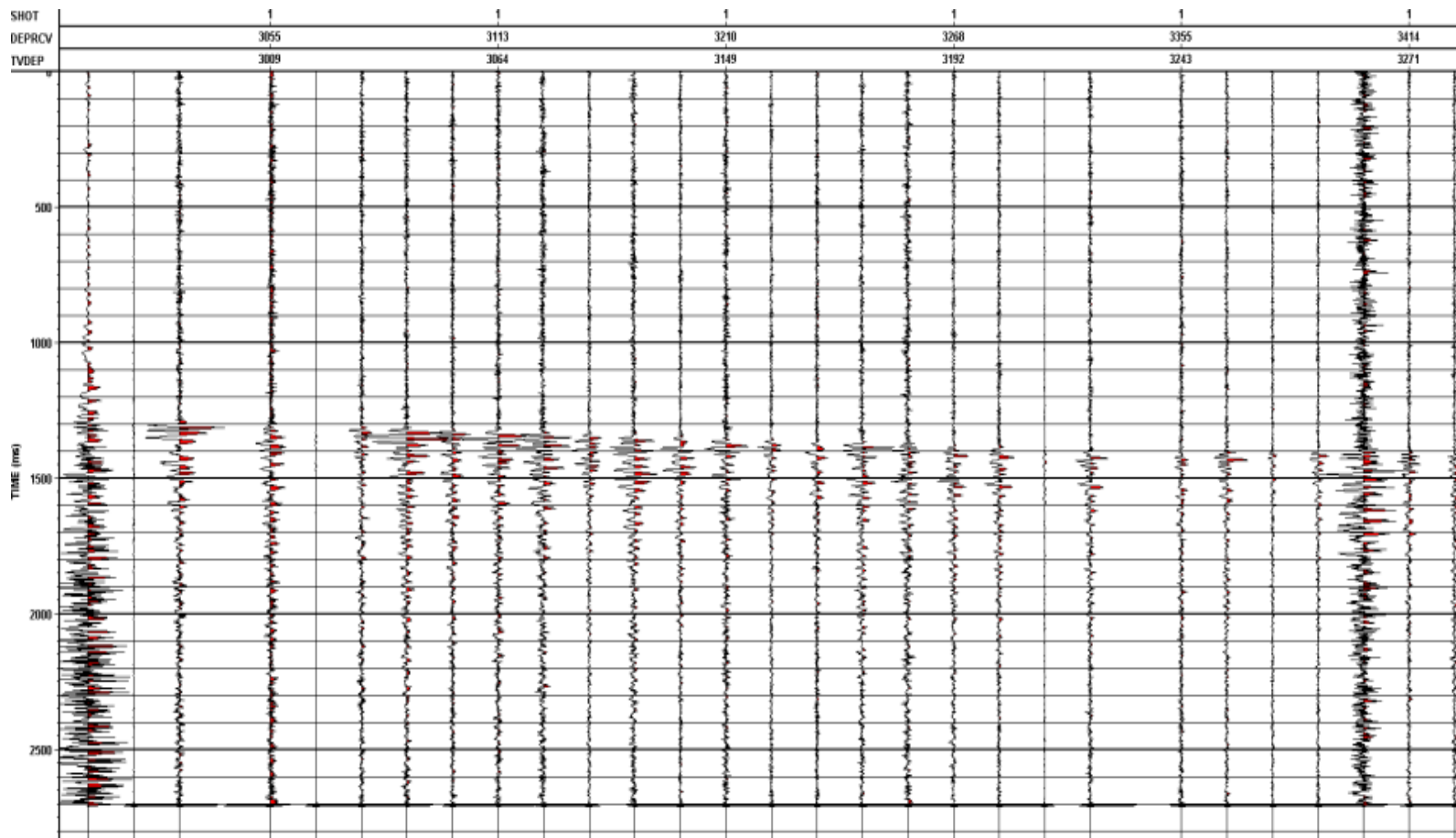


Figure 3.21: Z' Hodogram Rotation.

3.6 Wavefield Separation

Effectiveness of wavefield separation is related to repeatability of the source and regularity of acquisition. Median filters usually are robust and successfully used for the separation of upgoing and downgoing VSP waves. Another approach is using velocity filters like an $f-k$. This approach requires data adequately sampled in space to avoid aliasing (Poletto et al,2004).

3.6.1 Wavefield separation using velocity filters

Standard procedures for velocity filtering of VSP data usually use filters implemented in the $f-k$ space. The $f-k$ filters are applied to the entire dataset. Separating waves by velocity pass and reject filters is based on the following dichotomy: waves that are desired are signal and everything else is noise. So signal is passed by time-correcting it for moveout and applying velocity pass filters that are centered about zero moveout. The coherent noise is rejected by time-correcting it for moveout and applying velocity reject filters that are centered about zero moveout. This principle is used to pass signal (upgoing P-waves) and reject noise (downgoing P waves and tube waves) (Al-Fares et al 1987).

Downgoing waves are characterized by apparent velocities that are positive (Mari and Coppens,1991). Downgoing P-waves are separated from upgoing waves by correcting the data for downgoing P wave moveout, and applying an $f-k$ filter with pass band $\pm V_d$, where V_d is an aparent-velocity parameter designed for optimal suppression of upgoing waves, to get the purest downgoing P-waves. This set will include the direct P-wave and all downward-traveling multiples.

Processing to separate upgoing P-waves from downgoing waves is achieved by correcting for upgoing P-wave moveout, and applying an $f-k$ filter whose pass band is between $\pm V_u$, where the cutoff velocity V_u is designed for optimal suppression of the downgoing waves. After applying the $f-k$ filter, the moveout corrections may be restored, and then the upgoing P-waves will be in their true positions, or they can be

corrected to surface time to line them up with zero moveout. The upgoing P-waves include the primary reflections and all upward traveling multiples.

3.6.2 Wavefield separation using median filter

Median filters are very effective and easy to implement. One useful characteristic of median filtering is its ability to preserve signal edges while filtering out impulses. They do not require any Fourier transformation since they operate entirely in the time domain and they can be applied to irregularly sampled data containing signal with nonlinear moveout. Before applying them, the energy mode that is to be preserved has to be time corrected to zero moveout. Median filters have been used as time-domain low-pass filters for smoothing sequences. The implementation of the filter requires a simple digital nonlinear operation. For a signal length L , a window of length $2N+1$ slides across this signal. The filtered output is the median of these $2N+1$ signal samples, and is associated with the time sample at the center of the window (Gallagher and Wise, 1981).

3.6.3 Separate Downgoing P from H_{\max}

In the following text, the terms FRT, +TT time and -TT time will be used repeatedly. When the data are recorded in the field without any bulk shift being added or subtracted from the raw recorded times, the term FRT (field recorded time) is used to describe the time placement of the data. To align the data along the first-break picks, the first-break traveltime for each trace is subtracted from that trace and the aligned data is bulk-shifted to a time datum (to 1200 ms in this project). The data in that configuration is said to be in -TT time. The TT refers to the first-break traveltime for that trace. To align the upgoing waves horizontally (imaging flat interfaces), each trace's respective first-break time is added to that trace. The data in this time configuration is said to be in +TT time.

In order to separate the downgoing P waves, the downgoing waves are aligned horizontally and enhanced by median and $f-k$ filtering. These filters require proper

‘flattening’ of the wave that is to be selected. Flattening is a travel-time correction. After this correction, the wave is in normal incidence.

The downgoing P-wave separation from the H_{\max} wavefield is accomplished with the flows shown in figures 3.22 and 3.23. A fifteen-trace median filter is applied to compute the downgoing wavefield. Also, a mean scaling was applied to all the traces in order to cover the direct arrival only. The FRT and $-TT$ outputs of those two flows are presented in figures 3.24, 3.25, 3.26 and 3.27.

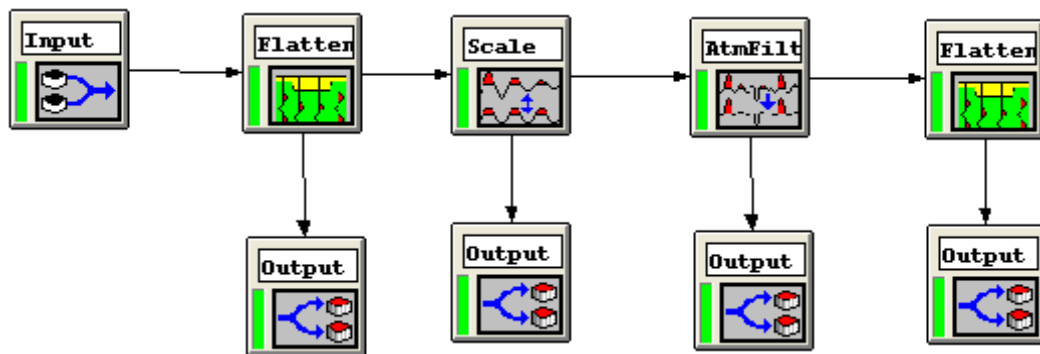


Figure 3.22: Downgoing P Separation using a median filter.

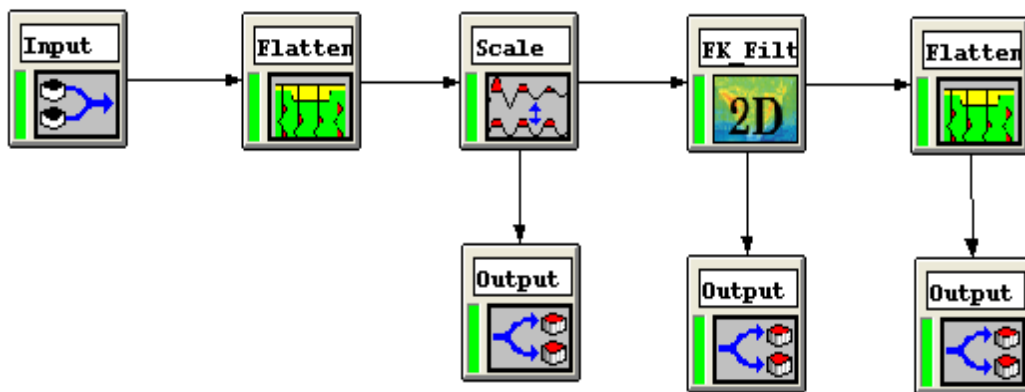


Figure 3.23: Downgoing P Separation using an $f-k$ filter.

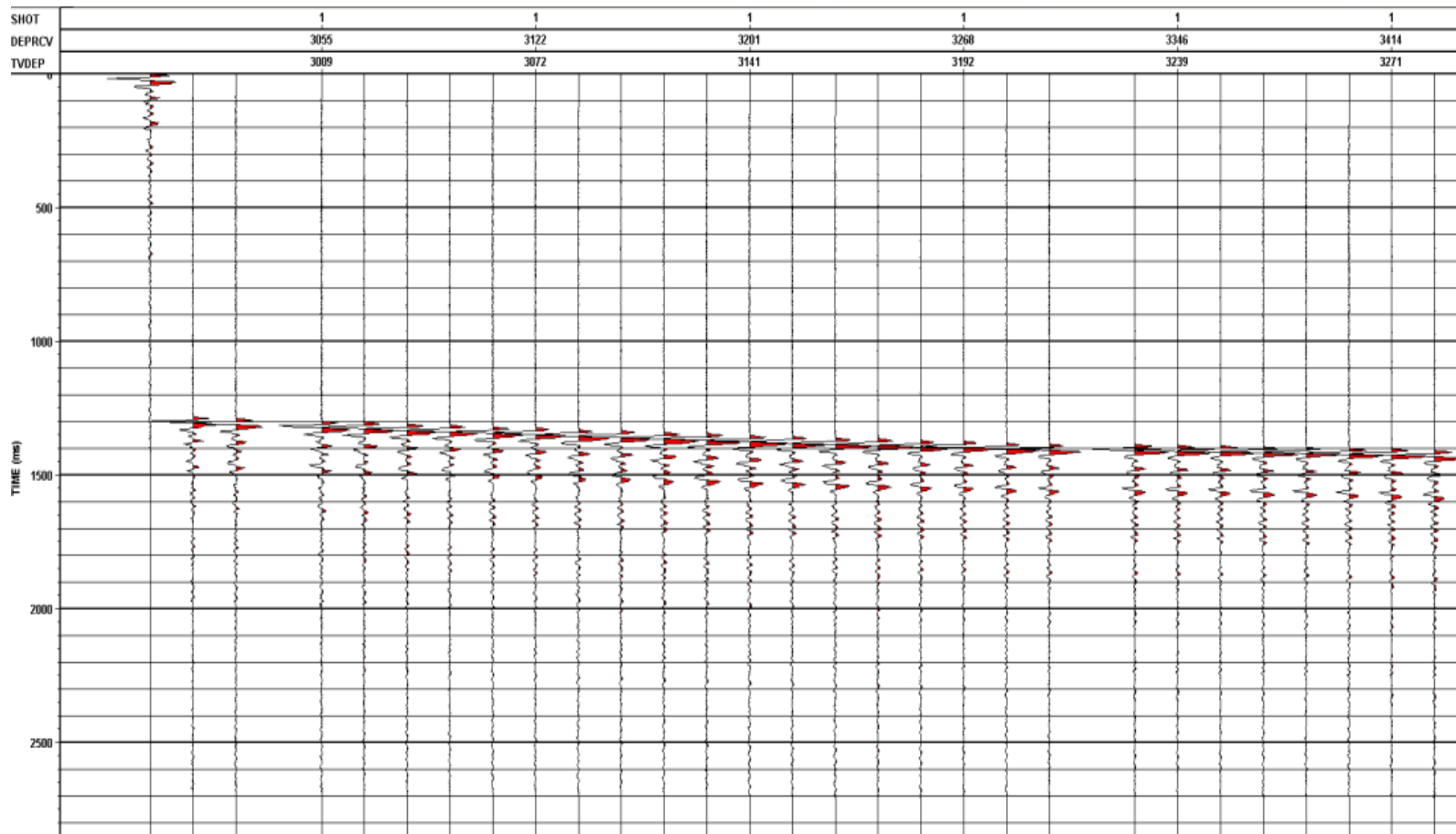


Figure 3.24: FRT Output for Downgoing P Separation using a median filter.

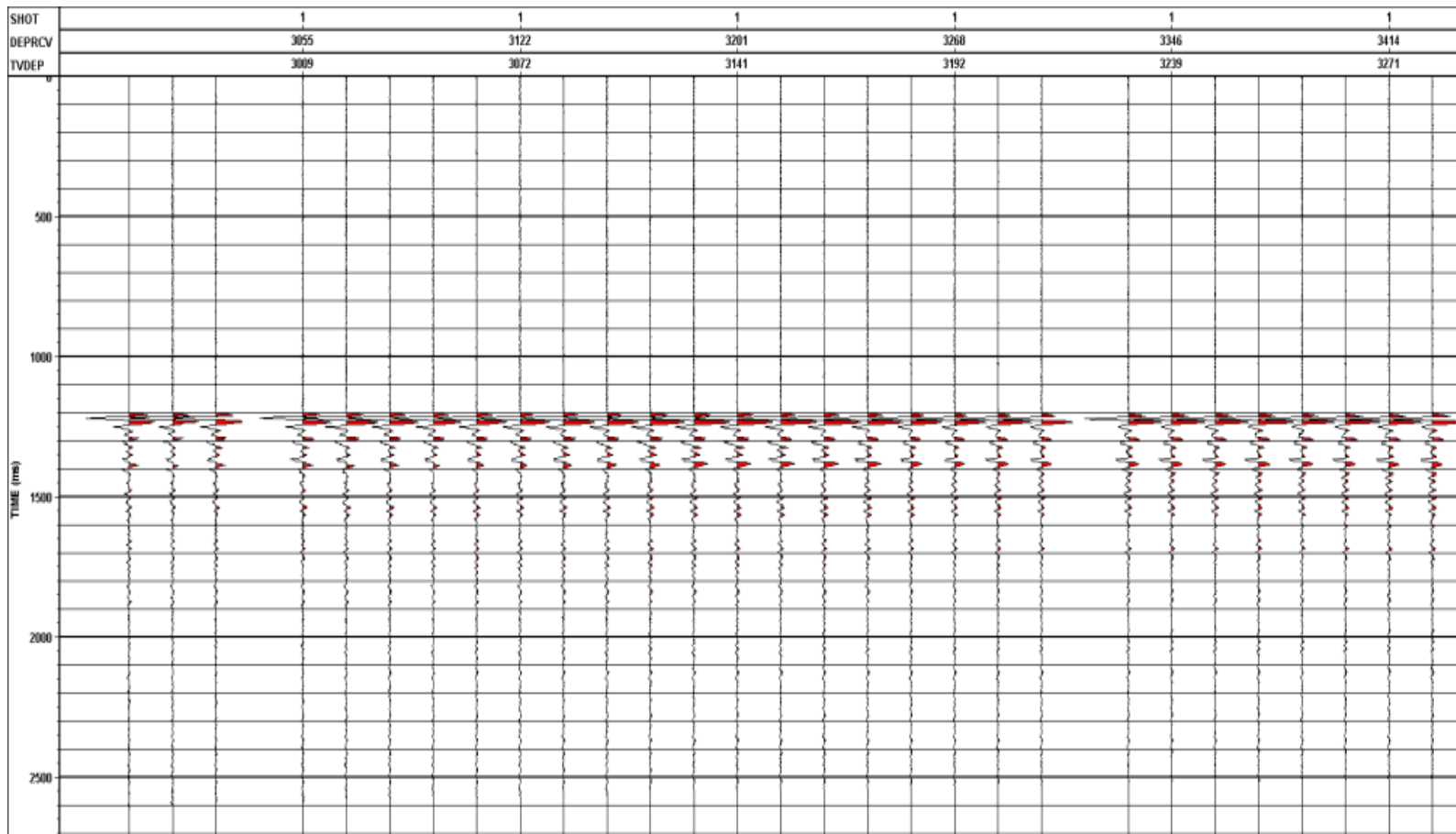


Figure 3.25: -TT Output for Downgoing P Separation using a median filter.

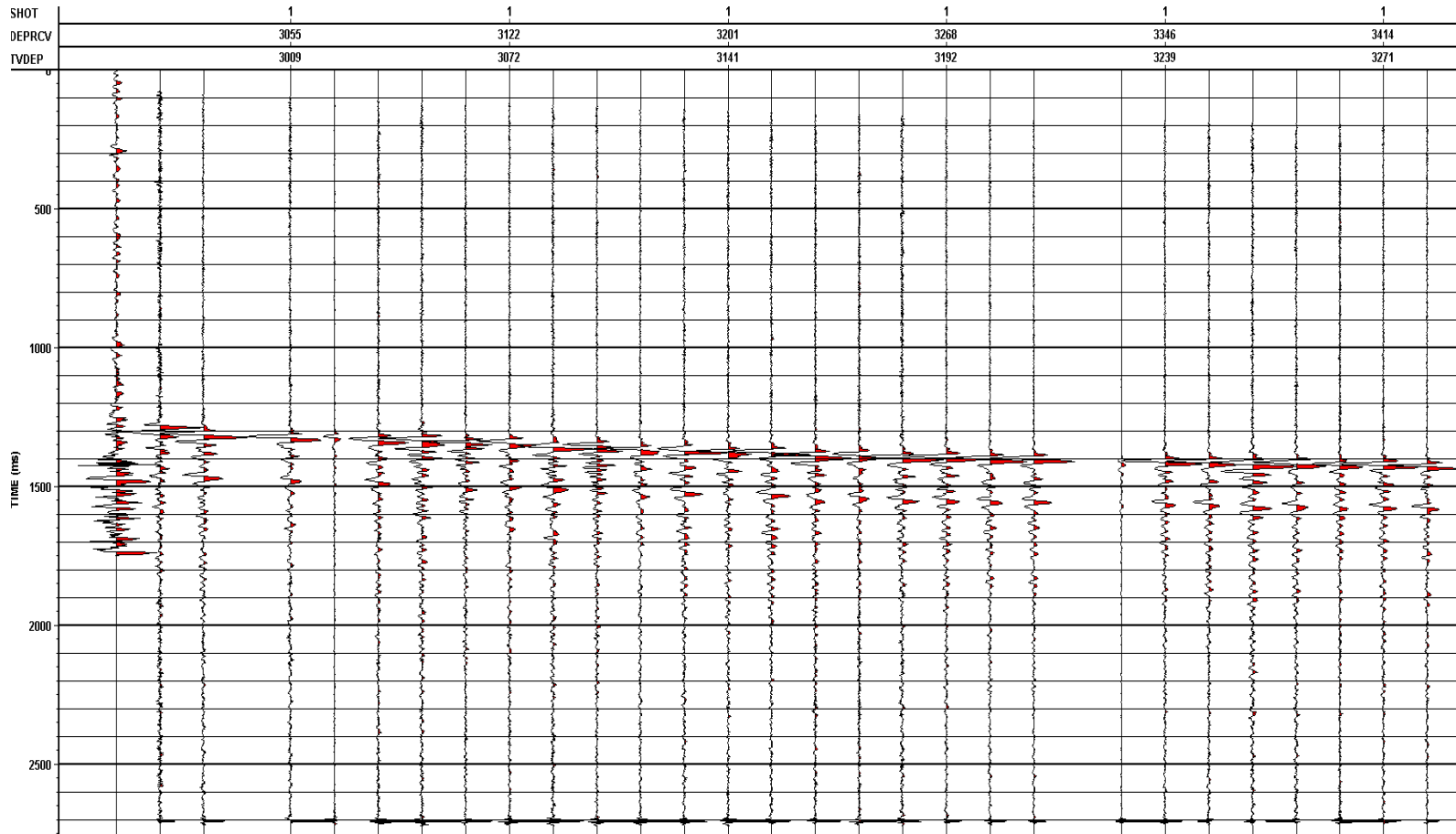


Figure 3.26: FRT Output for Downgoing P Separation using an $f-k$ filter.

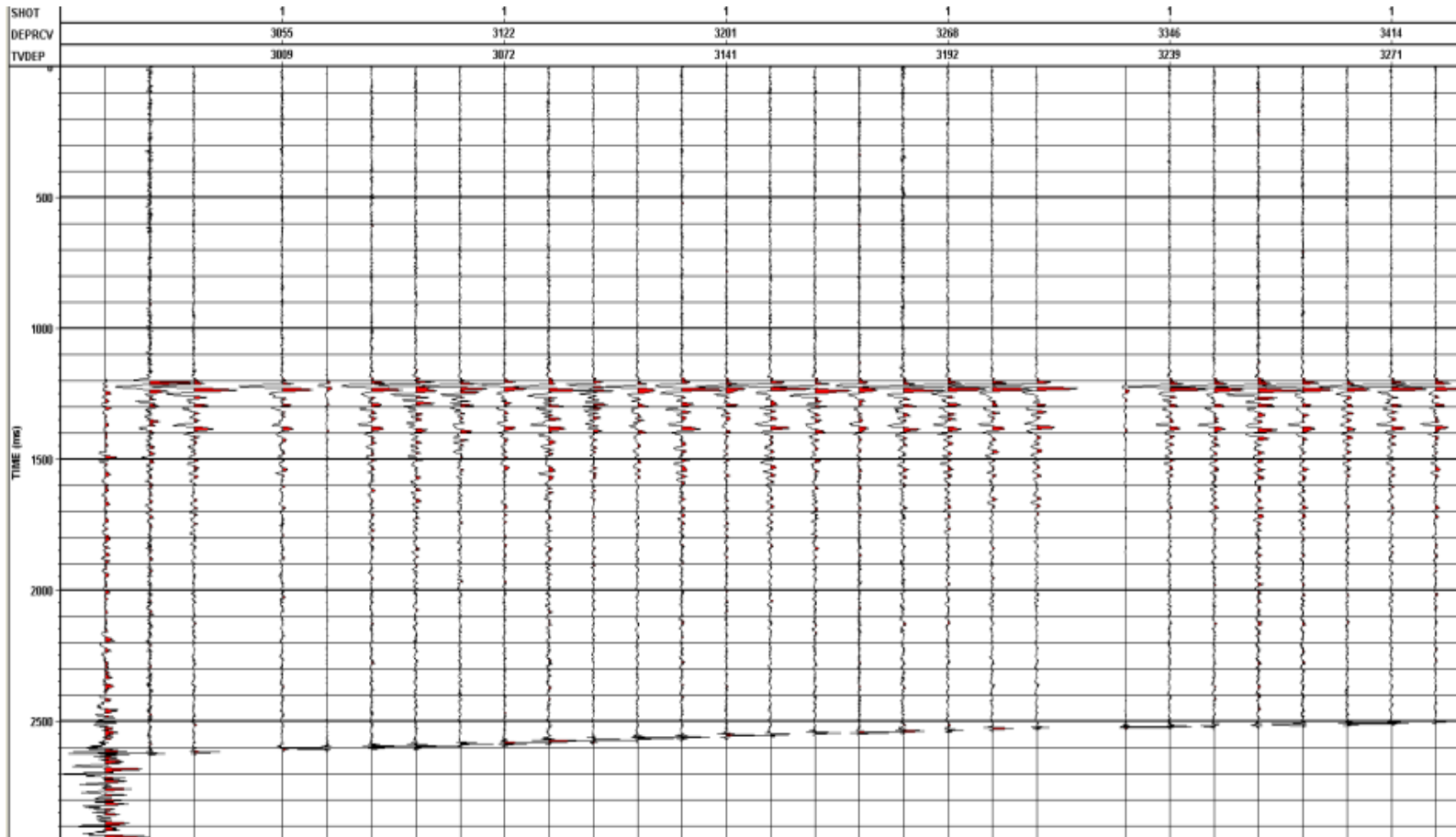


Figure 3.27: -TT Output for Downgoing P Separation using an $f-k$ filter.

3.6.4 Separate Upgoing P from Raw Z and H_{\max}

The separation of the upgoing P waves from the Raw Z and H_{\max} wavefields has been accomplished using an $f-k$ filter. Initially, the downgoing wavefield (P and SV) was separated from the Z and H_{\max} wavefields. Thereafter, it was subtracted from the original data yielding the upgoing wavefield. The upgoing energy in Raw Z and H_{\max} contains both P and SV waves.

The flow shown in figure 3.28, has been used for these purpose. The input is Raw Z or H_{\max} depending on which wavefield the separation takes place in. The FRT and – TT outputs are presented in figures 3.29, 3.30, 3.31 and 3.32.

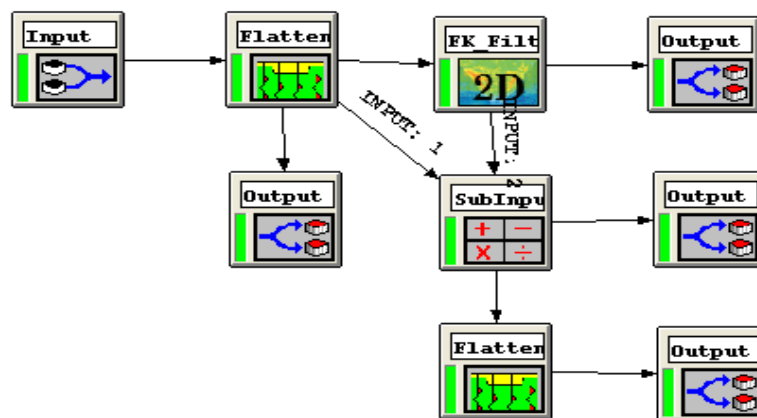


Figure 3.28: Upgoing P Separation from Raw Z and H_{\max} using an $f-k$ filter.

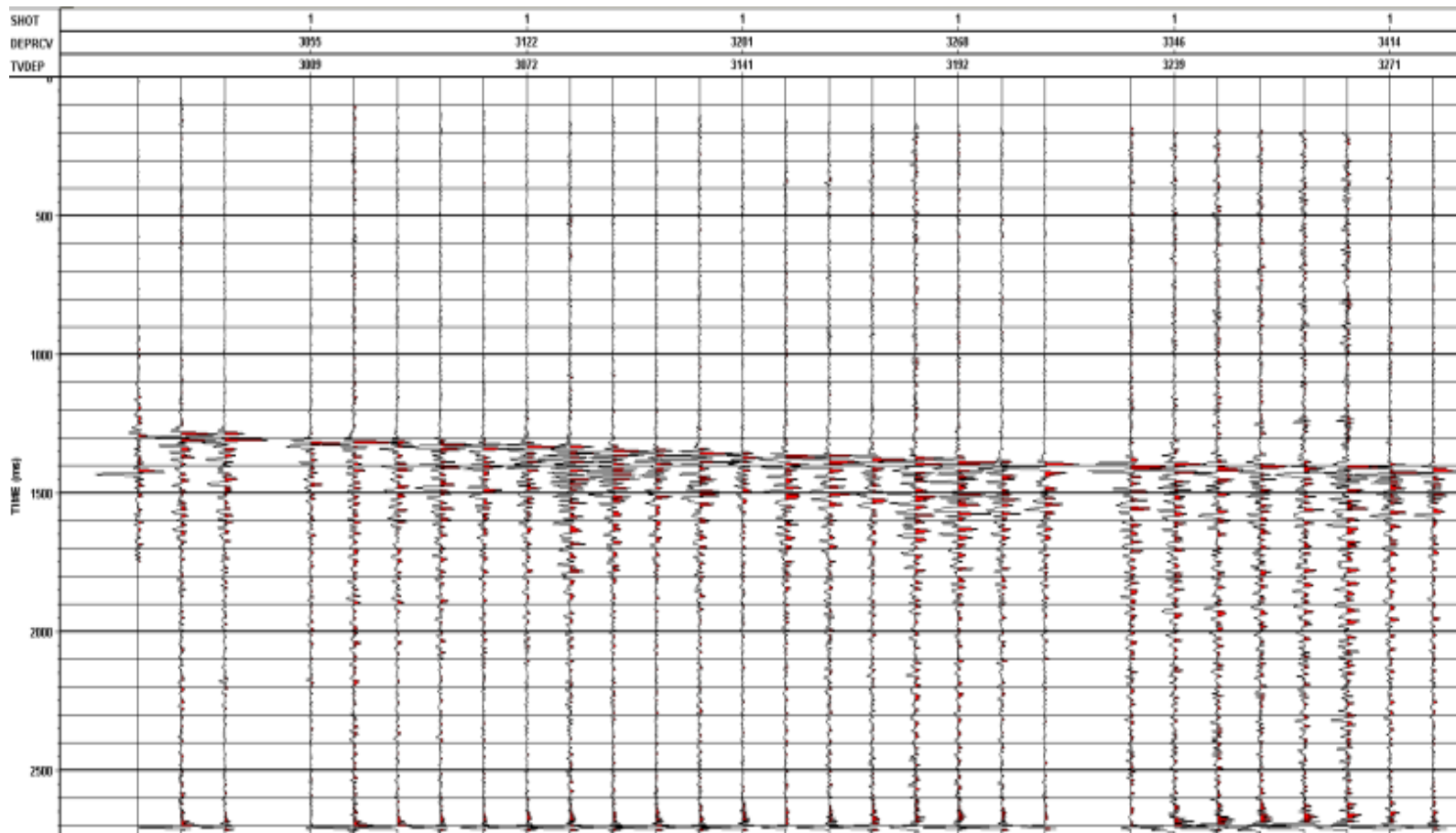


Figure 3.29: FRT Output of Upgoing P Separation from Raw Z.

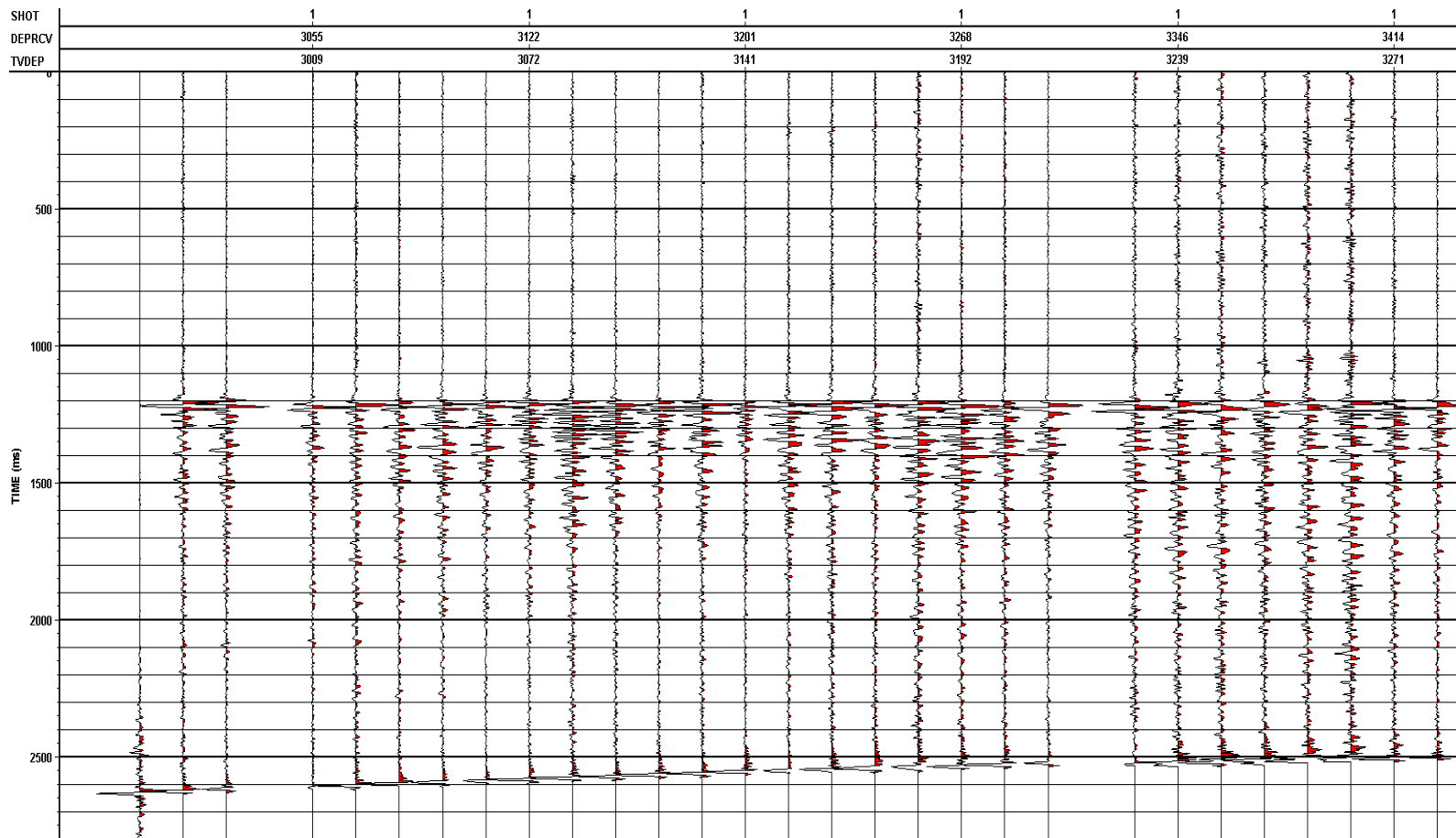


Figure 3.30: -TT Output of Upgoing P Separation from Raw Z.

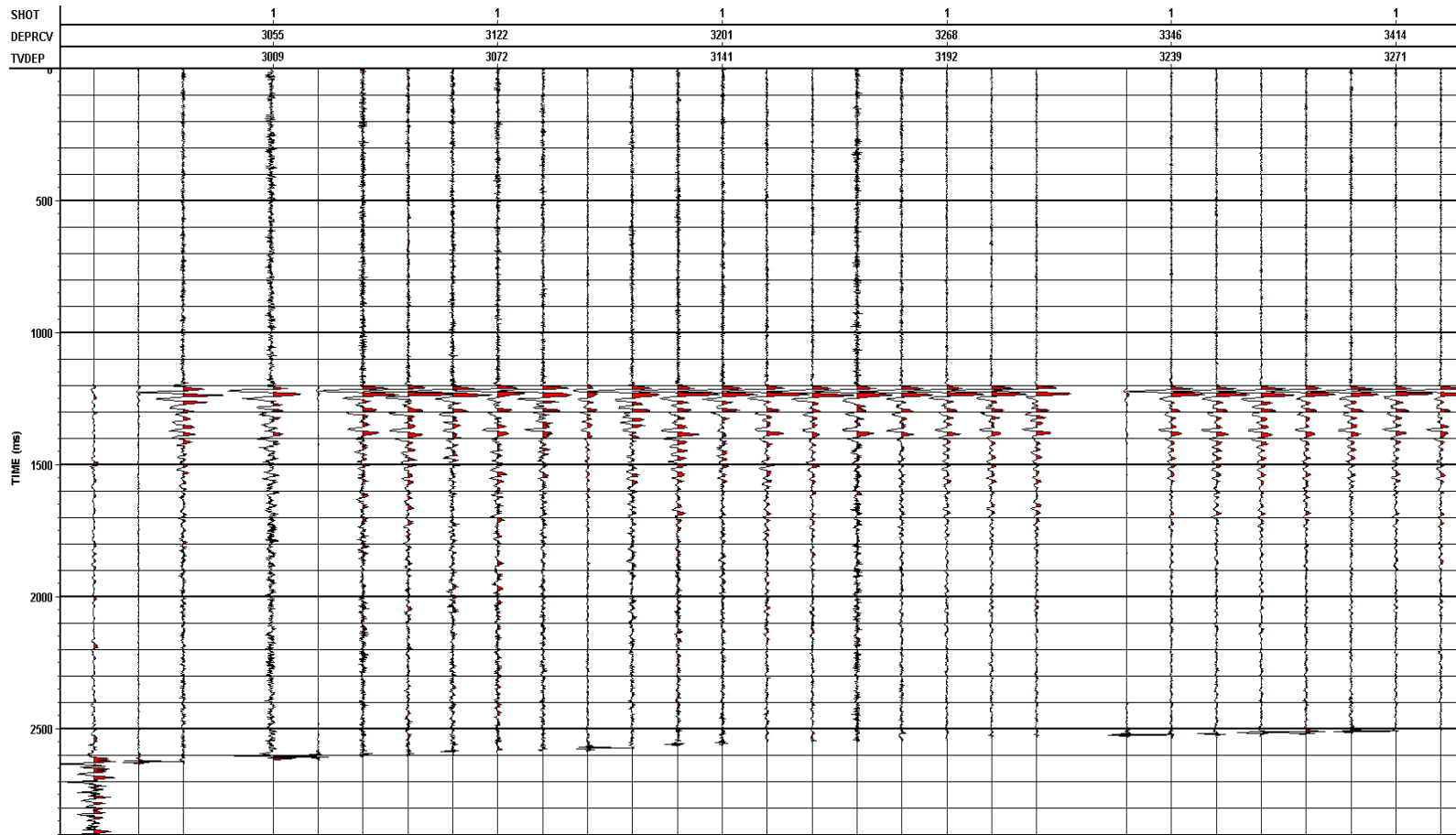


Figure 3.31: FRT Output of Upgoing P Separation from H_{\max} .

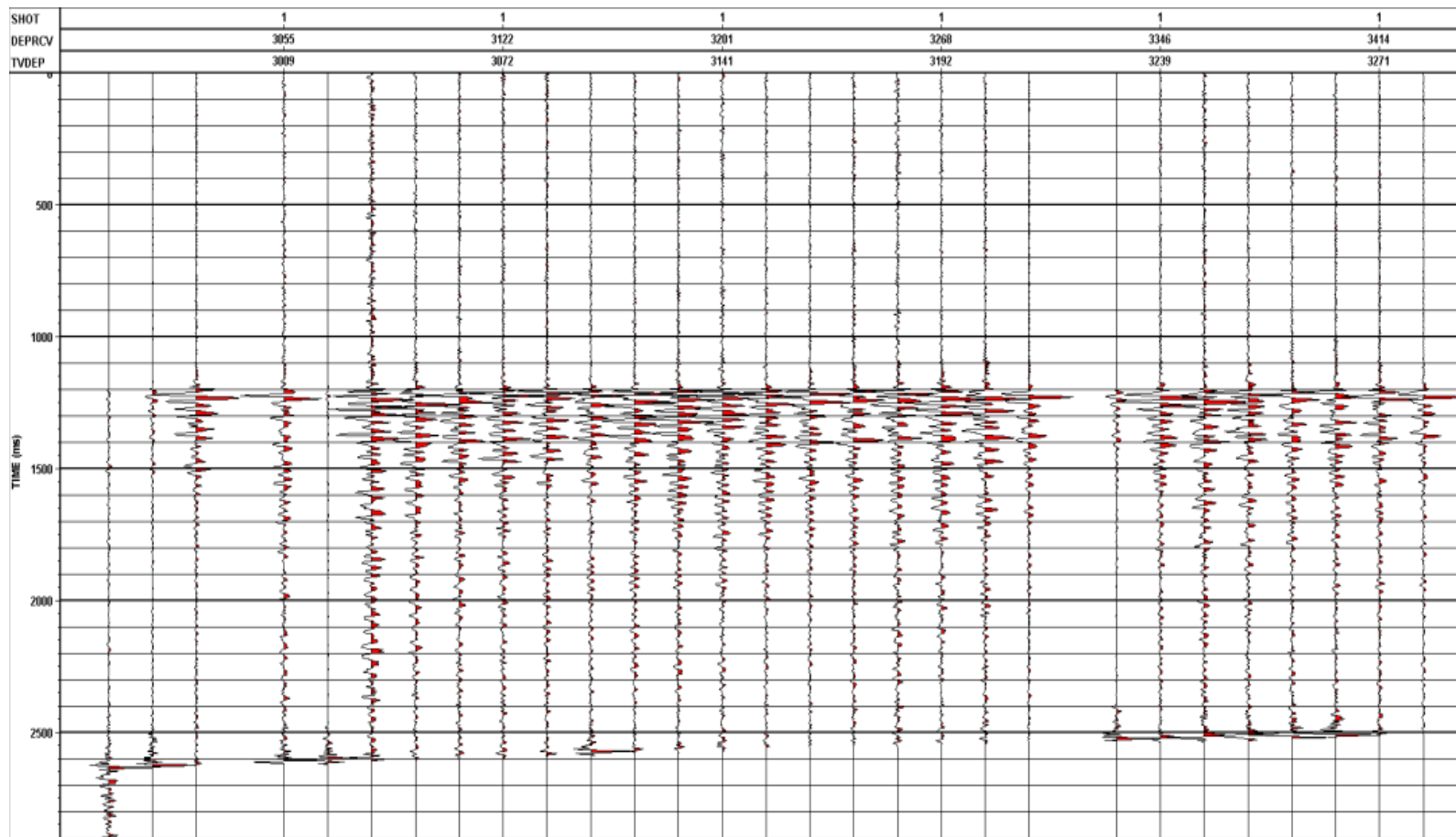


Figure 3.32: -TT Output of Upgoing P Separation from H_{\max} .

3.7 Time Variant Orientation

On the upgoing Z' and H_{\max}' panels, the remaining upgoing wavefields are not yet polarized and need to be rotated onto separate components in a time-variant manner to capture all the energy for each upgoing wavefield (P or SV). This can be accomplished using a velocity model and calculating the angle of incidence of P and SV waves at all time points on the VSP data (Kuzmiski et al, 2009).

In figure 3.33, the processing flow used for the separation of the P and SV components in the upgoing wavefield components is illustrated.

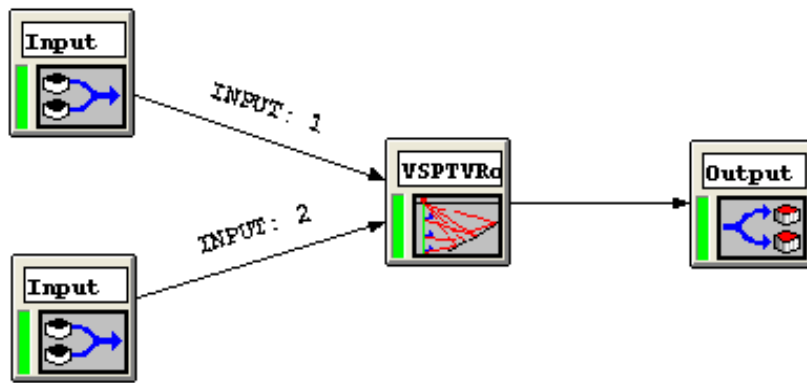


Figure 3.33: Separation of Upgoing P and SV.

The input 1 is the H_{\max} upgoing FRT file and the input 2 is the Z upgoing FRT file. In order to create the Ray Trace file, the velocity model that was constructed in the previous section, derived by the first-break times, was used as a velocity input. Also, the angles between 270 and 360 degrees and the number of traces equal to 2000 has been selected. This package estimates the angles at which the upgoing P and SV waves emerge into the geophones at the receiver depths with respect to the input two-dimensional velocity model. The H_{\max} upgoing FRT and Z upgoing FRT panels are rotated according to the incoming angles of the upgoing P wavefield.

The output file has the name TV-OR. This includes the two separate components P and SV. In figures 3.34 and 3.35, the upgoing P and upgoing SV wavefields are presented.

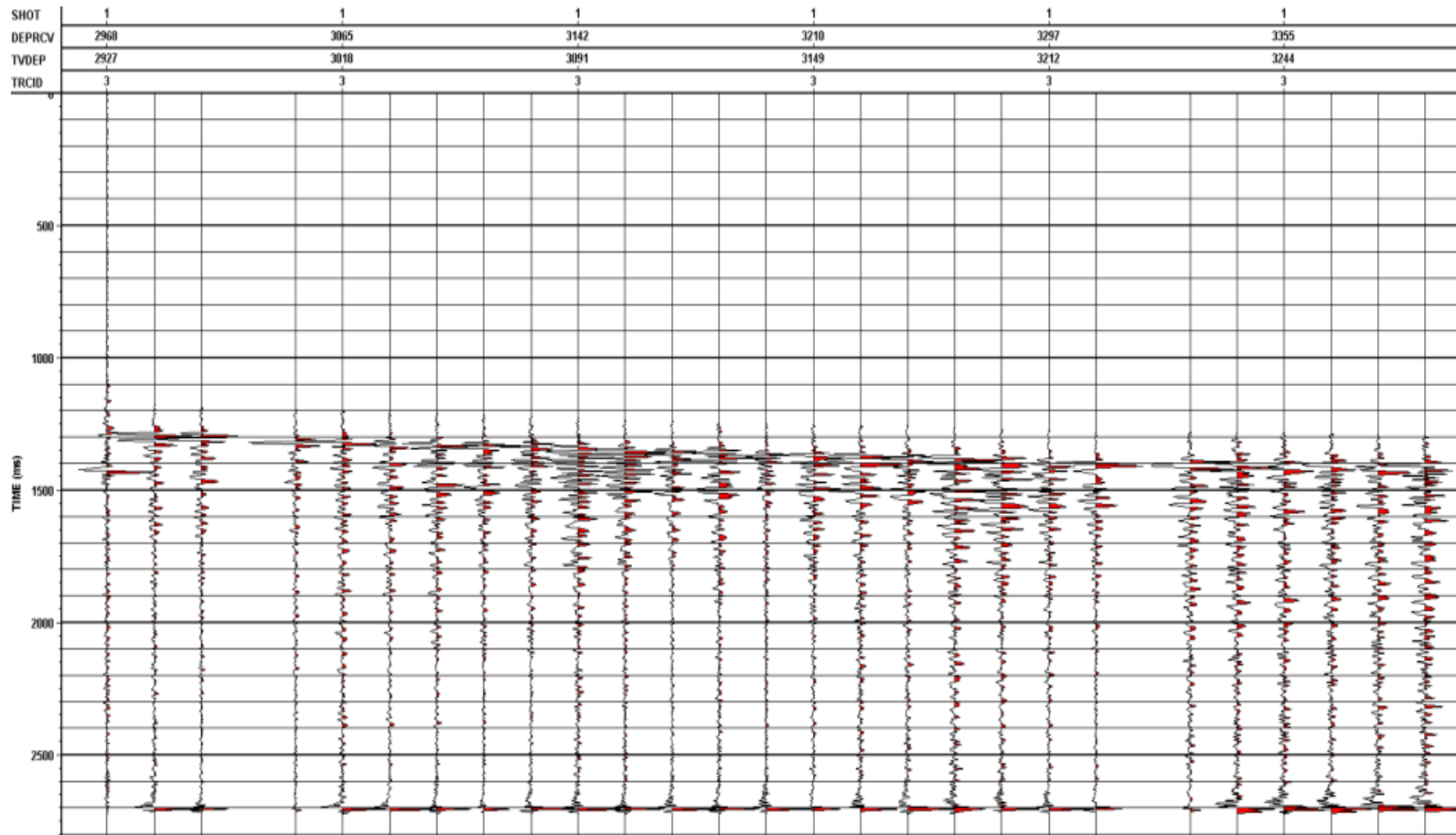


Figure 3.34: Upgoing SV Wavefield.

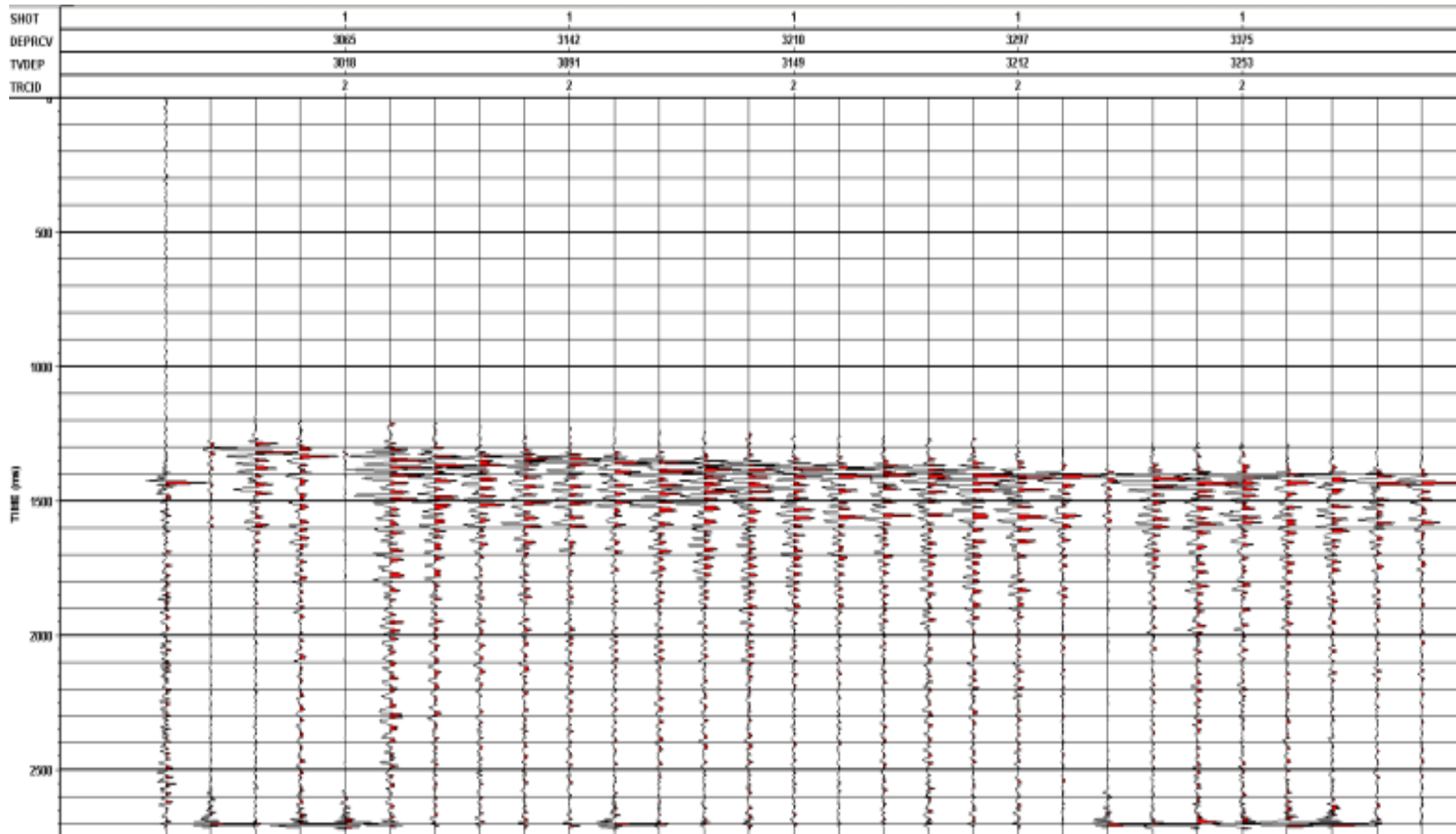


Figure 3.35: Upgoing P Wavefield.

3.8 Deconvolution

The downgoing P wavefield was used to design an operator to deconvolve the VSP upgoing wavefield. Generally, this works well for near-offset VSPs but as the offset increases, the ray paths of the downgoing and upgoing wavefields are no longer coincident and the criteria for using the downgoing as the deconvolution operator breaks down. This usually occurs on the medium to long offsets. In this case, the downgoing and upgoing wavefields must first be separated and then predictive deconvolution can be used to aid in removing longer-period multiples. This is followed by spiking deconvolution to whiten and convert the data to zero phase (Kuzmiski et al, 2009). In the current project, the VSP deconvolution does not fail showing that the wavefields are still coincident.

The model for VSP deconvolution assumes the downgoing waves reflect off acoustic impedance contrasts at near-vertical incidence in the earth to generate the upgoing waves. In other words, the downgoing wavefield, D_{zi} , which consists of the source signature and multiples generated above the geophone, is convolved with the reflection coefficients (RC), of the earth to obtain the upgoing wave field, U_{zi} :

$$U_{zi}=D_{zi}*RC \quad \text{Eq. 3.4}$$

Figure 3.36 shows why the VSP polarity is fixed after deconvolution based on the downgoing signatures. When upgoing and downgoing waves are recorded by the same geophone at each level, a downgoing compressional pulse will produce a trough, while a positive reflection coefficient, which generates an upward compression pulse back to the geophone, will produce a peak (upgoing waves). The borehole geophone responds to the upgoing compressional pulse with the opposite polarity as for a downgoing compressional pulse (DiSiena and Gaiser, 1983). In the filter design, by specifying the desired output to be a zero-phase waveform with a central trough, the deconvolution will always produce a positive reflection coefficient and a zero-phase wavelet with a central peak on the resulting seismograms.

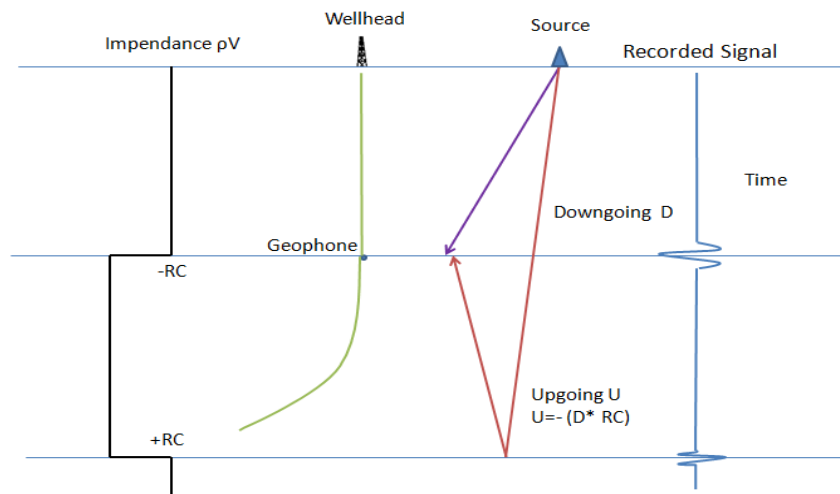


Figure 3.36: VSP Polarity.

The downgoing P wavefield is trace equalized along the first breaks prior to waveshaping deconvolution to insure that the same amplitude operator is applied to each upgoing trace. This process assures that a constant-amplitude deconvolution operator is calculated from the downgoing P wavefield. The designed deconvolution operator is calculated for each depth of the downgoing P wavefield and its length is only limited by the signal-to-noise ratio in the later times of the traces. The flow used for waveshaping deconvolution of downgoing P wavefield is presented in figure 3.37. Both inputs 1 and 2 are the file H_{max} ' Downgoing P -TT. The first-arrivals are aligned at 1200 ms. The waveshaping process eliminates many of the multiples in the data. This can be observed by noting that the reverberations in the downgoing P waves occurring after the first breaks are collapsed into a single peak wavelet after waveshaping deconvolution. The bandwidth of the filter applied to the deconvolved output is 5/10-80/90 Hz. The output file is the downgoing P deconvolution operator.

The processing flow in figure 3.38 shows the waveshaping VSP deconvolution of the upgoing wavefield. The input 1 is the H_{max} ' Downgoing P -TT and the input 2 is the file TV-OR. The optimized parameters from the previous flow have been used to perform the VSP deconvolution on the upgoing wavefield. The output panel from the polarization called Z'' Upgoing P wavefield.

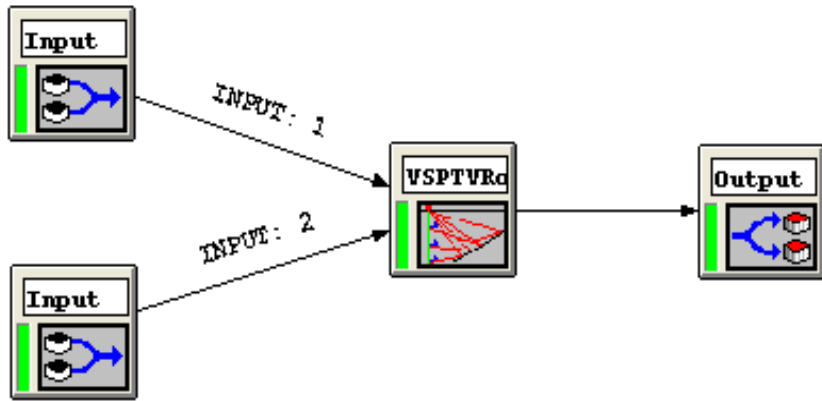


Figure 3.37: Deconvolution downgoing P operator.

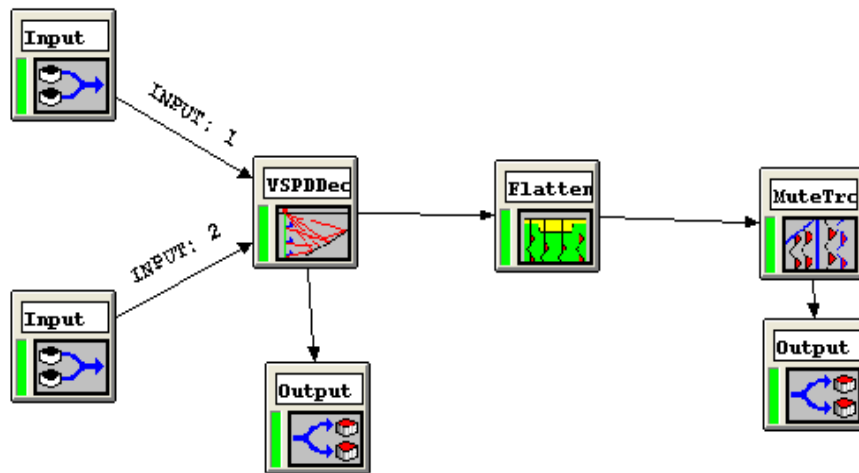


Figure 3.38: VSP waveshaping deconvolution on upgoing wavefield.

The deconvolution downgoing P operator is illustrated in figure 3.39 while the Z'' Upgoing P wavefield is shown in figure 3.40.

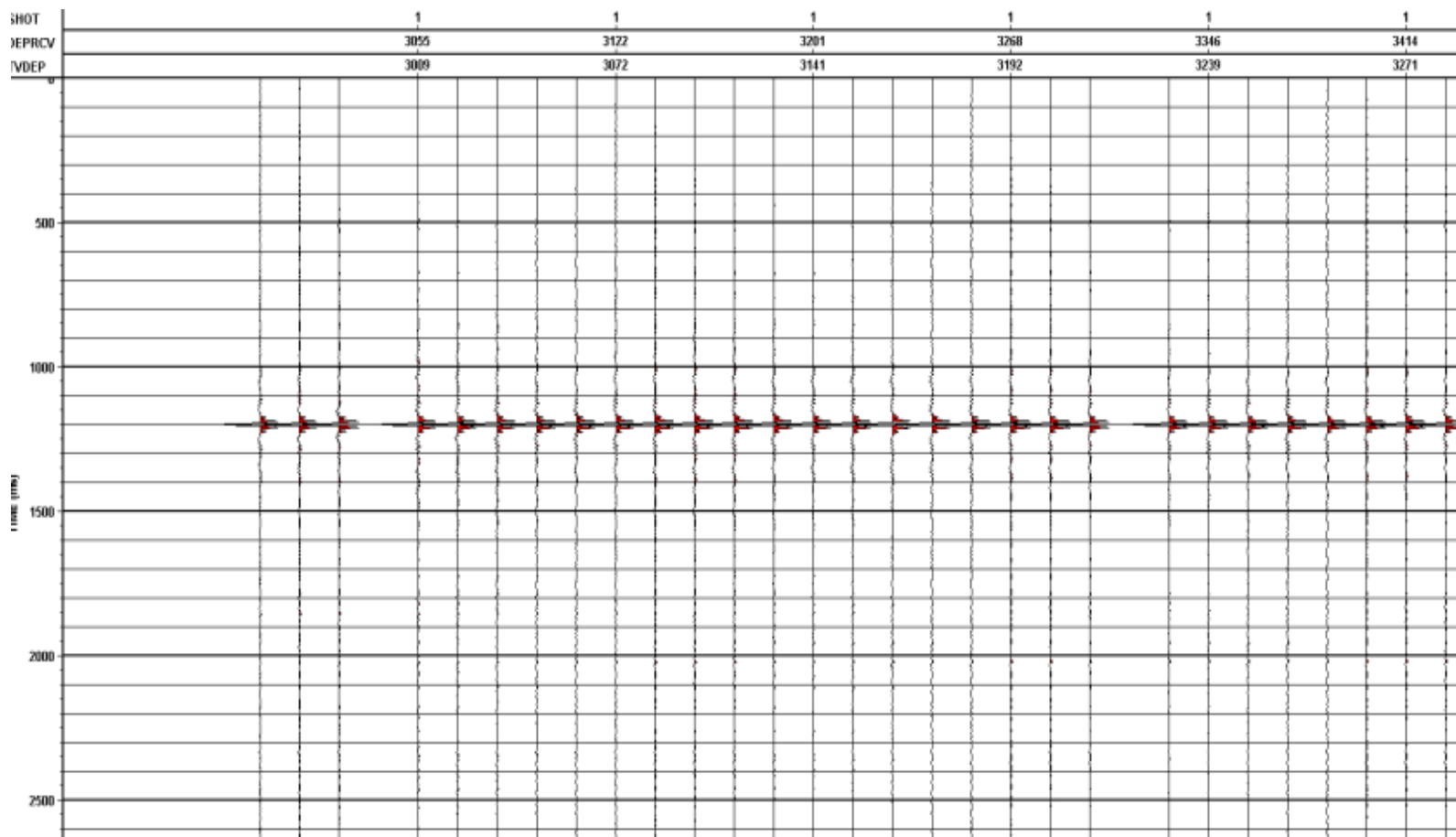


Figure 3.39: Downgoing P deconvolution operator.

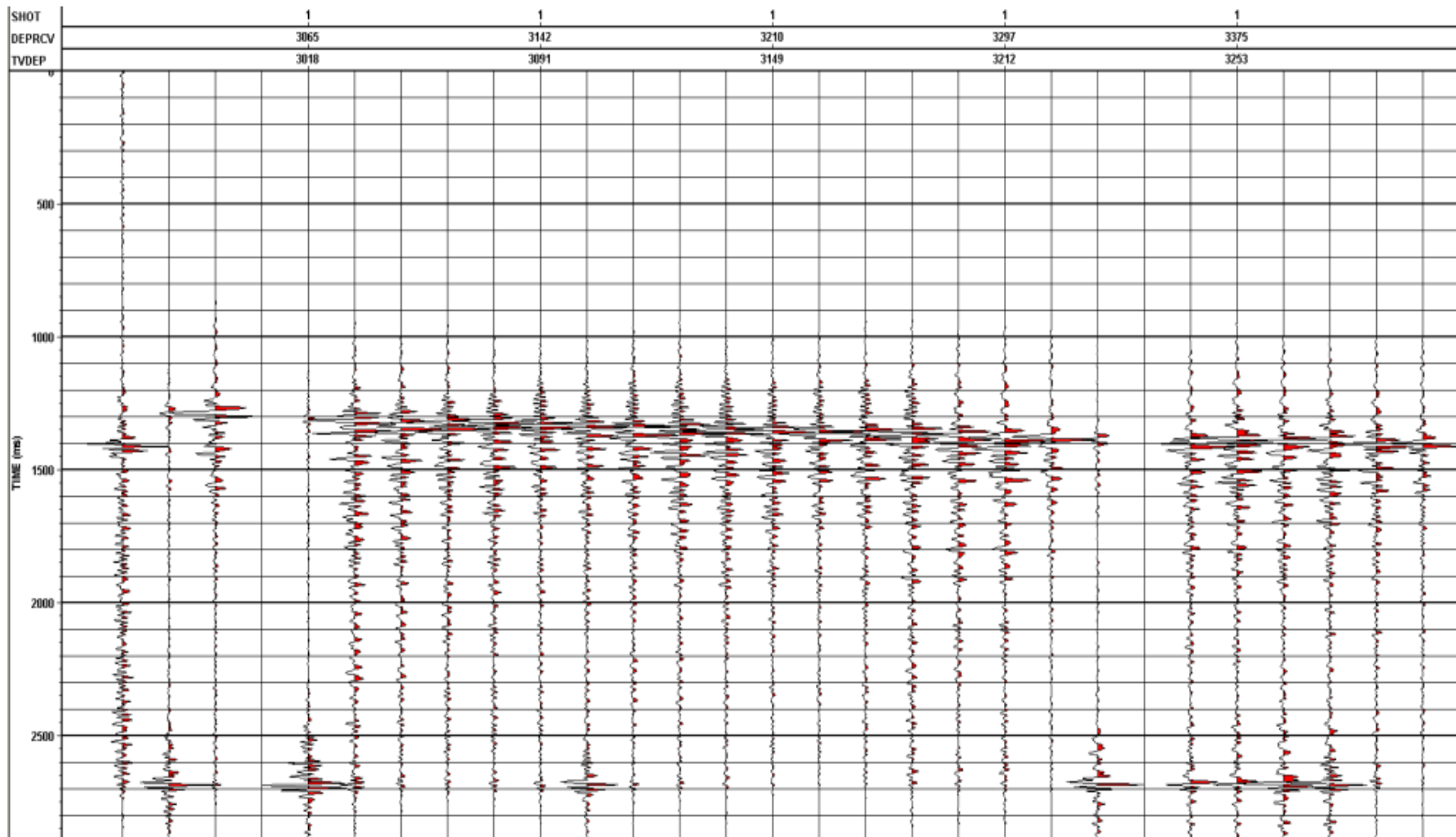


Figure 3.40: Z'' Upgoing P wavefield FRT.

3.9 VSPCDP Transformation and Corridor Stack

In order to image the subsurface at the zone of interest away from the borehole, the VSPCDP transform is used to convert +TT time to offset away from the well and "migrated +TT time". The VSPCDP transform takes the traces recorded at the different depths and, using an input velocity-depth function, stretches the traces over individual locus curves (Hinds et al). The common-depth-point locations are computed by extending the raypaths from the source to the reflecting horizon, through the receiver, and back to the surface. For horizontal layers, the results can be quite good. The curves are regrouped into trace format by a "binning" procedure. The horizontal axis is now offset away from the well.

The main limitation is the maximum offset of the image from the borehole. The angle of incidence changes radically with time for a given offset. Thus, as the offset increases, the probability that the reflection changes into a refraction also increases (Verm et al, 1987).

The deconvolved Z'' Upgoing P wavefield is processed to obtain the VSPCDP transformation and the corridor stack. In figure 3.41, the processing steps are shown and explained analytically.

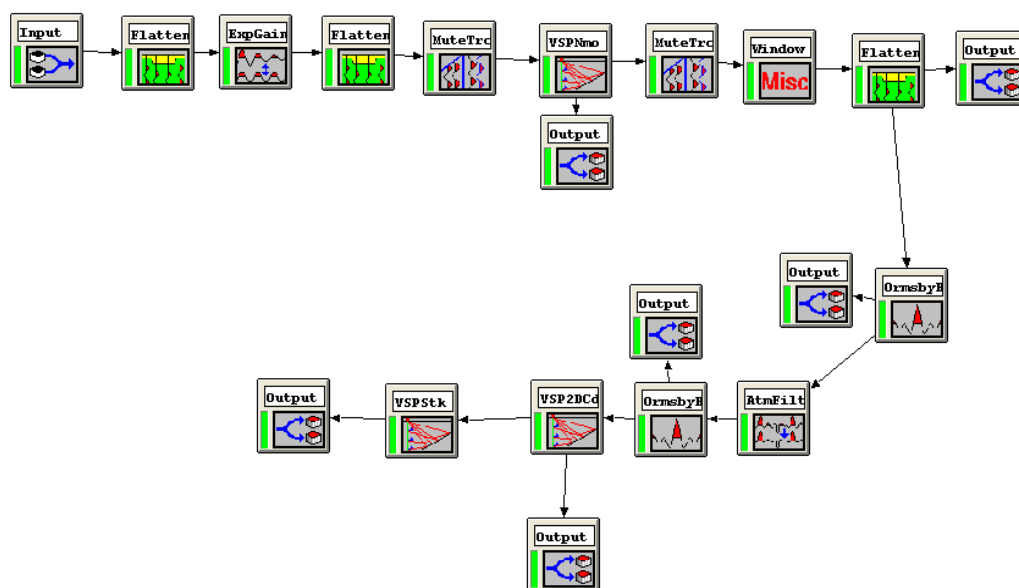


Figure 3.41: Processing flow to receive VSPCDP and Corridor Stack.

The input Z'' Upgoing P wavefield FRT is sorted to the Trace-ID-Code. In order to correct for spherical spreading and transmission losses and to compensate for reflection amplitude loss below the level of geophone, an exponential correction was applied to this waveform with exponent equal to 1.0, flattened to an event at 1200 ms. The next step is to correct the upgoing wavefields for normal moveout (NMO). A reverse flatten is used before normal moveout correction in order to remove the previous applied static and to place data in field recorded time. The NMO traveltimes are calculated by ray tracing through the P-wave velocity mode. In figure 3.42, the result after NMO correction are presented. The traces at the shallower depth include the most coherent energy. An amount of random noise can be detected as the depth increases. Also observed is the absence of energy on some traces at different depths. A five-trace median filter was applied on the NMO-corrected upgoing P wavefield to attenuate the random noise and to make visible the energy (figure 3.43). Despite this, the incoherent signal still remains on the deepest parts of traces. Furthermore, muting is applied after NMO correction to avoid excessive stretch effects.

Since the first-break traveltime corresponds to the one-way vertical P-wave traveltime from the source to the receiver, the upgoing P-wave traveltimes are shifted to two-way time by shifting each trace by the first-break time (figure 3.44). Additionally, two band-pass filters and a five-trace median filter (before the second band pass filter) are used to remove the unwanted time. The bandwidth of both band-pass filters is 5/10-60/70 Hz. The results of the band-passes filters are shown in figures 3.45 and 3.46.

The next step in the processing flow was to map the upgoing P wavefield to the correct offset positions. The data were binned into 5 m bins centered every 5 m.

A corridor extending from the first-break time down 4000 ms extracted from the upgoing P-waves and stacked to obtain the final VSP trace. The corridor extends to the end of the data to include reflections from below the well. A corridor of the VSP data is useful since the reflected energy traveled back up to the borehole, it includes multiples and other wave phenomena that cannot be controlled in processing. The VSPCDP transform and the corridor stack are shown in figure 3.47.

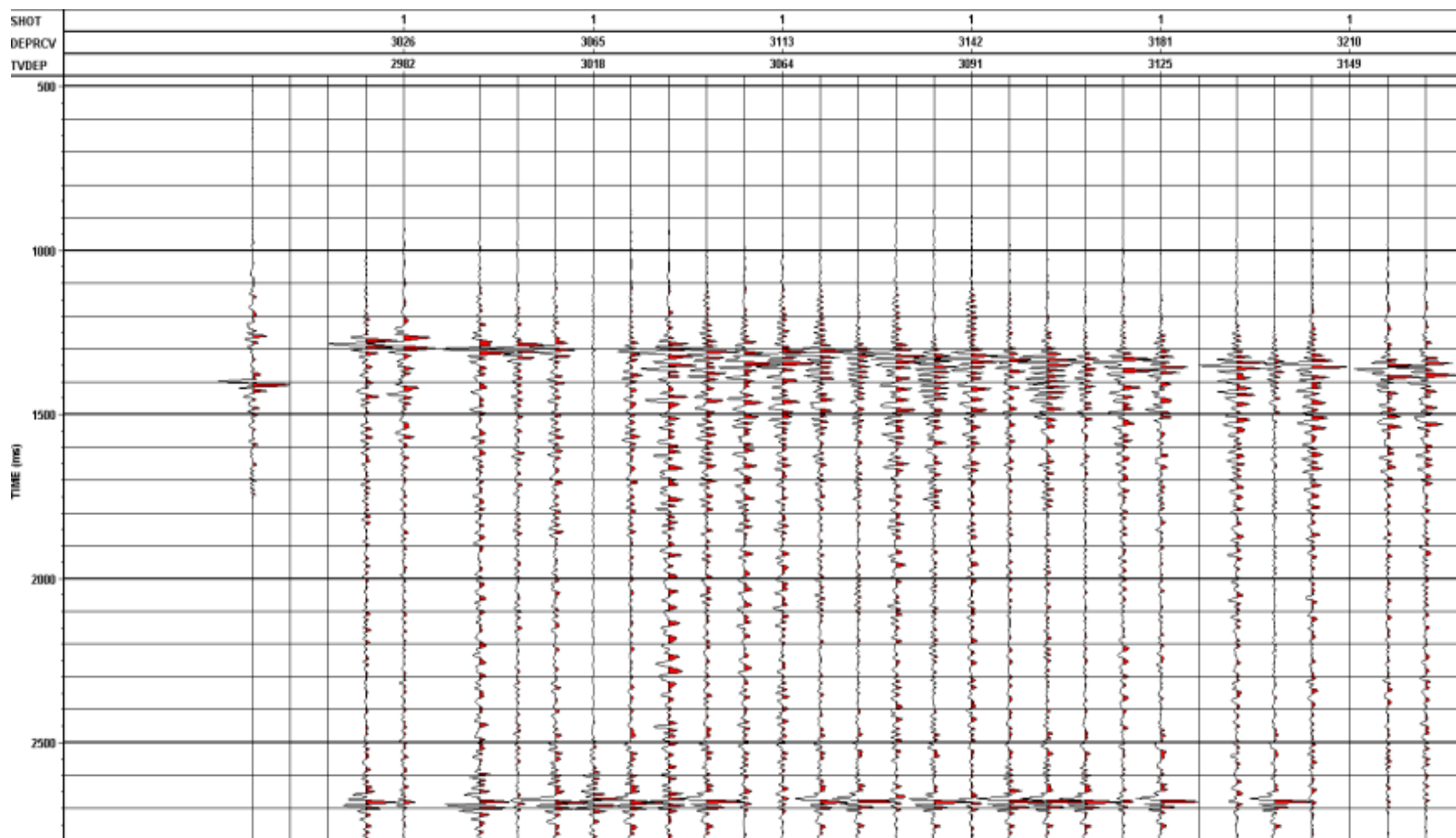


Figure 3.42: Normal Moveout Correction.

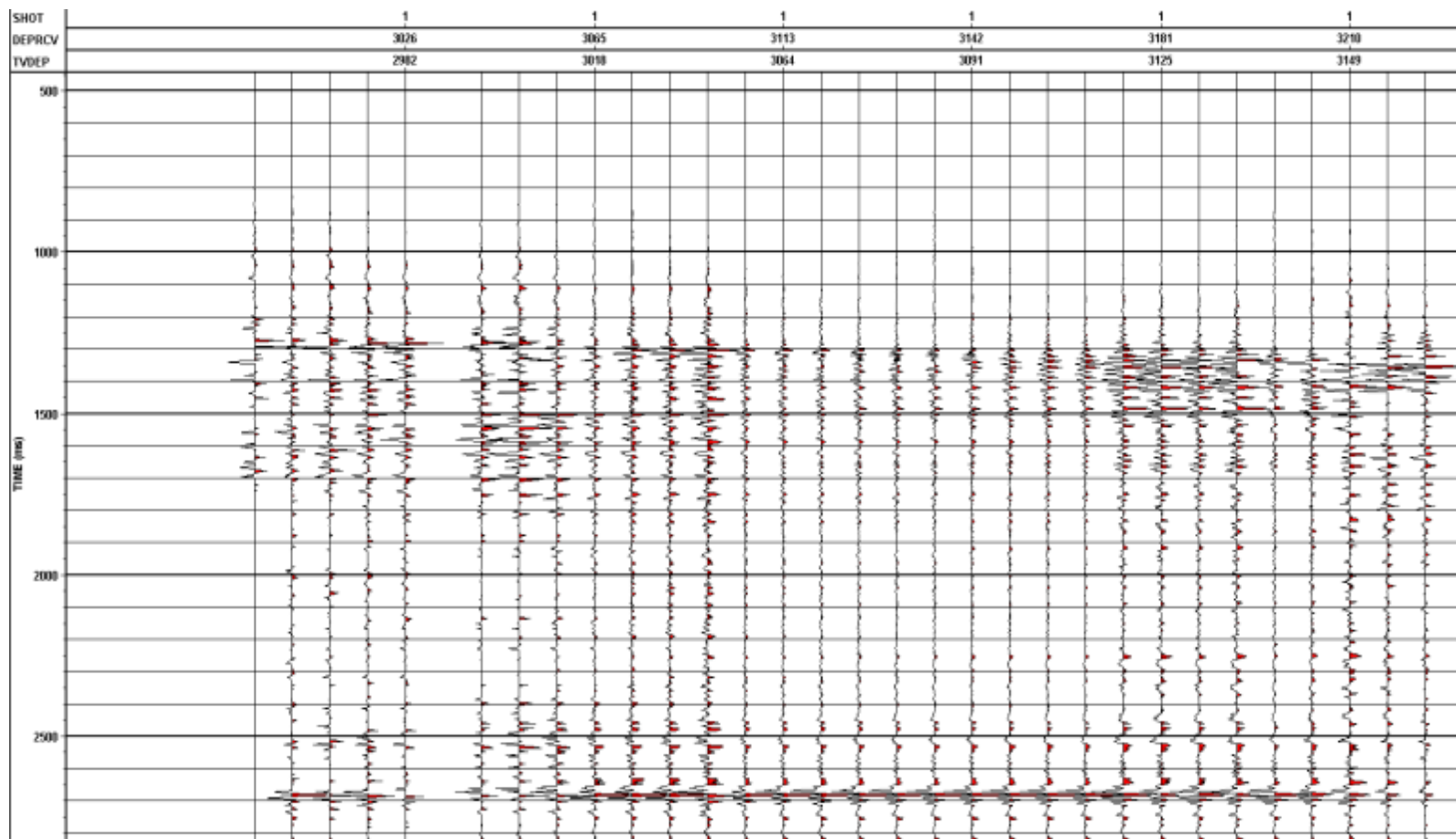


Figure 3.43: Normal Moveout Correction after a median filter application.

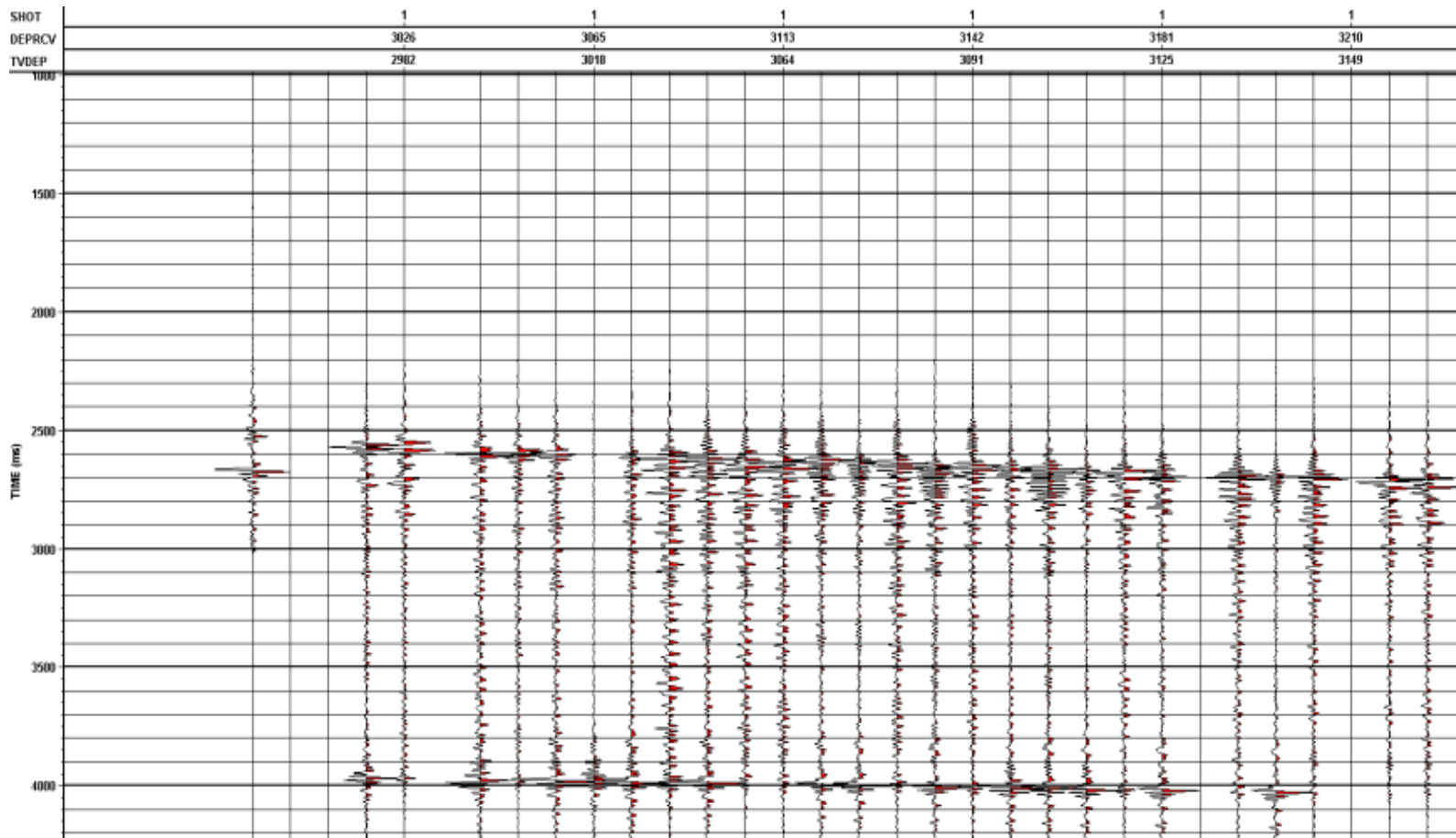


Figure 3.44: Shifting to two-way time after NMO Correction.

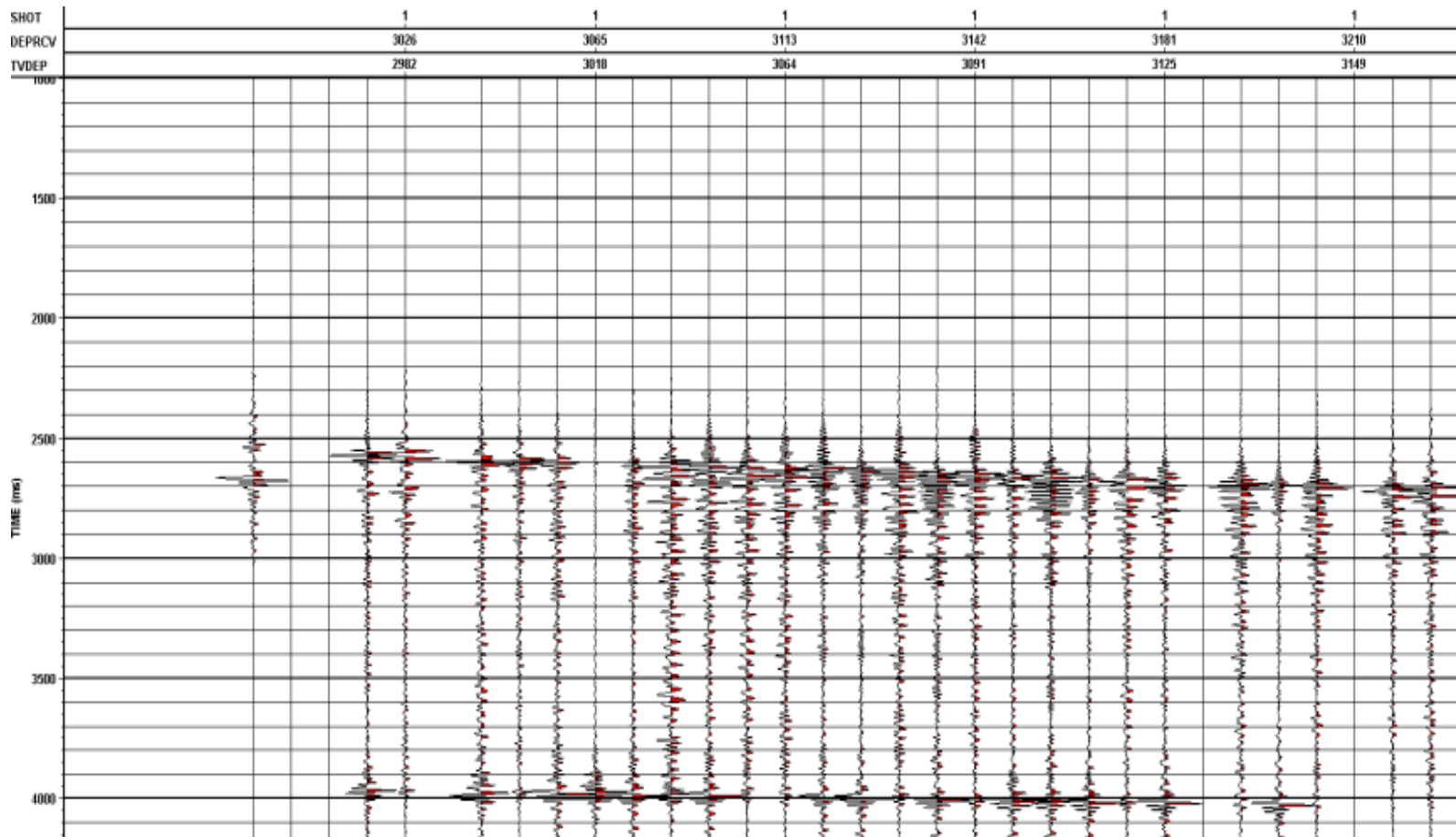


Figure 3.45: Output of the first band-pass filter.

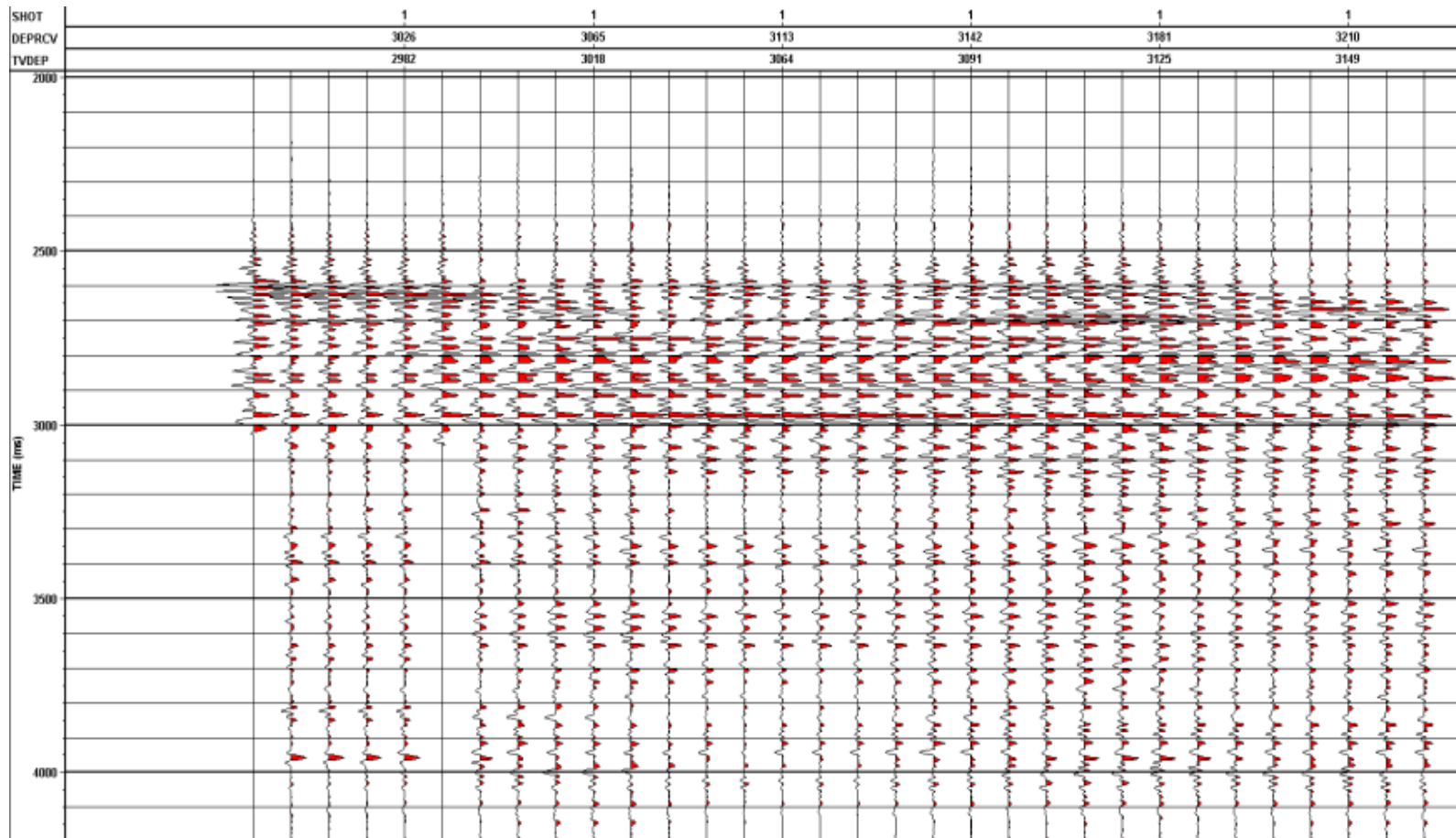


Figure 3.46: Output after the five-trace median filter and the second band-pass filter.

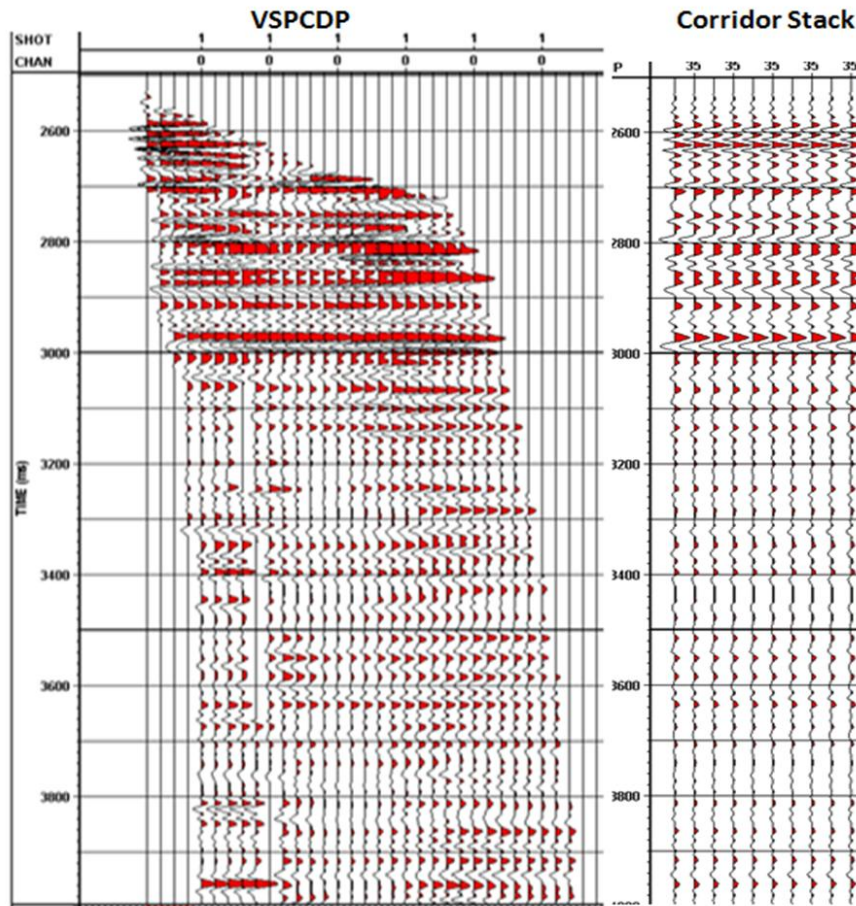


Figure 3.47: VSPCDP Transformation on the left and the Corridor Stack on the right.

Several filtering bandwidths have been tested before the last decision of a 5/10-60/70 Hz band-pass filter was selected to create the corridor stack. In particular, the figure 3.48 presents five corridor stacks at different common-depth-points (CDP) and bandwidths. For the first four corridor stacks the bandwidths 7/10-40/50 Hz, 10/20-40/60 Hz, 0/5-60/70 Hz and 5/10-60/70 Hz have been used, respectively, and the CDP is equal to 35. The last corridor stack has CDP equal to 34 and bandwidth 5/10-60/70 Hz.

The selected corridor stack is the fourth one since it has higher vertical resolution.

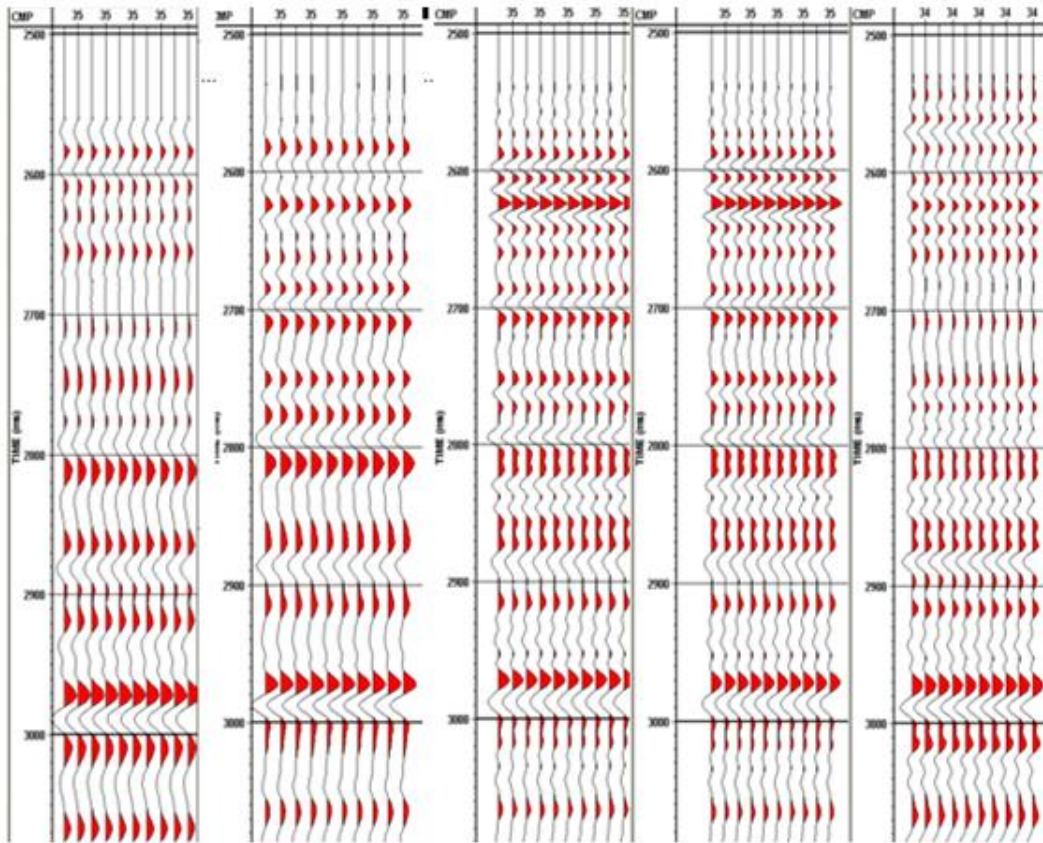


Figure 3.48: Corridor Stacks resulting from different filter application.

CHAPTER 4: Interpretation and Conclusion

4.1 Interpretation

In this section the interpretation of the processing result is discussed. As it has already been mentioned, it is not possible to identify the lithology since there is no available information of well and sonic logs. The resulting corridor stack from the current processing represents the data recorded in the memory tool. The corridor stacks that Schlumberger provided are the processing result of both the real-time and recorded memory data. Those corridor stacks must be similar.

In figure 4.1, the resulting VSP2DCDP and the corridor stack are presented, extending from 2500 ms to 3100 ms where the area of interest is. Six events can be identified and are shown in dashed lines. In what follows, a zero-phase wavelet with a central peak or trough is referred to simply as a peak, and similarly for a trough. The strong trough followed by strong peak imply change in the characteristics of the subsurface in porosity, density, liquid saturation causing different reflection coefficient.

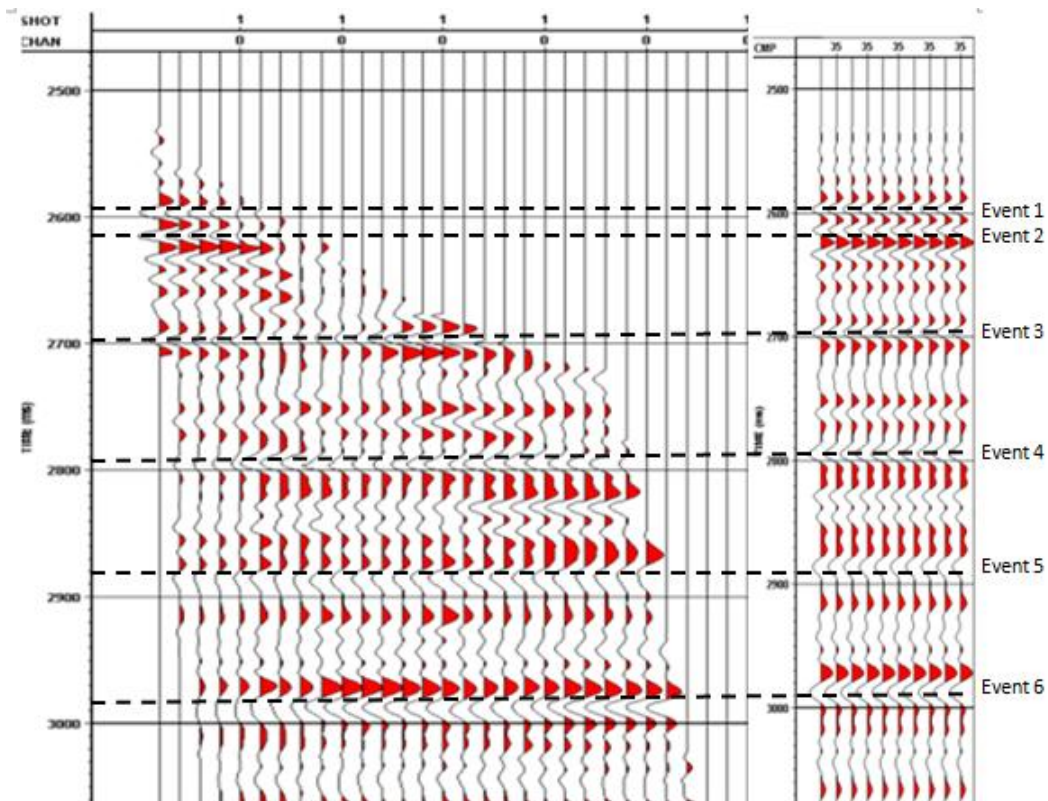


Figure 4.1: Recognized events over the VSP2DCDP and Corridor Stack.

The next step is to try to identify those six events on the provided corridor stack of the recorded-memory data. In figure 4.2, the identification of those events and the interpretation with the resulting corridor stack is illustrated. The two corridor stacks provided by the company resulted from different bandwidth filters. On the first one, no band pass filter has been applied, while on the second one a filter with a bandwidth from 7 to 60 Hz has been applied. (Recall that the filter's bandwidth applied on the resulting corridor stack in section 3.9 is from 5 to 70 Hz). The fact that, slightly different frequencies have been applied to each of them does not cause problems in the interpretation. In fact, five out of the six events have been successfully identified. However, the Event 3 is not confidently correlated. It is regarded that the difference in frequencies causes this problem.

Furthermore, it is fundamental to mention that the target has been detected from the survey to be at 2891 ms two-way-time. The target Tex X Sand is represented as Event 5 in figure 54. In the result of the current thesis, Event 5 is shown at 2888 ms two-way-time. It is considered the difference of 3 ms as quite small since the accuracy of the processing in both cases is under uncertainty.

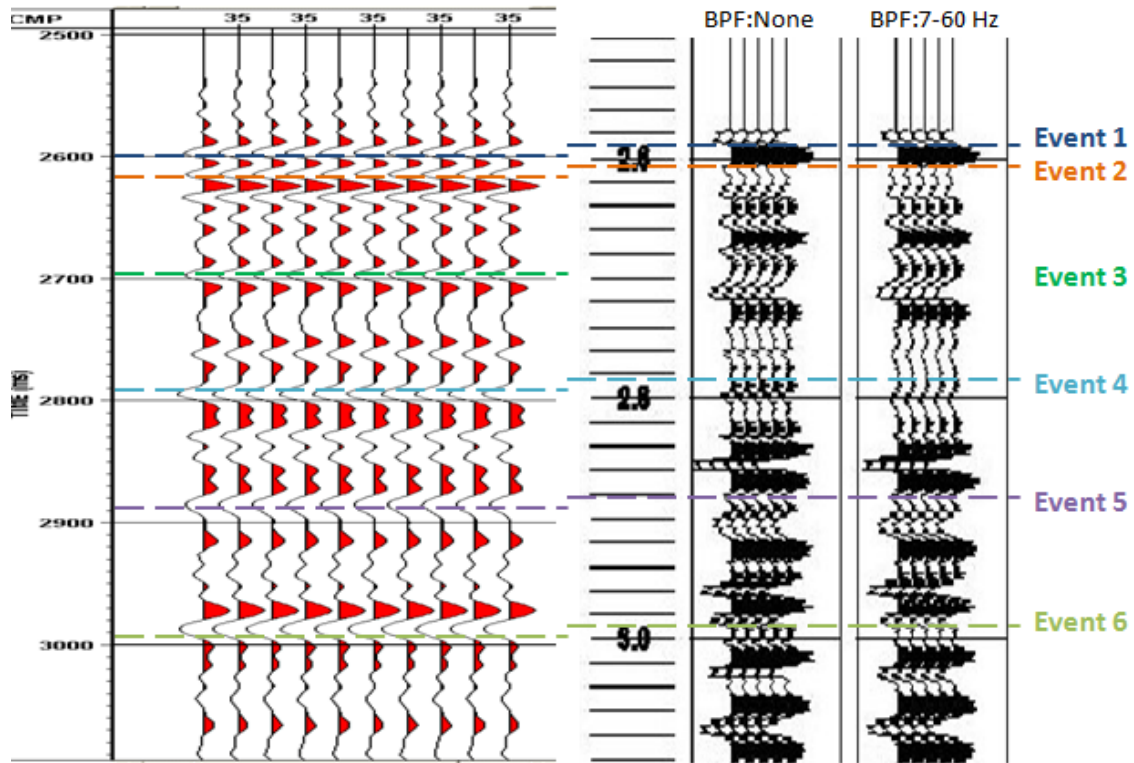


Figure 4.2: Interpretation between the resulting corridor stack(left) and the corridor stack from recorded-memory data provided by Schlumberger (right).

In addition to the recorded-memory data, the interpretation between the resulting of the current project corridor stack from the current project and the one from the real-time data has been carried out (figure 4.3).

To begin with, the frequency of the filter applied on the corridor stack of the real-time data is not known. It is evident that the frequencies are much lower than those of the resulting corridor stack. The six events referred to before are not easily identified. So to help the interpretation a band-pass filter of 0/5-10/20 Hz was applied on the resulting corridor stack. Discrete events at several time depths over both corridor stacks have been identified. In figure 4.3, those events are illustrated. The events are detected with very small, almost negligible, time-depth difference over the corridor stacks. It is observed that generally the two corridor stacks are matching very well.

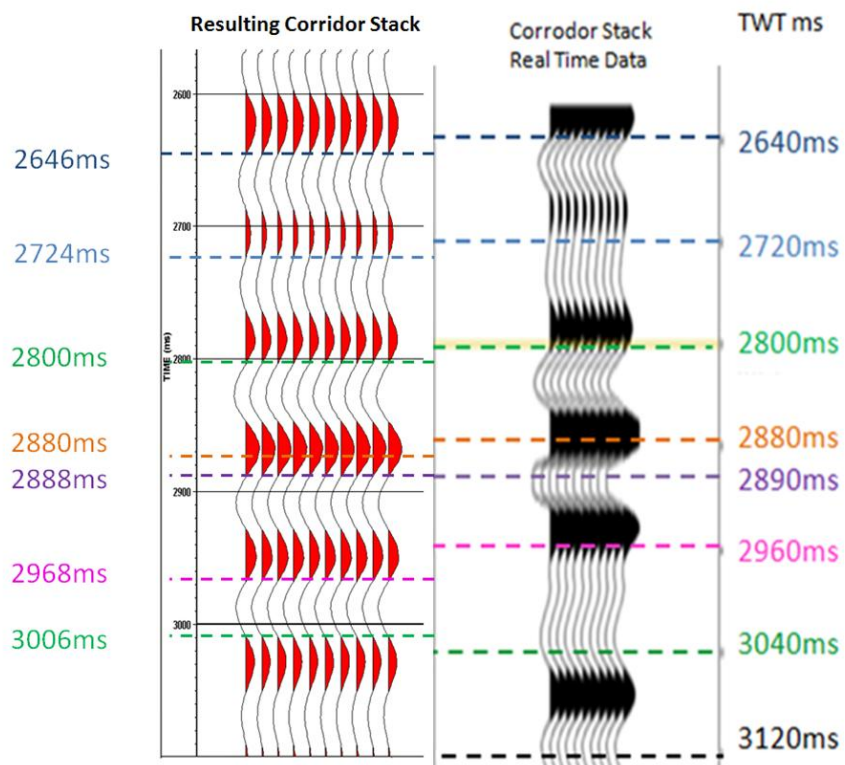


Figure 4.3: Interpretation between the resulting corridor stack (left) and the corridor stack from real-time data provided by Schlumberger (right).

4.2 Conclusion

The processed data are characterized by good quality without significant amount of incoherent signal and with high signal-to-noise ratio. The challenge of the processing focused on the geometry of the survey and the absence of a similar case study in the literature.

The main objective is the detection of the target resulting by the matching between the corridor stacks provided by Schlumberger and that of the current processing. The interpretation among all the three corridor stacks, show very good matching implying the successful identification of the target Tex X Sand through the current processing.

The very good interpretational agreement between real-time and recorded-memory corridor stacks and the extension of them deeper to 4000 ms verify that the VSP-WD method can be successfully used for depth uncertainty reduction and look ahead investigation.

Bibliography

Anchliya A., 2006, A Review of SWD Techniques: A journey from 1986 to 2005: SPE European/EAGE Annual Conference and Exhibition, Viena, Austria.

Althoff G., Cornish B., Varsamis G., Kavaipatti B., Arian A., Wisniewski L.T., Blanch O.J., and Cheng A.C., 2004, New concepts for seismic surveys while drilling: SPE Annual Technical Conference and Exhibit, Houston, Texas.

Baker Huges, 1997, Baker Huges INTEQ's guide to measurement while drilling information guide.

Coppens F., Mari J.-L., 1991, Seismic well surveying: Editions Technip, Paris.

Dethloff M. H., Petersen A. S., 2007, Seismic-while-drilling operation and applications: SPE, California.

Esmersoy C., Underhill W., Hawthorn A., 2001, Seismic measurement while drilling: Conventional borehole seismics on LWD. Schlumberger Sugar Land Product Center SPWLA 42nd Annual Logging Symposium.

Gaiser J. E., and Di Siena J.P., 1983, Marine vertical seismic profiling: Offshore Technology Conference, Houston, Texas, OTC 4541.

Hardage B., 2009, Seismic-While-Drilling: Techniques using the drill bit as the seismic source: Search and Discovery Article, Texas.

Hernández G., Campos H., Bautista R., Brewer J.R., Torne J., Perez R., and Barrios O., 2007, New technologies and applications for the vertical seismic profile as a lithostructural tool and "look ahead" mode. Mexico: SPE International.

Hernández G., Casares M., Perez R., Barrios O., Bautista R., Brewer J.R., Torne J., 2007, "Look ahead" applications of vertical seismic profiles as a litho-structural tool combined with dipole sonic logging: Case histories-Burgos Basin- Northern Mexico: 48th Annual Logging Symposium, Texas.

Hinds R.C., Kuzmiski R.D, Botha W.J., Anderson N.L., Chapter 12. Vertical and lateral seismic profiles: P.h.D. University of Pretoria.

Knight J.M., 1987, Deviated well VSP's in high-dip structures: Offshore Technology Conference, Houston, Texas, OTC 5571.

Kuzmiski R., Charters B., Galbraith M., 2009, Processing considerations for 3D VSP: CSEG RECORDER, Alberta, Canada.

Labonté S., 1990, Modal separation, mapping and inverting three-component VSP data. In: M.Sc. Thesis. The University of Calgary.

Lee M.W., and Balch A.H., 1983, Computer processing of vertical seismic profile data: 48, 272-287.

Price R. C., 1990, High resolution seismic source specifications applications and misapplications: Geodetic International Inc, Houston, Texas.

Poletto F., and Miranda F., 2004, Seismic while drilling fundamentals of drill-bit seismic for exploration: ELSEVIER, , Italy, vol 35, ISBN 0-080-43928-4.

Sengbush R.L., and Al-Fares M.H., 1987, Optimal processing of VSP data: Offshore Technology Conference, Houston, Texas.

Sheriff R.E., and Geldart P.L., 1995, Exploration Seismology: Press Syndicate of the University of Cambridge, New York, ISBN 0-521-46282-7.

Stewart R.R., 1984, VSP interval velocities from travelttime inversion: Geophys. Prop., 32, 608-628.

Underhill W., Esmersoy C., Hawthorn A., Hashem M., Hendrickson J., Scheibel J., 2001, Demonstration of real-time borehole seismic from an LWD tool: SPE Annual Technical Conference, New Orleans, Louisiana.

Verm R.W., Hilterman F.J and Liang L.C., 1987, Imaging VSP's 3 kilometers beyond the borehole receiver: Offshore Technology Conference, Houston, Texas.

Wise G.L., and Gallagher N.C., 1981, A theoretical analysis of the properties of median filters. Lafayette: IEEE Transactions on Acoustic, Speech, and Signal Processing.

Appendix A

First Rotation

Table A- 1 : Rotation Angles and Bearing from the First Rotation.

Level	TVD	Rotation angle	Bearing
1	2926.73	212.99	237.01
2	2964.23	153.97	296.03
3	2981.74	156.92	293.08
4	2990.88	170.62	279.38
5	3009.05	207.30	242.70
6	3018.19	292.68	157.32
7	3036.42	49.60	40.40
8	3045.32	317.18	132.82
9	3063.85	173.91	276.09
10	3072.32	137.75	312.25
11	3090.92	331.64	118.36
12	3099.39	248.29	201.71
13	3116.85	58.91	31.09
14	3124.87	189.14	260.86
15	3141.33	184.42	265.58
16	3148.89	283.21	166.79
17	3164.12	202.75	247.25
18	3171.32	322.82	127.18
19	3185.71	166.11	283.89
20	3192.26	160.57	289.43
21	3211.68	224.72	225.28
22	3223.49	123.74	326.26
23	3228.90	206.19	243.81
24	3229.05	3.72	86.28
25	3239.08	25.45	64.55
26	3243.53	254.41	195.59
27	3252.64	112.01	337.99
28	3257.00	156.08	293.92
29	3266.54	283.09	166.91
30	3271.22	204.81	245.19
31	3285.71	169.90	280.10
32	3296.05	181.05	268.95

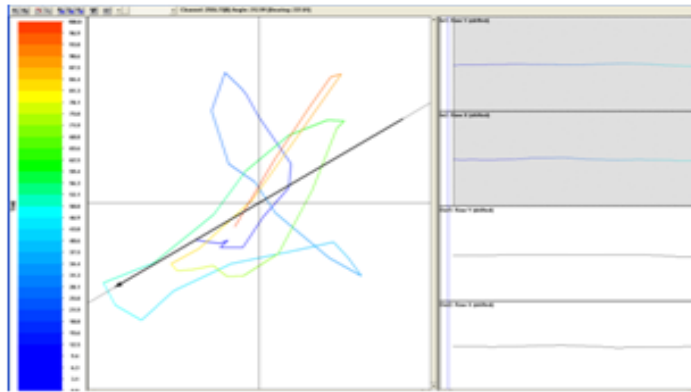


Figure A-1: Hodogram at 2926.73m depth.

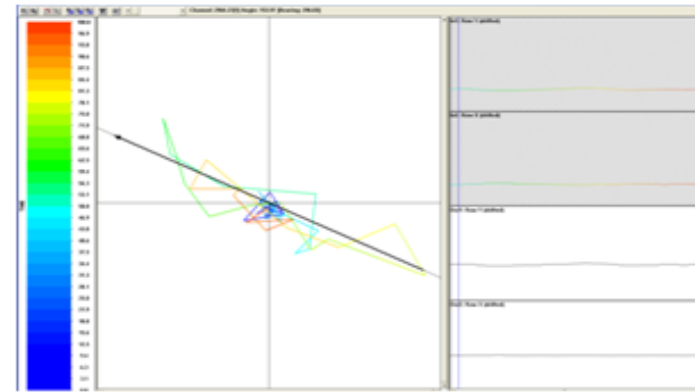


Figure A-2: Hodogram at 2964.23m depth.

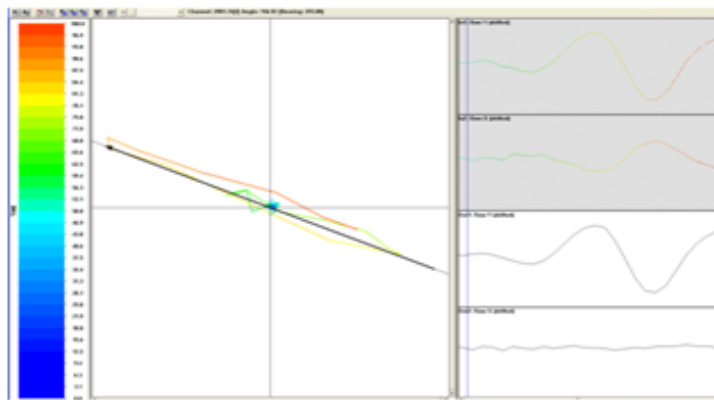


Figure A-3: Hodogram at 2981.74m depth.

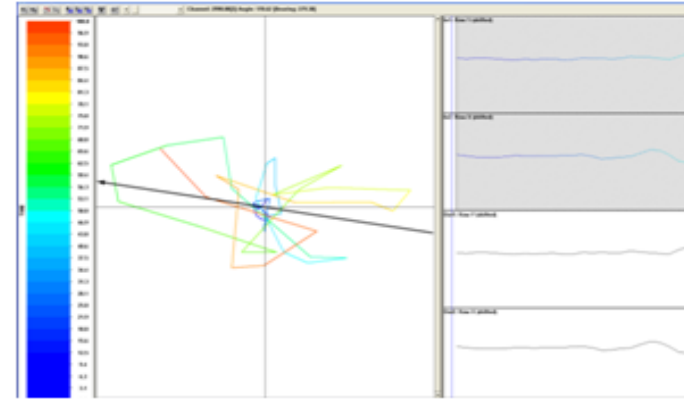


Figure A-4: Hodogram at 2990.88m depth.

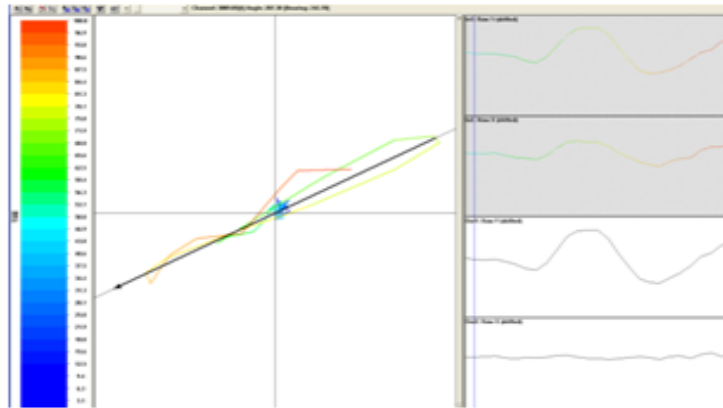


Figure A-5: Hodogram at 3009.05m depth.

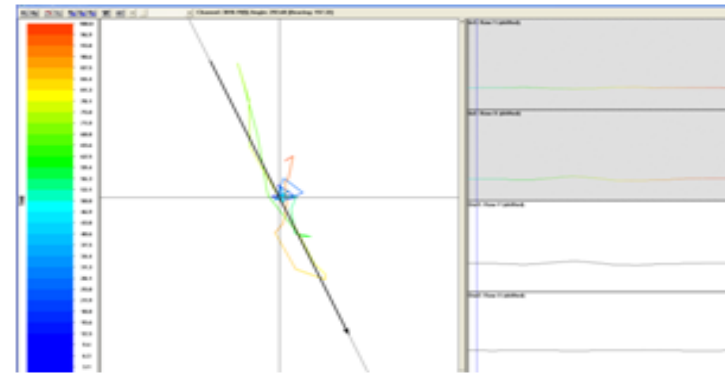


Figure A-6: Hodogram at 3018.19m depth.

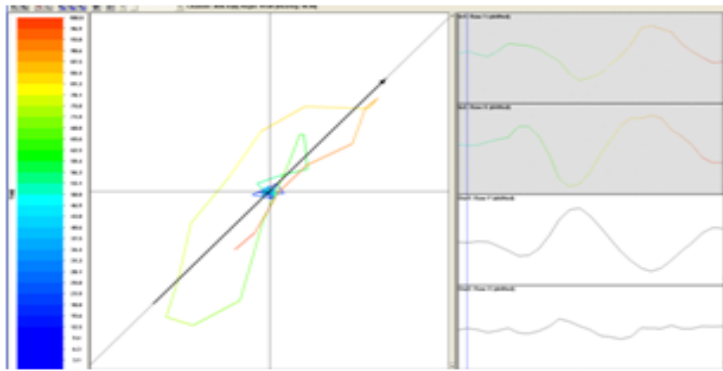


Figure A-7: Hodogram at 3036.42m depth.

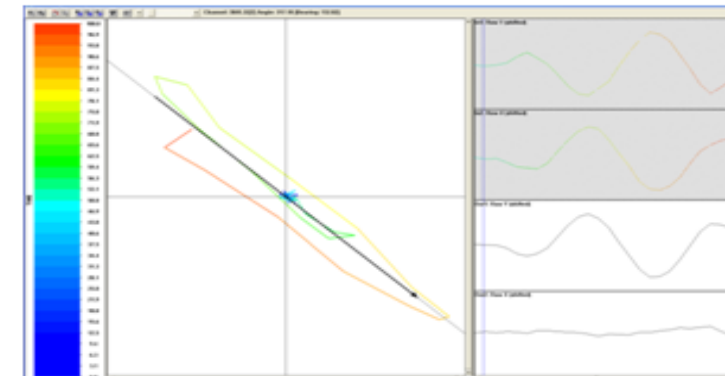


Figure A-8: Hodogram at 3045.32m depth.

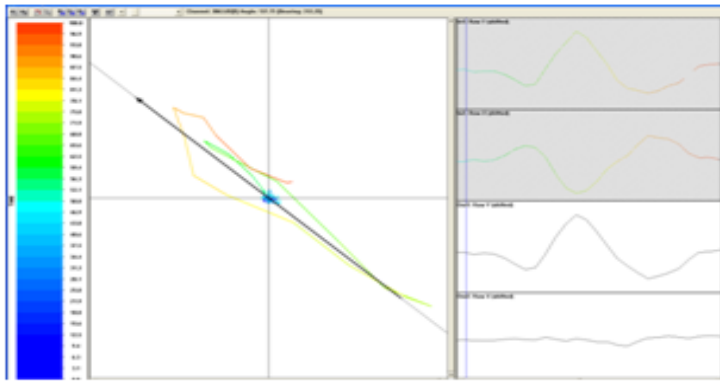


Figure A-9: Hodogram at 3063.85m depth.

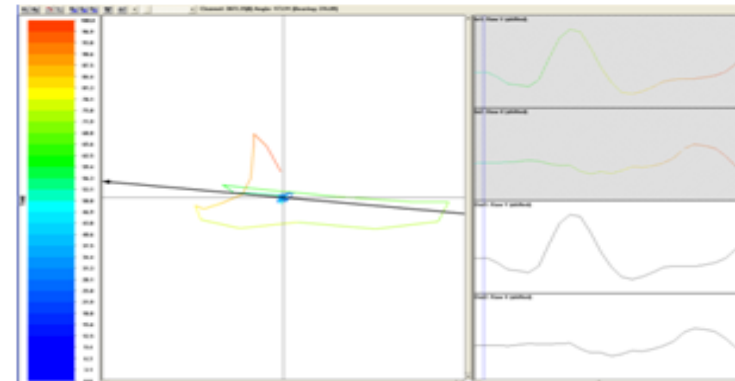


Figure A-10: Hodogram at 3072.32m depth.

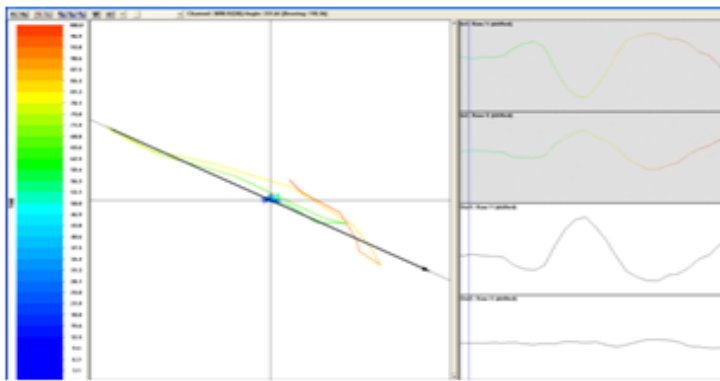


Figure A-11: Hodogram at 3090.92m depth.

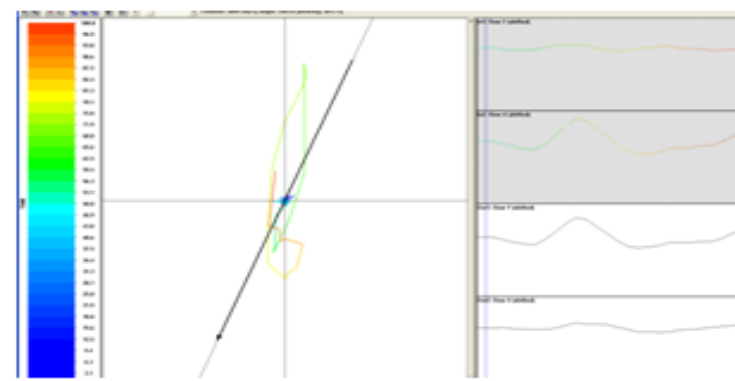


Figure A-12: Hodogram at 3099.39m depth.

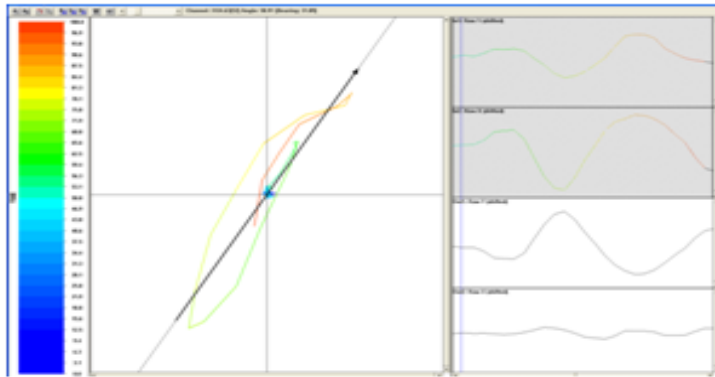


Figure A-13: Hodogram at 3116.85m depth.

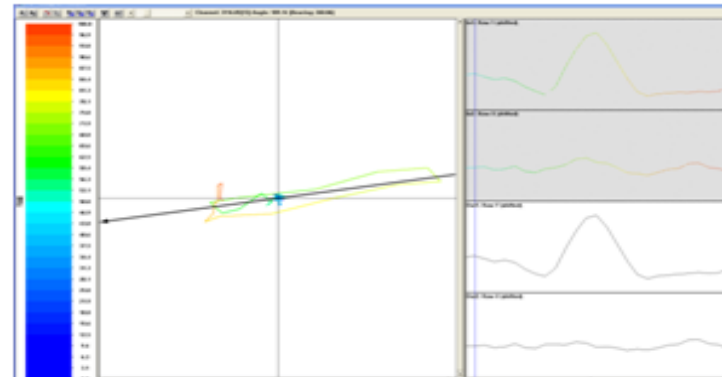


Figure A-14: Hodogram at 3124.63m depth.

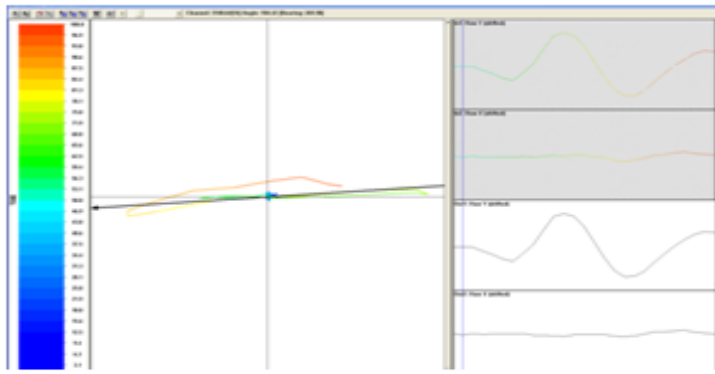


Figure A-15: Hodogram at 3141.33m depth.

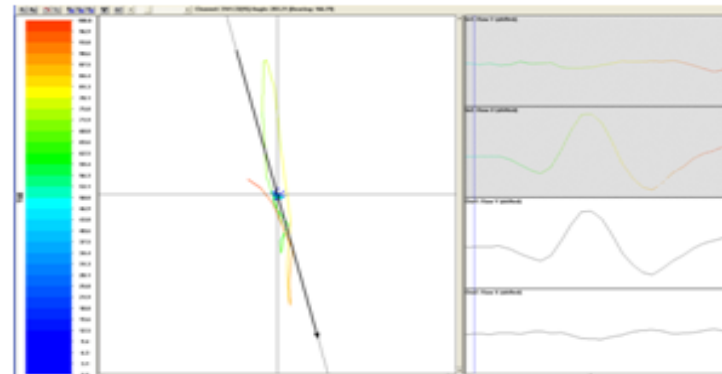


Figure A-16: Hodogram at 3148.64m depth.

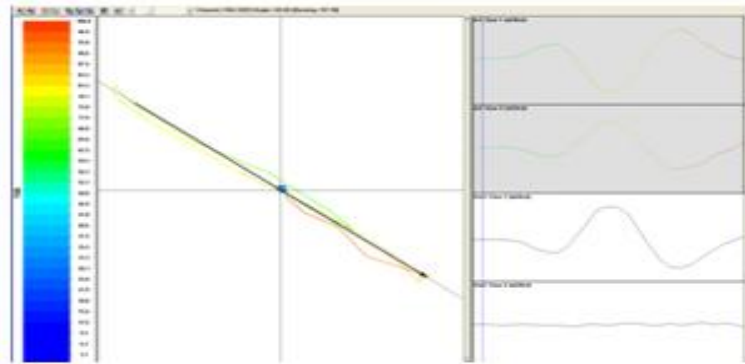


Figure A-17: Hodogram at 3164.12m depth.

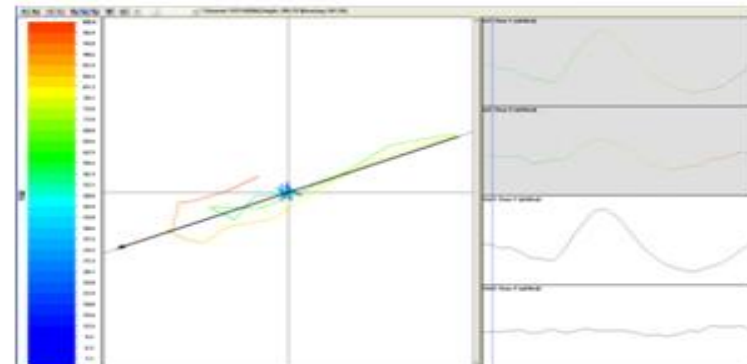


Figure A-18: Hodogram at 3171.03m depth.

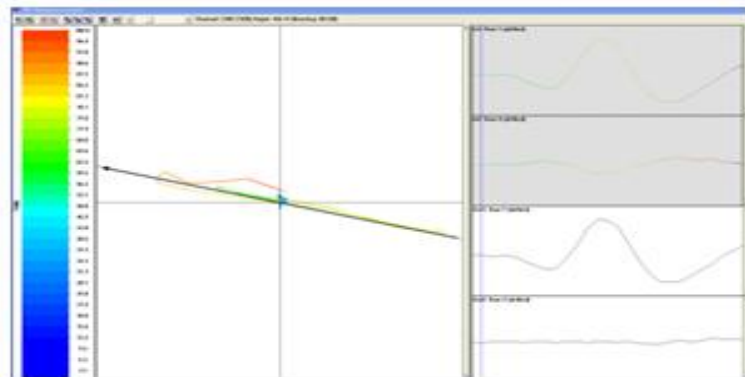


Figure A-19: Hodogram at 3185.71m depth.

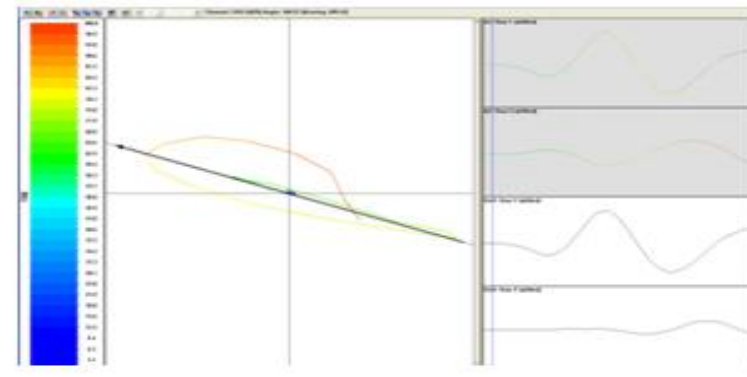


Figure A-20: Hodogram at 3192.26m depth.

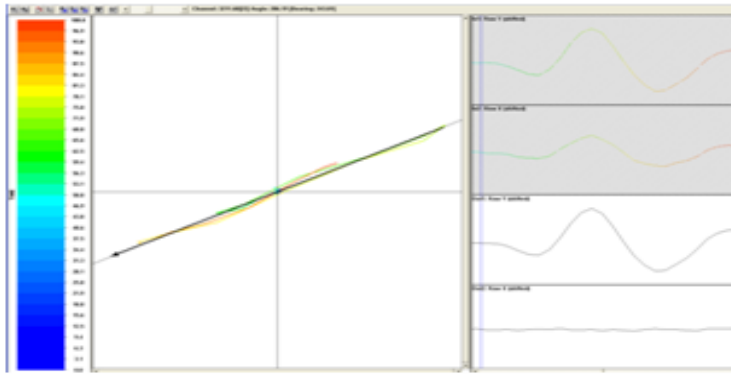


Figure A-21: Hodogram at 3211.68m depth.

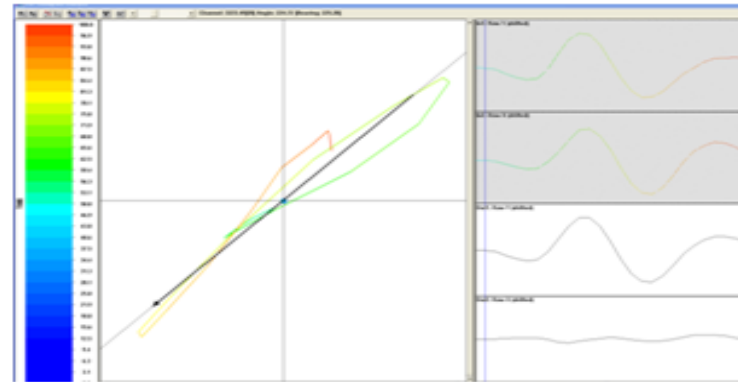


Figure A-22: Hodogram at 3223.49m depth.

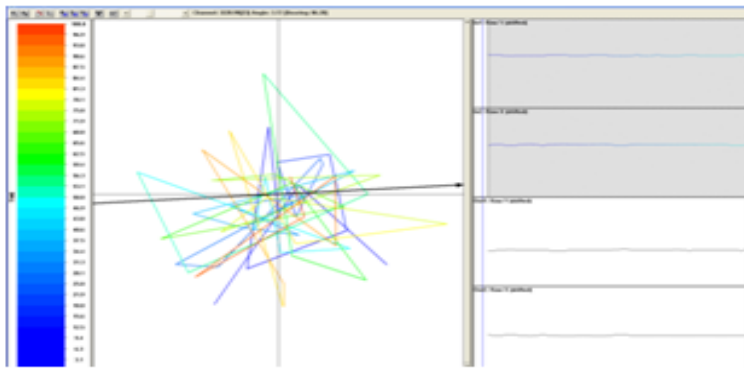


Figure A-23: Hodogram at 3228.90m depth.

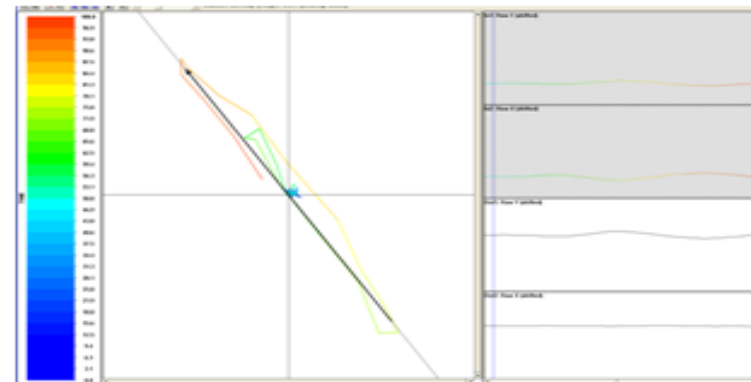


Figure A-24: Hodogram at 3229.03m depth.

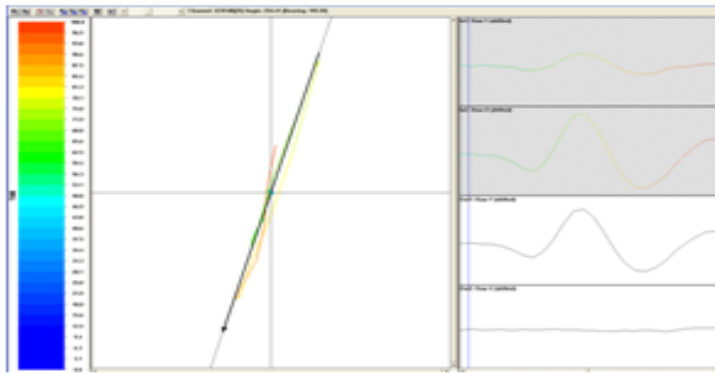


Figure A-25: Hodogram at 3239.08m depth.

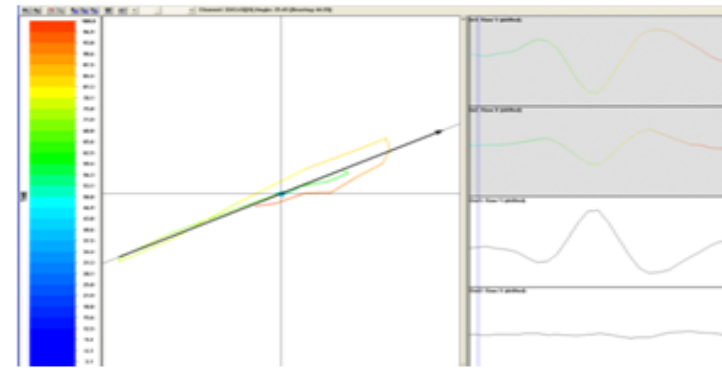


Figure A-26: Hodogram at 3243.53m depth.

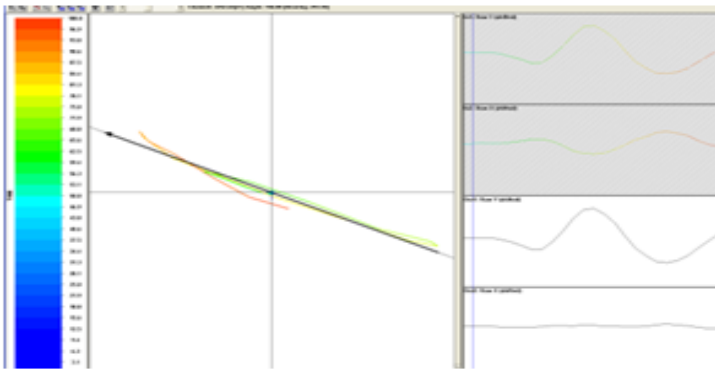


Figure A-27: Hodogram at 3252.64m depth.

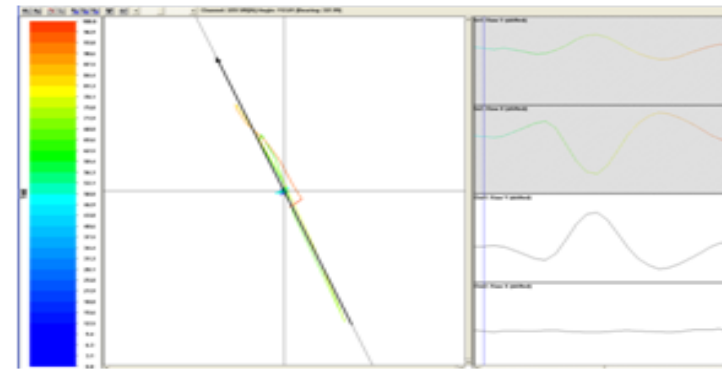


Figure A-28: Hodogram at 3257.00m depth.

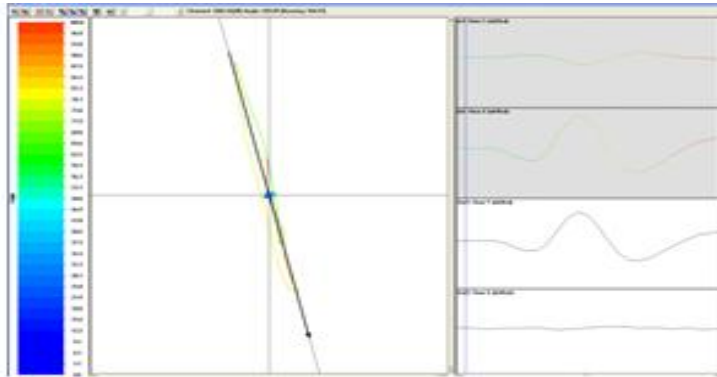


Figure A-29: Hodogram at 3266.54m depth.

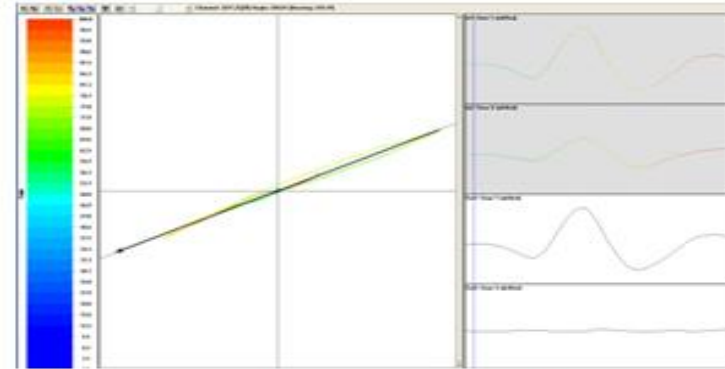


Figure A-30: Hodogram at 3271.22m depth.

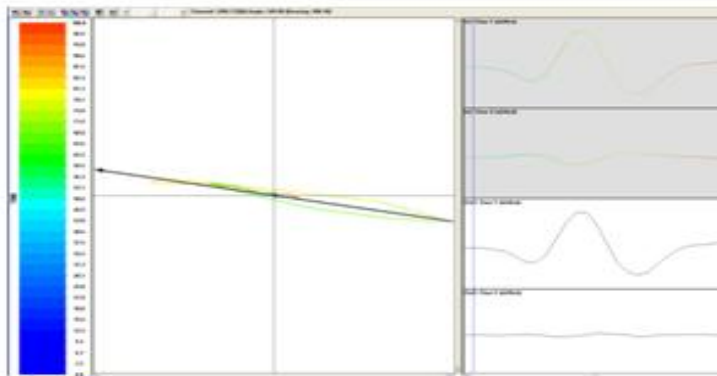


Figure A-31: Hodogram at 3285.71m depth.

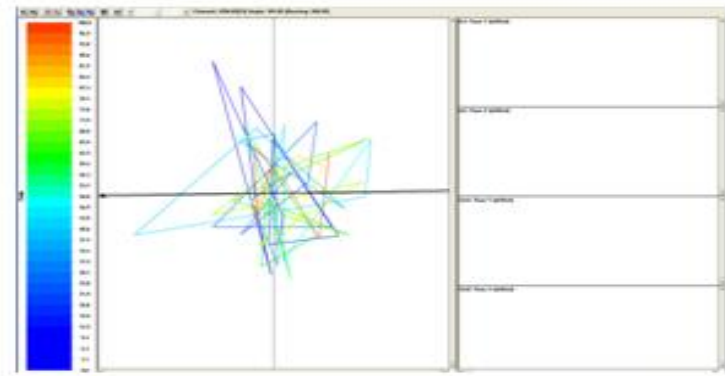


Figure A-32: Hodogram at 3296.05m depth.

Appendix B

Second Rotation

Table B- 1: Rotation Angles and Bearing from the Second Rotation.

Level	TVD	Rotation angle	Bearing
1	2926.73	122.13	327.87
2	2964.23	16.11	73.89
3	2981.74	153.47	296.53
4	2990.88	179.92	270.08
5	3009.05	155.14	294.86
6	3018.19	152.56	297.44
7	3036.42	153.63	296.37
8	3045.32	157.15	292.85
9	3063.85	161.26	288.74
10	3072.32	156.12	293.88
11	3090.92	143.61	306.39
12	3099.39	155.37	294.63
13	3116.85	151.25	298.75
14	3124.87	147.50	302.50
15	3141.33	140.87	309.13
16	3148.89	140.70	309.30
17	3164.12	134.49	315.51
18	3171.32	142.37	307.63
19	3185.71	128.84	321.16
20	3192.26	127.10	322.90
21	3211.68	123.94	326.06
22	3223.49	118.13	331.87
23	3228.90	184.96	265.04
24	3229.05	118.88	331.12
25	3239.08	116.26	333.74
26	3243.53	107.92	342.08
27	3252.64	118.66	331.34
28	3257.00	114.44	335.56
29	3266.54	115.50	334.50
30	3271.22	119.44	330.56
31	3285.71	122.32	327.68
32	3296.05	6.84	83.16

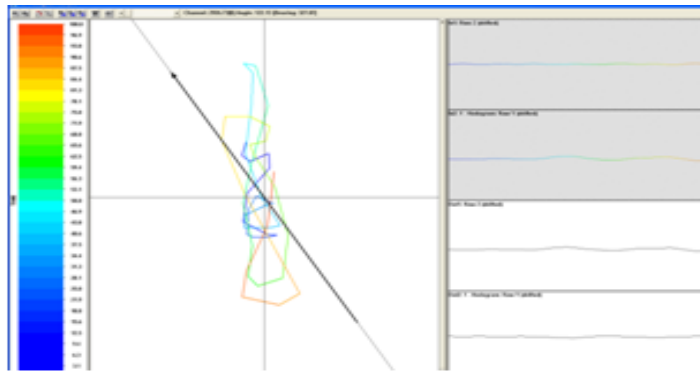


Figure B-1: Hodogram at 2926.73m depth.

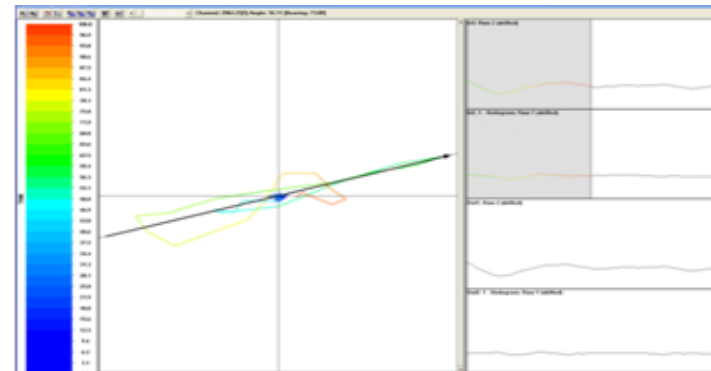


Figure B-2: Hodogram at 2964.23m depth.

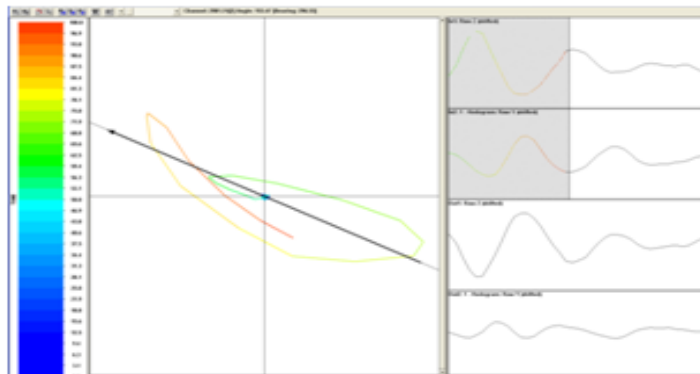


Figure B-3: Hodogram at 2981.74m depth.

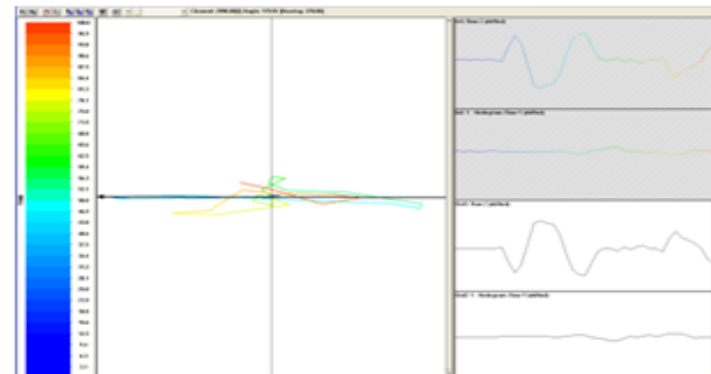


Figure B-4: Hodogram at 2990.88m depth.

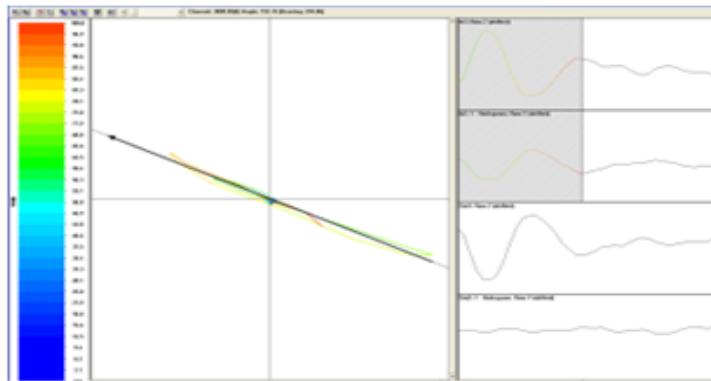


Figure B-5: Hodogram at 3009.05m depth.

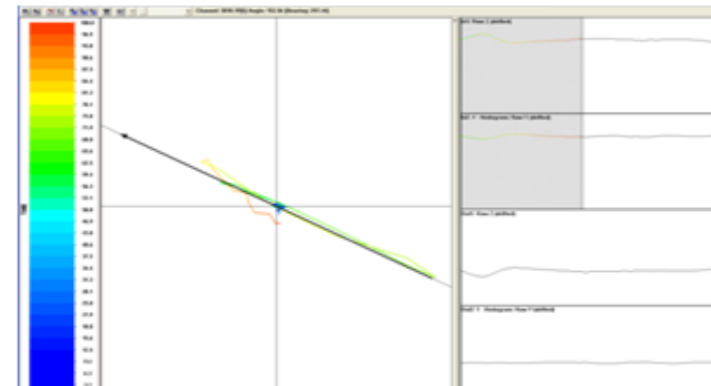


Figure B-6: Hodogram at 3018.19m depth.

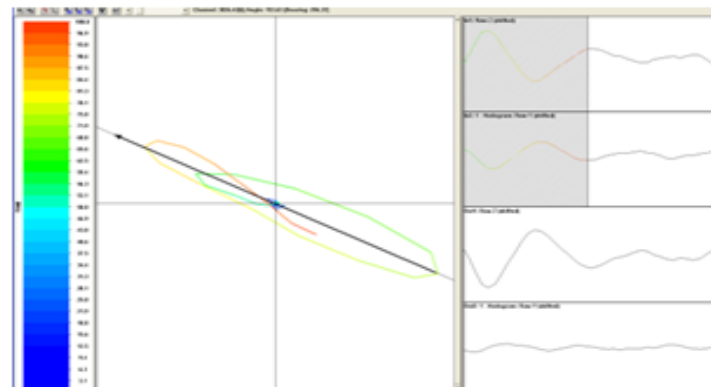


Figure B-7: Hodogram at 3036.42m depth.

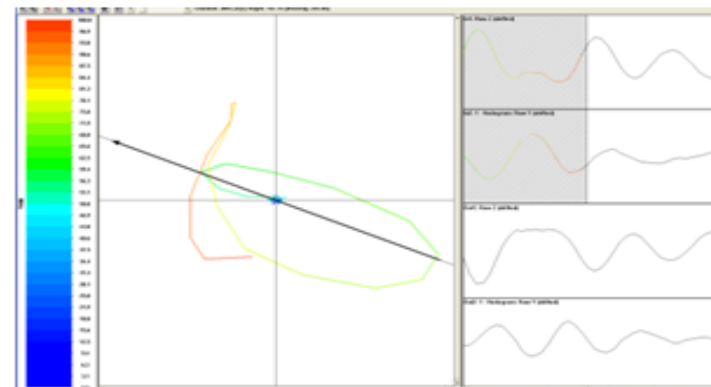


Figure B-8: Hodogram at 3045.32m depth.

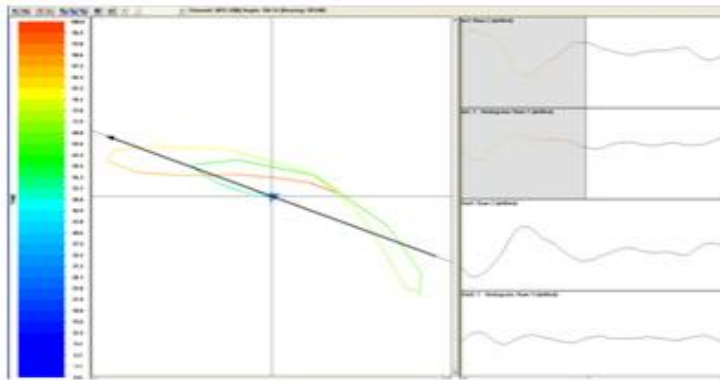


Figure B-9: Hodogram at 3063.85m depth.

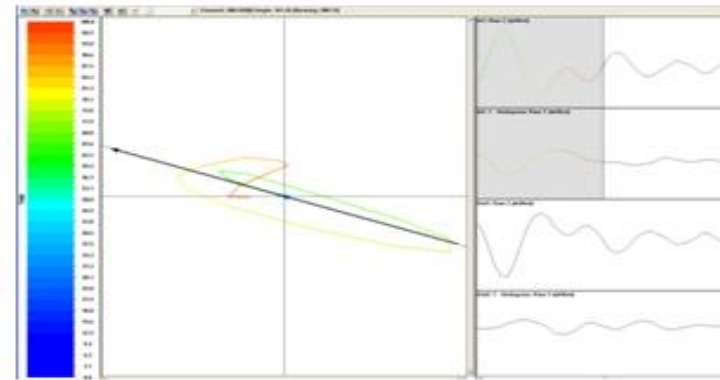


Figure B-10: Hodogram at 3072.32m depth.

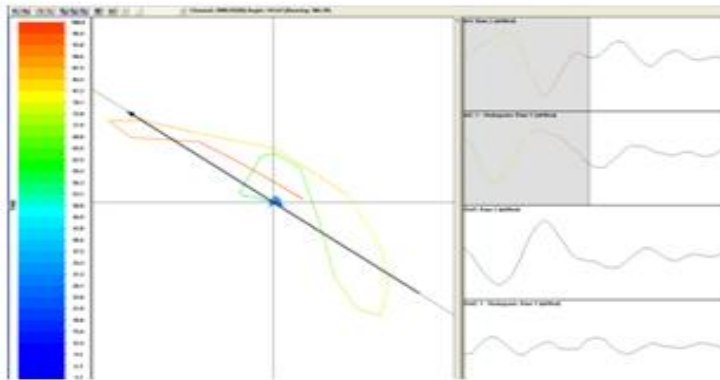


Figure B-11: Hodogram at 3090.92m depth.

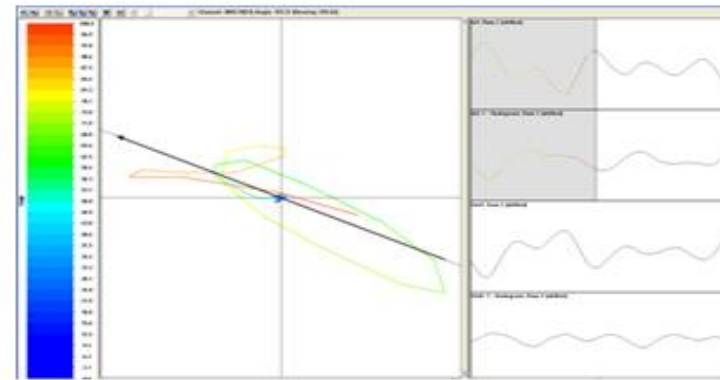


Figure B-12: Hodogram at 3099.39m depth.

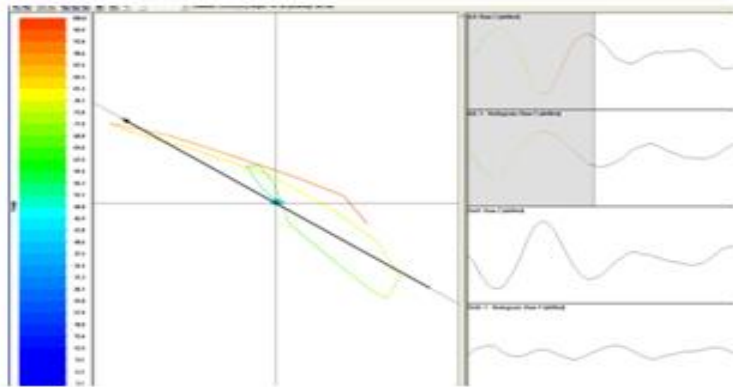


Figure B-13: Hodogram at 3116.85m depth.

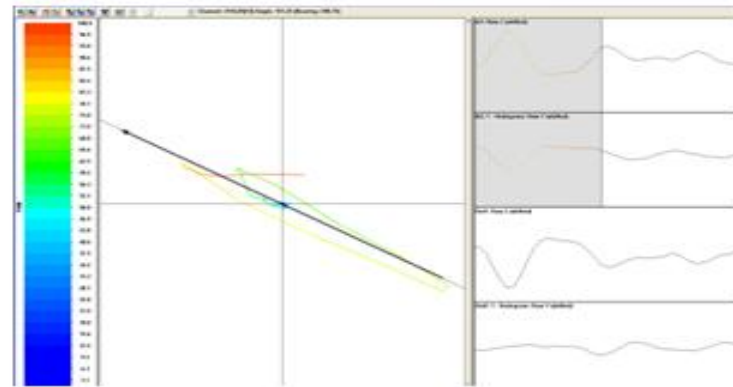


Figure B-14: Hodogram at 3124.63m depth.

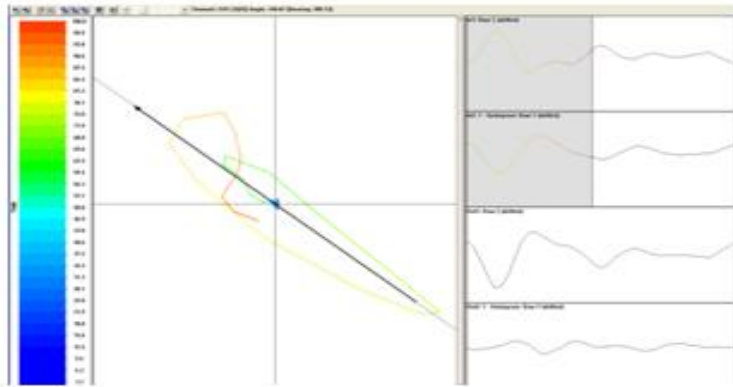


Figure B-15: Hodogram at 3141.33m depth.

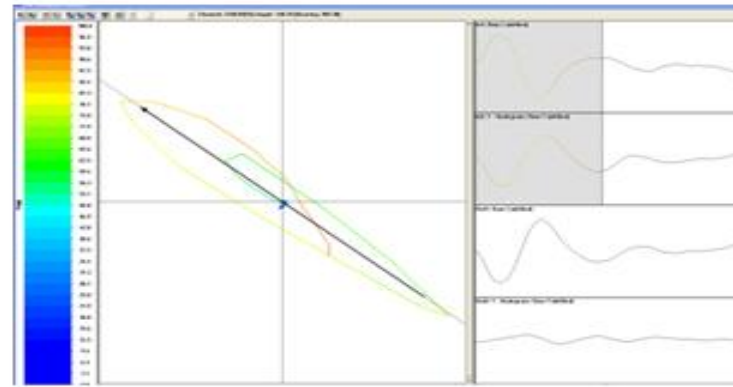


Figure B-16: Hodogram at 3148.64m depth.

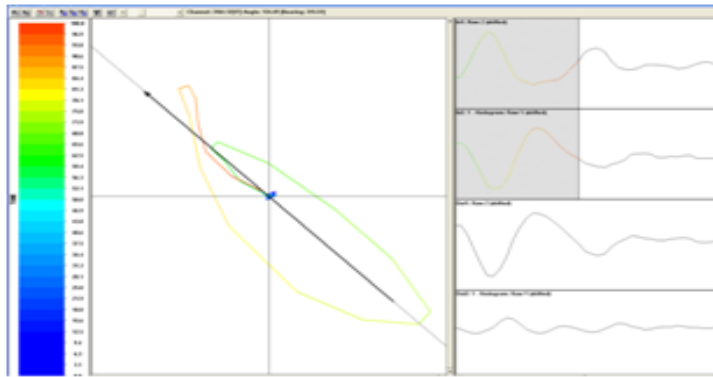


Figure B-17: Hodogram at 3164.12m depth.

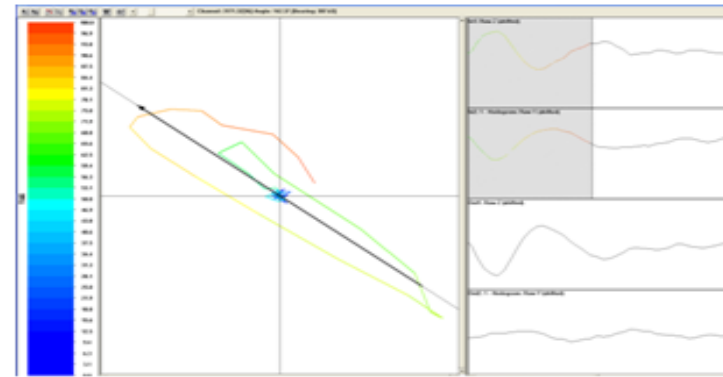


Figure B-18: Hodogram at 3171.03m depth.

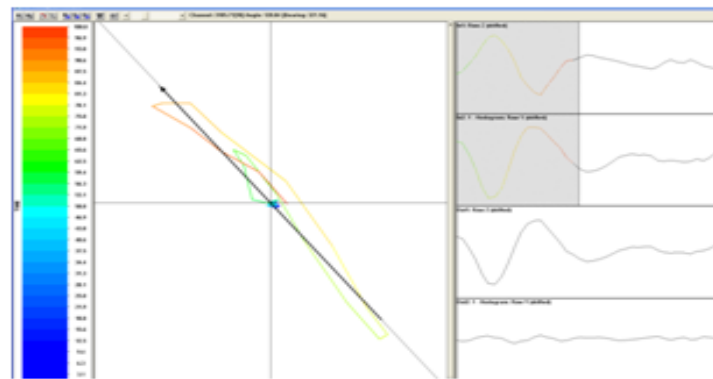


Figure B-19: Hodogram at 3185.71m depth.

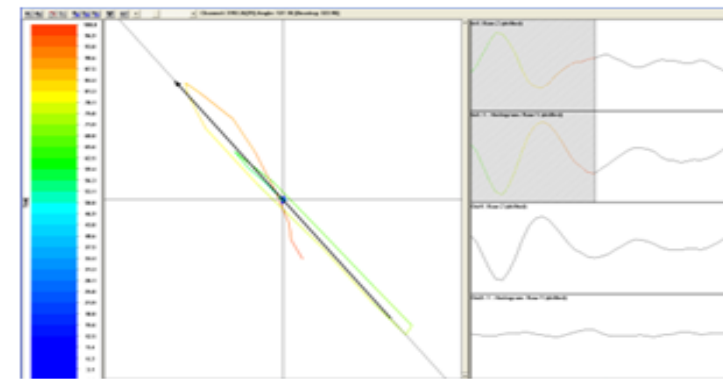


Figure B-20: Hodogram at 3192.26m depth.

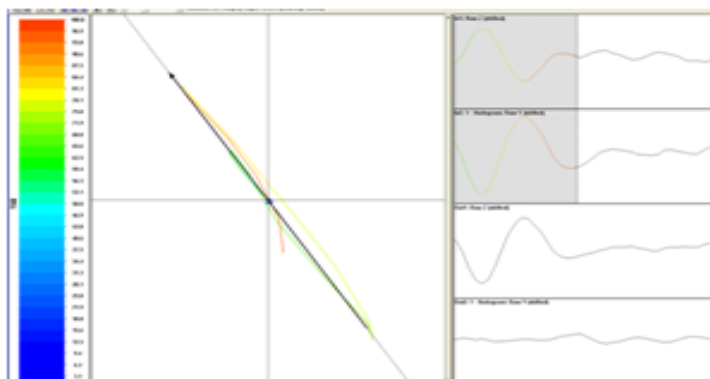


Figure A-21: Hodogram at 3211.68m depth.

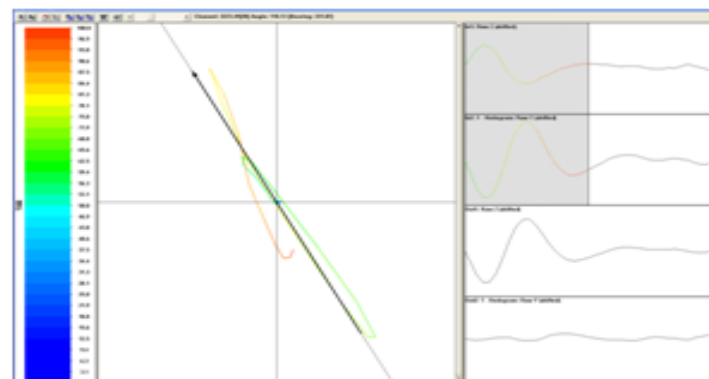


Figure A-22: Hodogram at 3223.49m depth.

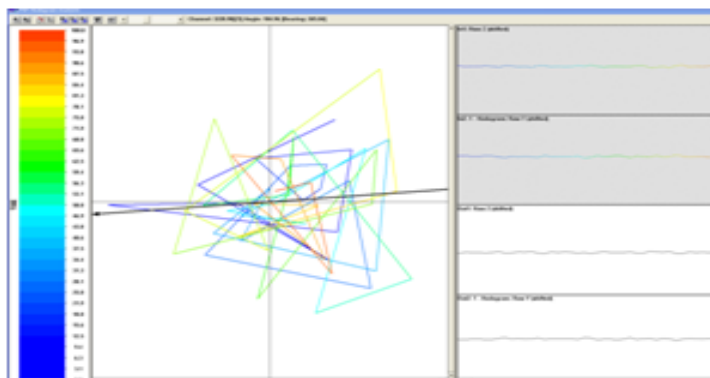


Figure A-23: Hodogram at 3228.90m depth.

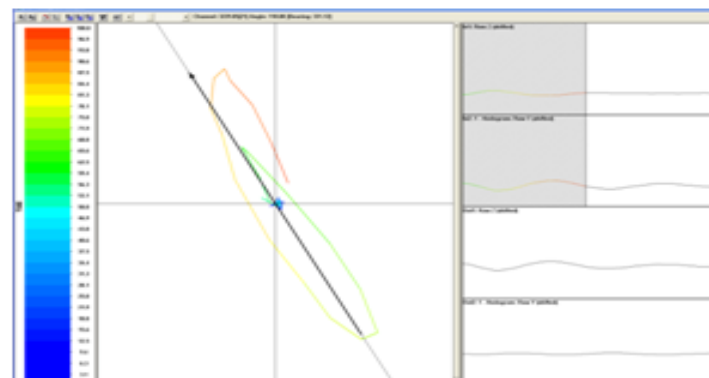


Figure A-24: Hodogram at 3229.03m depth.

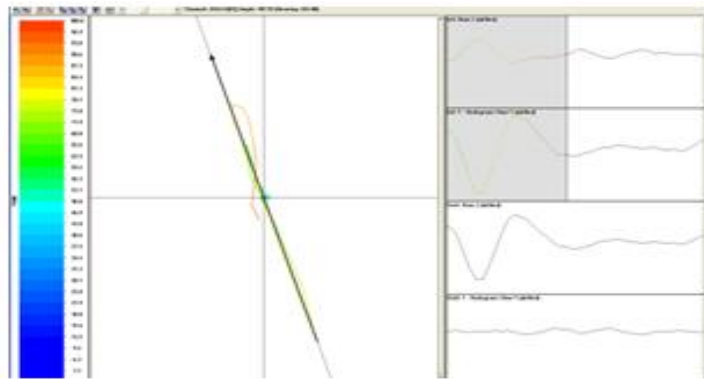


Figure B-25: Hodogram at 3239.08m depth.

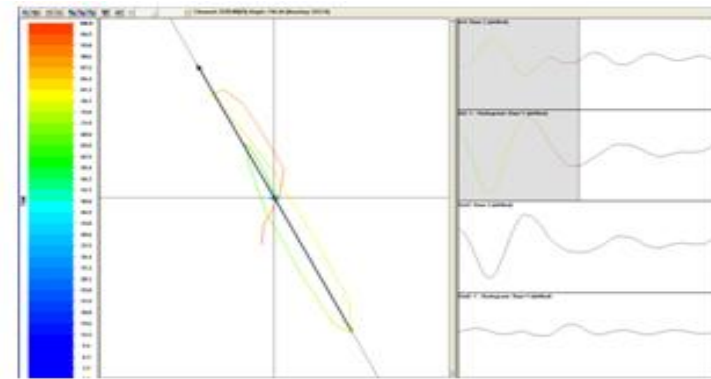


Figure B-26: Hodogram at 3243.53m depth.

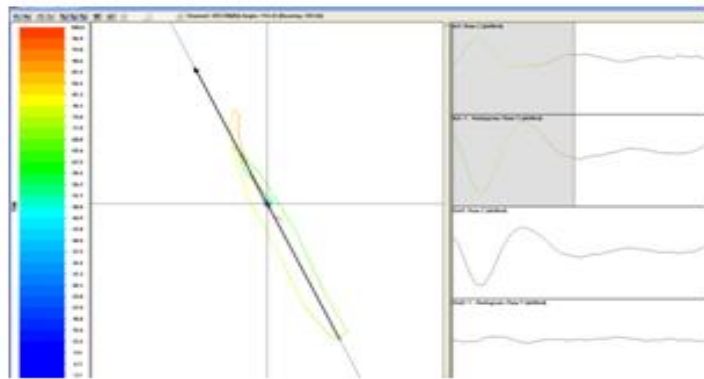


Figure B-27: Hodogram at 3252.64m depth.

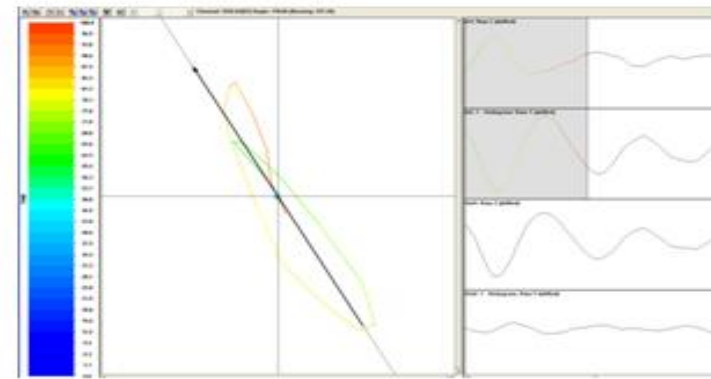


Figure B-28: Hodogram at 3257.00m depth.

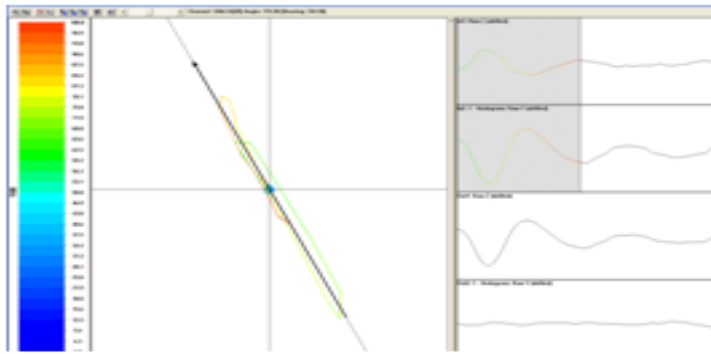


Figure B-29: Hodogram at 3266.54m depth.

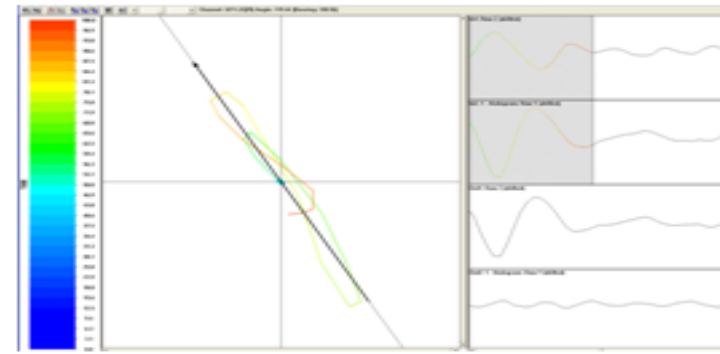


Figure B-30: Hodogram at 3271.22m depth.

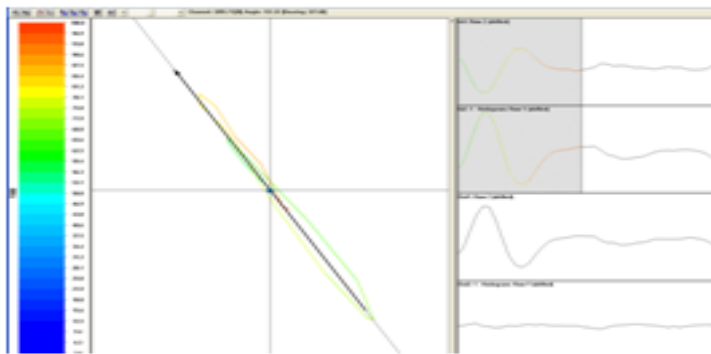


Figure B-31: Hodogram at 3285.71m depth.

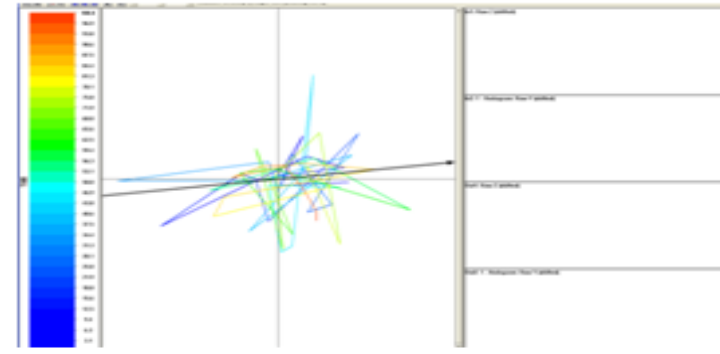


Figure B-32: Hodogram at 3296.05m depth.

